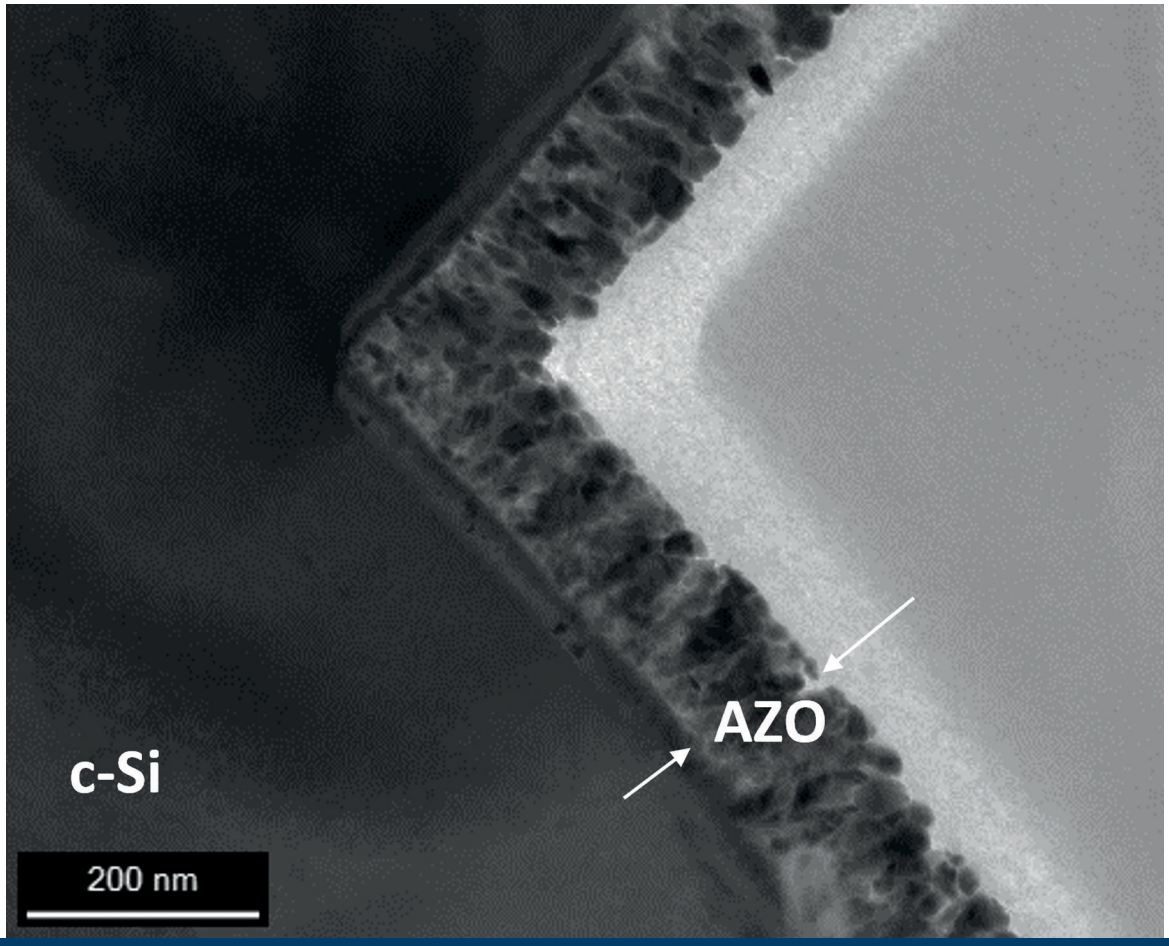

Microstructure and Functionality of Heterojunction contacts on crystalline Silicon solar cells

Sara Alkhereibi

Energie & Umwelt / Energy & Environment
Band / Volume 742
ISBN 978-3-69367-019-4

Mitglied der Helmholtz-Gemeinschaft

JÜLICH
Forschungszentrum

Schriften des Forschungszentrums Jülich
Reihe Energie & Umwelt / Energy & Environment Band / Volume 742

Forschungszentrum Jülich GmbH
Ernst Ruska-Centrum für Mikroskopie und
Spektroskopie mit Elektronen (ER-C)
Materialwissenschaft und Werkstofftechnik (ER-C-2)

Microstructure and Functionality of Heterojunction contacts on crystalline Silicon solar cells

Sara Alkhereibi

Schriften des Forschungszentrums Jülich
Reihe Energie & Umwelt / Energy & Environment Band / Volume 742

ISSN 1866-1793 ISBN 978-3-69367-019-4

Bibliografische Information der Deutschen Nationalbibliothek.
Die Deutsche Nationalbibliothek verzeichnet diese Publikation in der
Deutschen Nationalbibliografie; detaillierte Bibliografische Daten
sind im Internet über http://dnb.d-nb.de abrufbar.

Herausgeber und Vertrieb:	Forschungszentrum Jülich GmbH Zentralbibliothek, Verlag 52425 Jülich Tel.: +49 2461 61-5368 Fax: +49 2461 61-6103 zb-publikation@fz-juelich.de www.fz-juelich.de/zb
Umschlaggestaltung:	Grafische Medien, Forschungszentrum Jülich GmbH
Druck:	Grafische Medien, Forschungszentrum Jülich GmbH
Copyright:	Forschungszentrum Jülich 2026

Schriften des Forschungszentrums Jülich
Reihe Energie & Umwelt / Energy & Environment, Band / Volume 742

D 82 (Diss. RWTH Aachen University, 2026)

ISSN 1866-1793
ISBN 978-3-69367-018-7 (Print)
ISBN 978-3-69367-019-4 (E-Book)

Vollständig frei verfügbar über das Publikationsportal des Forschungszentrums Jülich (JuSER)
unter www.fz-juelich.de/zb/openaccess.



This is an Open Access publication distributed under the terms of the Creative Commons Attribution License 4.0,
which permits unrestricted use, distribution, and reproduction in any medium, provided the original work is properly cited.

Summary

This thesis explores how the microstructural characteristics of front-contact layers influence the efficiency and stability of silicon heterojunction (SHJ) solar cells. The study focuses on transparent conductive oxides (TCOs) such as aluminum doped zinc oxide (AZO) and indium tin oxide (ITO), as well as transparent passivating contacts (TPCs) based on hydrogenated nanocrystalline silicon carbide (nc-SiC:H) combined with a thin silicon oxide (SiO_2) layer. The present study emphasizes the crucial role of advanced transmission electron microscopy (TEM) techniques, which allow for direct nanoscale observation of solar cell structure for example: of the grain structure, crystallographic orientation, interface quality, and degradation pathways elements, that cannot be precisely evaluated with traditional characterization methods. In the first result chapter, AZO emerges as a promising TCO due to its affordability, abundance, and strong optoelectrical performance. However, its device behavior is governed by nanoscale structural features, particularly grain size, columnar growth, and grain boundary distribution. High resolution TEM (HRTEM) and precession assisted four dimensional scanning TEM (4D-STEM) with automated orientation analysis were used to map these microstructural signatures in AZO films deposited on hydrogenated amorphous silicon (a-Si:H) and hydrogenated nanocrystalline silicon (nc-Si:H). AZO on a-Si:H exhibited columnar grains exceeding 10 nm, whereas AZO on nc-Si:H showed grain sizes below 10 nm near the interface that expanded toward the film surface. In ITO/AZO bilayers, grain diameters ranged from 5 to 90 nm with significantly larger and irregular boundaries. These results demonstrate that larger columnar grains correlate with improved charge carrier mobility and that an ITO seed layer substantially enhances AZO crystallinity. The study also identifies sputtering induced damage as a critical performance factor, with RF sputtering producing far fewer interface defects than DC sputtering, thereby preserving better passivation quality. The second part investigates ultraviolet induced degradation (UVID) in TPC based SHJ cells. (J–V) measurements showed pronounced reductions in open-circuit voltage (V_{OC}), short-circuit current density (J_{SC}), and fill factor (FF) after 60 kWh m^{-2} UV exposure, with losses exceeding 10% in TPC devices.

TEM based structural analysis revealed no major elemental diffusion; instead, UV exposure triggered disorder, hydrogen depletion, and localized nanocrystallization within the nc-SiC:H layer. These changes degrade carrier transport and interface passivation, explaining the observed decline in performance. Overall, this thesis demonstrates that: (i) TCO microstructure is strongly substrate dependent and vital for optimizing SHJ front contact performance; (ii) AZO/ITO stacks offer superior crystallinity and enhanced electrical behavior; (iii) UV stability remains a major challenge for TPC based architectures; and (iv) TEM techniques play a pivotal role in uncovering the nanoscale mechanisms that govern material behavior and device reliability. The insights gained from these structural, electrical correlations provide a foundation for improving the efficiency and long term stability of the SHJ solar cells.

Zusammenfassung

Diese Dissertation untersucht, wie die mikrostrukturellen Eigenschaften der Frontkontaktschichten die Effizienz und Stabilität von Silizium-Heterojunction-(SHJ)-Solarzellen beeinflussen. Die Studie konzentriert sich auf transparente leitfähige Oxide (TCOs) wie aluminiumdotiertes Zinkoxid (AZO) und Indiumzinnoxid (ITO) sowie auf transparente passivierende Kontakte (TPCs) auf Basis von hydriertem nanokristallinem Siliziumkarbid (nc-SiC:H) in Kombination mit einer dünnen Siliziumoxidschicht (SiO_2). Die vorliegende Studie betont die entscheidende Rolle fortschrittlicher Transmissionselektronenmikroskopie-(TEM)-Techniken, die eine direkte Beobachtung der Solarzellenstruktur auf der Nanoskala ermöglichen, beispielsweise der Kornstruktur, der kristallographischen Orientierung, der Grenzflächenqualität und der Elemente der Degradationspfade, die mit traditionellen Charakterisierungsmethoden nicht präzise bewertet werden können.

Im ersten Ergebniskapitel erweist sich AZO aufgrund seiner Kostengünstigkeit, Verfügbarkeit und starken optoelektrischen Leistungsfähigkeit als vielversprechendes TCO. Sein Verhalten im Bauelement wird jedoch durch strukturelle Merkmale auf der Nanoskala bestimmt, insbesondere durch Korngröße, säulenförmiges Wachstum und die Verteilung der Korngrenzen. Hochauflösende TEM (HRTEM) und präzessionsunterstützte vierdimensionale Raster-TEM (4D-STEM) mit automatisierter Orientierungsanalyse wurden verwendet, um diese mikrostrukturellen Merkmale in AZO-Schichten zu kartieren, die auf hydriertem amorphem Silizium (a-Si:H) und hydriertem nanokristallinem Silizium (nc-Si:H) abgeschieden wurden. AZO auf a-Si:H zeigte säulenförmige Körner mit Größen von über 10 nm, während AZO auf nc-Si:H in der Nähe der Grenzfläche Korngrößen unter 10 nm aufwies, die sich zur Filmoberfläche hin vergrößerten. In ITO/AZO-Doppelschichten lagen die Korndurchmesser zwischen 5 und 90 nm, mit deutlich größeren und unregelmäßigen Korngrenzen. Diese Ergebnisse zeigen, dass größere säulenförmige Körner mit einer verbesserten Ladungsträgermobilität korrelieren und dass eine ITO-Keimschicht die Kristallinität von AZO erheblich verbessert. Die Studie identifiziert außerdem durch Sputtern verursachte Schäden als einen kritischen Leistungsfaktor, wobei

RF-Sputtern wesentlich weniger Grenzflächendefekte erzeugt als DC-Sputtern und dadurch eine bessere Passivierungsqualität aufrechterhält.

Der zweite Teil untersucht die durch ultraviolette Strahlung induzierte Degradation (UVID) in TPC-basierten SHJ-Zellen. (J–V)-Messungen zeigten nach einer UV-Exposition von 60 kWh m^{-2} deutliche Verringerungen der Leerlaufspannung (V_{OC}), der Kurzschlussstromdichte (J_{SC}) und des Füllfaktors (FF), wobei die Verluste bei TPC-Bauelementen mehr als 10% betrugen. Die TEM-basierte Strukturanalyse zeigte keine wesentliche Elementdiffusion; stattdessen führte die UV-Exposition zu Unordnung, Wasserstoffverarmung und lokalisierter Nanokristallisation innerhalb der nc-SiC:H-Schicht. Diese Veränderungen verschlechtern den Ladungsträgertransport und die Grenzflächenpassivierung und erklären damit den beobachteten Leistungsabfall. Insgesamt zeigt diese Dissertation, dass: (i) die TCO-Mikrostruktur stark vom Substrat abhängig und für die Optimierung der Leistung des SHJ-Frontkontakts von entscheidender Bedeutung ist; (ii) AZO/ITO-Schichtstapel eine überlegene Kristallinität und ein verbessertes elektrisches Verhalten bieten; (iii) die UV-Stabilität weiterhin eine große Herausforderung für TPC-basierte Architekturen darstellt; und (iv) TEM-Techniken eine zentrale Rolle bei der Aufdeckung der nanoskaligen Mechanismen spielen, die das Materialverhalten und die Zuverlässigkeit der Bauelemente bestimmen. Die aus diesen strukturell-elektrischen Korrelationen gewonnenen Erkenntnisse bilden eine Grundlage für die Verbesserung der Effizienz und Langzeitstabilität von SHJ-Solarzellen.

Table of Contents

1 Introduction **11**

1.1 Preface 11

1.2 Aim and outline of this thesis 14

2 Theoretical background **17**

2.1 Photovoltaic solar cells 17

2.1.1 Photovoltaic basics 17

2.1.2 Limit of the solar cell efficiency 19

2.1.3 Recombination losses 21

2.1.4 Solar cell parameters 22

2.2 Silicon heterojunction solar cell 24

2.2.1 Light trapping 26

2.2.2 Carrier transport and selectivity 26

2.3 Materials and properties 28

2.3.1 Transparent conductive oxide 28

2.3.2 Electrical conductivity 29

2.3.3 Transport mechanisms 30

2.3.4 Aluminium-doped zinc oxide 31

2.3.5 Indium-doped tin oxide 32

2.3.6 Silicon carbide 34

2.4 Microscopy techniques 35

3 Methods and sample preparation **37**

3.1 Transmission electron microscopy 37

3.1.1 Background 37

3.1.2 Principles of electron imaging 38

3.1.3 TEM setup and components 42

3.1.4 Electron interaction with sample materials 44

3.1.5 TEM modes and contrast 46
3.2 Scanning transmission electron microscopy (STEM) 48
3.3 Electron diffraction 50
3.4 Analytical electron microscopy technique 55
3.4.1 Energy dispersive x-ray (EDX) 56
3.4.2 Electron energy loss spectroscopy (EELS) 57
3.5 TEM sample preparation 57
3.5.1 Conventional method 58
3.5.2 Focused ion beam (FIB) 60
3.6 Fabrication of solar cells 64
3.6.1 Silicon heterojunction solar cell 64
3.6.2 Transparent conductive oxide 66
3.6.3 Transparent passivating contact 67
3.7 Experimental details 68
3.8 Conclusion 70

4 Challenges in TEM sample preparation of solar cell and solutions 73
4.1 Limitations and practical difficulties in TEM sample preparation 73
4.2 Conclusion 81

5 Microtructural evaluation of AZO-front contact on SHJ solar cell 83
5.1 Introduction 83
5.2 Electrical Performance of SHJ solar cells with AZO and AZO/ITO layers . 87
5.3 TEM investigation of TCO thin film 91
5.4 Microstructural and elemental characterization 95
5.5 Orientation mapping and influence of grain size and boundaries 98
5.6 Impact of magnetron sputtering on the structural properties 106
5.6.1 Electrical Performance 108
5.7 Conclusion 110

6 Ultraviolet-induced degradation in TPCs solar cells 113
6.1 Brief review of UVID degradation in TPCs solar cells 113
6.2 Samples for the study 117
6.3 TPCs solar cell performance 119
6.3.1 J-V characteristics 119

6.4 Insight into ITO/nc-SiC:H front contact microstructure 121
6.4.1 Mapping grains in the ITO/nc-SiC:H front contact 124
6.5 Conclusion 129

7 Conclusions and future work **131**
7.1 Conclusions 131
7.2 Future work 133

List of Abbreviations **135**

Appendix **139**

List of Figures **147**

List of Tables **149**

References **159**

1 Introduction

1.1 Preface

One of the fundamental challenges humanity faces today is energy generation. Global energy systems are confronted with numerous strategic issues. For instance, the increasing disruptions in energy supply due to population growth present worldwide challenges at all levels [1]. The potential environmental damage caused by the production and consumption of energy, as well as the disposal of waste from traditional energy sources, is a burden on all of humanity and remains a critical area of research. Additionally, the persistent issue of energy poverty is a fundamental challenge in this domain. Further resource depletion, exacerbated by population growth in the poorest countries already dependent on traditional energy, poses another threat to the world and the business community. Therefore, there is an urgent need for humanity to address the issue of energy poverty. The global population is growing, and so is the energy demand. As the world's electricity generation continues to rely heavily on fossil fuels, increased electricity production leads to higher carbon dioxide (CO_2) emissions, which have detrimental effects [2, 3]. Increasing the production of energy or electricity through renewable energy generation is one of the most important modern methods to be worked on to achieve the goals of the Paris Climate Agreement of 2016 [4], which can be attributed to the decarbonization of all industrial sectors to reduce climate change. Whereas coal alone accounted for about 38% of global electricity generation in 2018. Such dependence adds to increasing CO_2 emissions. Incredibly, these renewable energies are coming up, with an increase in global electricity participation from 8.4% in 2017 to 9.3% in 2018; however, fossil fuels still dominate. Coal, natural gas, and renewables shared the burden of the 3.7% increase in electricity consumption in 2018, thus increasing carbon emissions by another 2.7%, which is the highest increase in seven years. By 2020, renewables had grown to supply about 28% of global electricity, up from lower percentages just a few years earlier [5]. Despite this growth, fossil fuels still dominate. In 2024, total energy-related CO_2 emissions reached a record $\sim$37.8 gigatonnes, increasing $\sim$0.8% over

the prior year. Renewables are expanding rapidly and are projected to make up around 30-35% of the global electricity mix by 2025, but they still must scale further and faster to offset the emissions from fossil fuels [6].

To stay on track with the Paris Agreement targets, energy-related emissions must decline by 3.5% annually through 2050. With the status quo of the energy mix remaining for more than two decades, it is now more timely than ever that the expansion of renewable energy occurs at a significantly faster rate to counterbalance the ever-increasing energy demand [7].

Renewable energy is derived from natural sources. There are five main sources of renewable energy: wind, biomass, geothermal, hydroelectric, and solar (thermal and photovoltaic) [2, 8]. All of these forms of energy are, in principle, capable of producing large amounts of electricity for current and future use. These sources are inexhaustible because they are available in almost permanent abundance, unlike traditional energy sources based on fossil fuels such as coal, oil, and gas. They have another advantage that makes them a humanitarian necessity and goal: they are environmentally friendly, as they do not contribute to the production of carbon dioxide or other greenhouse gases. They also allow us to distribute energy more equitably, as they can supply poorer regions, helping to reduce their dependence on energy from other countries.

Photovoltaic (PV) electricity production is one of the most important driving forces behind the increase in renewable energy production and utilisation, which showed a growth rate of 28.9% in 2018 [2]. The economic cost competitiveness with the cost of conventional electricity production in many countries is one of the most important reasons for the increase in PV electricity production [8]. The aim is to reduce solar module costs and increase the efficiency of the solar cells [3, 9].

The accelerating global shift toward renewable energy has brought solar PV technology to the forefront of sustainable energy solutions. From the various PV technologies, Crystalline Silicon (c-Si) has been a dominant material platform for a long time due to its abundance, reliability, and maturity, sharing about 97% of the global production of solar cells and modules [9]. According to global world-scale manufacturers, silicon heterojunction (SHJ) solar cells technology is the second most available n-type concept nowadays, and it is expected to increase the 2023 market share of about 5% to over around 19% within the next ten years. Due to the high-power conversion efficiency (η), lean fabrication process, and low-temperature coefficient. High efficiency is the biggest advantage of SHJ

solar cells, which increases their competitiveness for mass production [10] and achieving power converting efficiency up to 26.81% [11].

SHJ solar cells have emerged as one of the most efficient silicon-based architectures, combining a high-quality crystalline silicon wafer with thin layers of Hydrogenated Amorphous Silicon (a-Si:H) to achieve excellent surface passivation and carrier selectivity. A key factor that governs the performance of SHJ solar cells is the design and optimization of the front contact structure, which must satisfy multiple functional requirements: high optical transparency, low electrical resistance, and minimal carrier recombination at the interface [12]. However, the front contact remains a performance-limiting factor, especially in terms of parasitic absorption, interface losses, and series resistance. Conventional front contacts often employ Transparent Conductive Oxides (TCO) such as Aluminum-doped Zinc Oxide (AZO) or Indium Tin Oxide (ITO) [13]. More recently, Transparent Passivating Contacts (TPC) such as ITO combined with NanoCrystalline Silicon Carbide (nc-SiC:H) have attracted attention for their ability to further suppress recombination and enhance carrier selectivity at the front interface [14].

Although these materials have shown great potential and common features that can improve the efficiencies of solar cells on the nanoscale, this creates a need for the correlation between their nanostructural properties and device-level performance. The nanostructure of the materials, like interfaces of the thin film, grain size and crystallographic orientation, can significantly affect carrier transport, charge carrier mobility, and overall solar cell efficiency. This is true in the TCO and TPC thin film layers, which are typically polycrystalline, consisting of many small grains with varying orientations and boundaries that influence electrical behavior. Therefore, a thorough understanding of the nanostructure and correlating it with the optoelectrical properties of these materials is essential for optimizing SHJ solar cells. Figure 1.1 illustrates the correlation between nanostructural, optoelectrical properties and device performance of solar cell devices. To generate understanding of the device physics of solar cells, we have to go from material parameters governed by the nanostructure of the materials to the macroscopic properties governed by the optical/electrical properties with a characterizing method to reach the target efficiency and performance.

This thesis utilises advanced Transmission Electron Microscopy (TEM) techniques, notably 4D Scanning Transmission Electron Microscopy (4D-STEM), to thoroughly investigate the effects on the structure of the front-contact layers. 4D-STEM provides orientation and phase mapping with remarkable nanometer resolution of 2 nm, making it an excellent

tool for analyzing polycrystalline materials such as AZO and ITO. By visualizing grain and orientation mappings, we can establish a correlation between microstructure and the key performance parameters of the solar cell device.

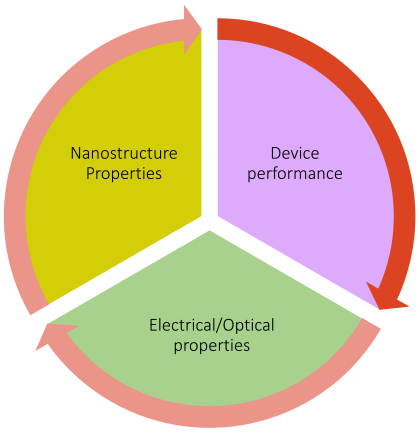

Figure 1.1: *Schematic representation illustrating the correlation between nanostructural properties, electrical/optical characteristics, and overall device performance in a solar cell.*

1.2 Aim and outline of this thesis

The primary objective of this thesis is to examine the influence of nanostructural characteristics of front contact layers in SHJ solar cells on their electrical and device performance. Therefore, the first part investigates the nanostructure, including grain size, orientation, and phase distribution, of the TCO thin films in the front contact of the SHJ solar cells. A detailed investigation of nanostructural features, such as grain and phase orientation of the AZO thin film deposited on a different hydrogenated silicon substrate and ultrathin ITO seed layer was performed using 4D-STEM to facilitate nanoscale orientation and phase mapping. It also correlates the nanostructural properties of the front contact thin films with the electrical properties and performance device of the solar cell. In the second part, the orientation and phase map of the front contact passivation layer were investigated after ultraviolet-induced (UV) treatment. This thesis is structured as follows:

Chapter 2 provides background and essential information on solar cell devices and materials selection. In Section 2.1, general principles of photovoltaic technology are in-

troduced, with an emphasis on c-Si-based solar cell technologies. Section 2.2 presents the fundamental theory behind SHJ solar cells. In Section 2.3 the physical properties of the electrical conductivity and transport mechanism in the semiconductor materials used for the front contact of SHJ solar cells, including AZO, ITO, and nc-SiC:H, are discussed. Section 2.4 emphasises the role of advanced microscopy techniques at the nanoscale level, especially in analyzing the nanostructure of solar cell materials.

Chapter 3 presents the main methods and sample preparation techniques. Section 3.1 present the TEM technique as the main method in this thesis, the historical background of TEM, the physical principle of electron imaging, and the layout of the TEM, as well as the type of imaging in the TEM are presented. Section 3.2 covers the basics of electron diffraction; Section 3.3 present the 4D-STEM method and its example of application, the orientation and grain mapping inside it. Section 3.4 describes analytical electron microscopy, the Energy Dispersive X-ray (EDX) as an example; Section 3.5 presents TEM sample preparation; Section 3.6 details the fabrication of solar cells; Section 3.7 examines solar cell device characterization; and finally, Section 3.8 presents structural characterization techniques.

Chapter 4 describes the technical challenges faced while preparing TEM samples from entire solar cell devices.

Chapter 5 presents the optimization of the front-contact SHJ solar cell, identifying the influences of different substrates on the growth of the AZO thin films, includes hydrogenated amorphous or nanocrystalline silicon layers (n/i)a-Si:H, (n)nc-Si:H/(i)a-Si:H, and with seedlayer ITO/(n/i)a-Si:H, as well as exploring their impact on the performance of the SHJ solar cell device. High resolution scanning TEM (HRSTEM) images for the interfaces are included, along with orientation mapping and the influence of grain size and boundaries on the three structures, which were analysed using 4D-STEM.

Chapter 6 examines the TPC passivation mechanism in the front contact of SHJ solar cells and evaluates the impact of UltraViolet-Induced Degradation (UVID) on the SHJ solar cell. General microscopy charcterization is included additionally, implementation of the orientation and grain mapping techniques to differentiate between the two structures with UV-induced and reference without UV-induced degrdation.

Finally in **Chapter 7** the main results are summarized and further work on the topic of the microscopy study of the materials of the SHJ solar cell will be discussed. This research aims to provide valuable insights into the optimization of front contact materials

in SHJ solar cells. The findings of this study will contribute to the ongoing development of high-efficiency photovoltaic technologies.

2 Theoretical background

This chapter provides background and fundamental information on photovoltaics and materials choices for the solar cells, as well as the need for microscopy characterization techniques for these materials. In section 2.1, general photovoltaic basics are introduced, and the different technologies related to the case of c-Si-based solar cells are described. Section 2.2 presents the theoretical framework behind SHJ solar cells. While section 2.3 focuses on material choices for the front contact of SHJ solar cells, discussing their electrical and structural properties. Finally, section 2.4 emphasises the role of advanced microscopy techniques at the nanoscale level, especially in analyzing the nanostructure of solar cell materials.

2.1 Photovoltaic solar cells

This work focuses on silicon photovoltaic (PV) solar cells. It will first explain how a solar cell operates and highlight its key characteristics. Then, it will examine the factors that limit their efficiency and review the main existing silicon solar cell technologies.

2.1.1 Photovoltaic basics

In recent years, generating electricity through photovoltaics has become a vital response to global energy challenges. As a sustainable, affordable and clean energy source, solar energy has increasingly gained popularity among all renewable resources. Of the various renewable energy options, PV technology harnessing solar energy has seen more extensive development than others [3, 15].

In principle, the PV effect is a fundamental process in semiconductors, where incoming photons from sunlight having energy $E = h\ \nu$, where h is Planck's constant and ν is the frequency of light. When energy is equal to or greater than the bandgap energy (E_g)

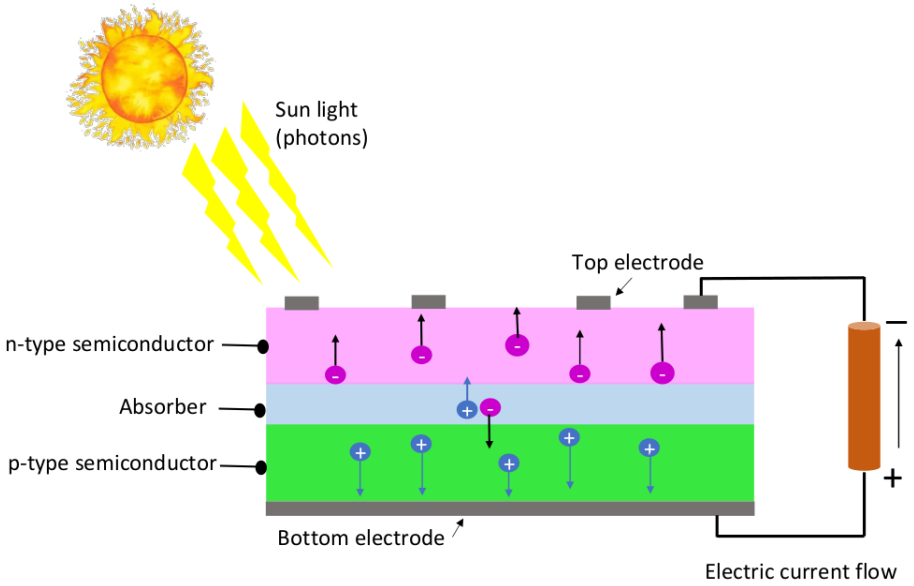

Figure 2.1: *Functional diagram of a photovoltaic solar cell with an external circuit component.*

of the semiconductor material, electrons are excited from the valence band (E_v) to the conduction band (E_c). Where the E_g of a semiconductor is a property that defines the minimum photon energy required for an electron excitation from the valence band E_v to the conduction band E_c. It represents the energy difference between the highest point of the E_v and the lowest point of the E_c, which dictates the electrical and optical properties of the material.

The photon energy must be higher than the E_g present in the semiconductor so that electron–hole pair generation is possible due to the absorption of photon energy. If the energy of the photons is less than the E_g then no energy absorption is possible, no electron–hole pair will be generated, and the material will seem to be transparent for the respective photons. However, the photon energy should not be much greater because there will be more heat loss along with electron–hole pair generation. The semiconductor to be selected must absorb the maximum percentage of the solar spectrum efficiently. In crystalline silicon solar cells,for example, the bandgap of 1.1 eV for silicon corresponds to wavelengths (λ) of 1130 nm and lower [16], as the photon energy depends on the wavelength by de Broglie's law and charge carrier mobility determines the overall performance of the

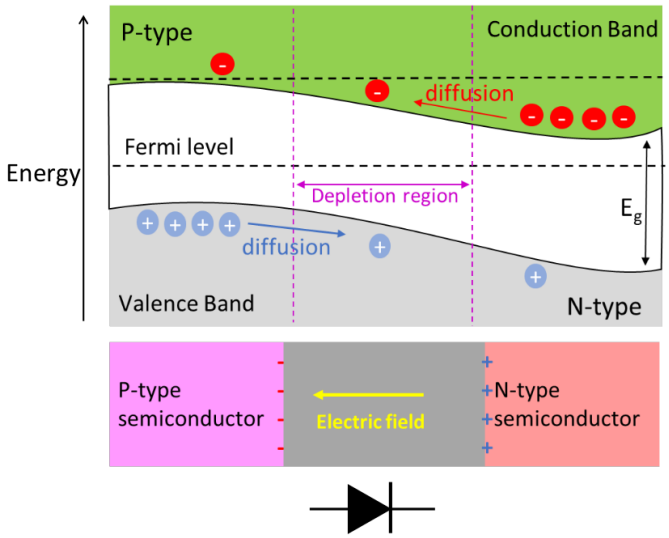

Figure 2.2: *The energy band diagram of the p-n junction.*

light absorption on PV [17]. The physical structure of a PV cell is shown in **Figure 2.1**. Basically, PV cells are made up of two different types of semiconductors: n-type and p-type, which come together to create a p-n junction. **Figure 2.2** illustrate the principle work of the p-n junction and the band diagram. When these materials are linked, electrons from the n-type region move into the p-type region, while holes from the p-type region move into the n-type region. As they recombine, they leave behind fixed, charged ions: positively charged donor ions in the n-type region and negatively charged acceptor ions in the p-type region. This movement creates a depletion region at the junction, establishing an internal electric field due to the separation of charges. This process creates an internal electric field across the depletion region. When light is absorbed in the solar cell, it generates additional electron-hole pairs. These photogenerated carriers are then separated by the internal electric field, contributing to the generation of electric current [10, 18, 19].

2.1.2 Limit of the solar cell efficiency

A single cell can utilize only a particular fraction of the solar spectrum. Multiple cells with many p-n junctions, known as multijunction (MJ) cells, are capable of enhancing this limitation and extracting maximum energy from solar irradiation. These solar cells are also

known as tandem cells since multiple p-n junctions are connected in tandem, each tuned to a particular frequency of the spectrum. MJ solar cells are also prevalent at present as they can significantly improve the efficiency of PV cells [18]. The overall efficiency of this process depends on several critical factors, including the purity and structural quality of the semiconductor, effective surface passivation to reduce recombination losses, and advanced light-trapping techniques that enhance photon absorption [10, 20, 21].

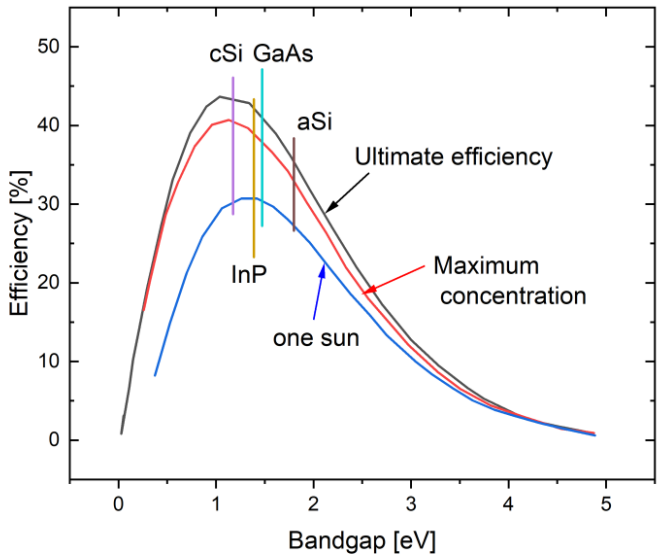

Figure 2.3: *Theoretical efficiency limits of single-junction solar cells as a function of the semiconductor bandgap. Adapted from [22].*

A widely used approach for measuring losses in photovoltaic energy conversion for single-junction solar cells is the Shockley-Queisser (SQ) model, which relies on the principle of detailed balance [23]. This principle asserts that in thermodynamic equilibrium, every process must be counterbalanced by its reverse process. In the context of solar cells, this means that the absorption of photons must be offset by the radiative recombination of electrons and holes, as discussed later. Shockley and Queisser proposed that photons with energies below the band gap pass through the cell without absorption, while photons with energies above the band gap are fully absorbed. They also assumed that electrons and holes are in thermal equilibrium with the lattice and disregarded all other loss mechanisms. Based on these assumptions, **Figure 2.3** shows the ideal efficiencies as functions of the

bandgap E_g under one-sun illumination, under maximum concentration of sunlight, and what is called the ultimate efficiency at 6000 K.

In simplicity, materials with a too low bandgap waste energy as heat (thermalization), while those with a too high bandgap miss many usable photons [24]. The efficiency varies slightly depending on whether incident and emitted photon spectra are described using black-body radiation, the AM 1.5 G spectrum for the sun, or a generalized Planck equation with a chemical potential for the cell. According to this assessment, the maximum efficiency achievable for a single junction solar cell under standard testing conditions using the one sun spectrum is approximately 33% [22]. These record efficiencies are very close to the theoretical limit of Si efficiency, known as the Shockley-Queisser limit and equal to 29% in Si single-junction for a bandgap near 1.1 eV under one sun illumination at the room temperature.

To achieve a high PV conversion efficiency close to the SQ limit, the following criteria are required [25]: (1) All incoming photons with energy above the bandgap must be absorbed. (2) Each absorbed photon must create one electron–hole pair. (3) All photo-generated charges must reach the contacts. (4) The contacts must be completely selective, blocking the opposite charge. (5) Charges must reach the external circuit with minimal voltage (recombination), fill factor (resistance), and current (parasitic absorption, reflection) loss.

2.1.3 Recombination losses

Generation and recombination describe the processes where free electron-hole pairs are created and annihilated. Specifically, an electron in the valence band is either excited to the conduction band or releases energy to fall back to the valence band. Recombination mechanisms can be classified as radiative and nonradiative decay, as well as the intrinsic and extrinsic mechanisms [26]. Indeed, these processes can occur via various pathways, including phonon absorption and emission of photons. Three primary recombination mechanisms are observed in solar cells:

- **Radiative recombination**
- **Auger recombination**
- **Shockley-Read-Hall (SRH)**

Radiative recombination results in the emission of excess energy as photons with

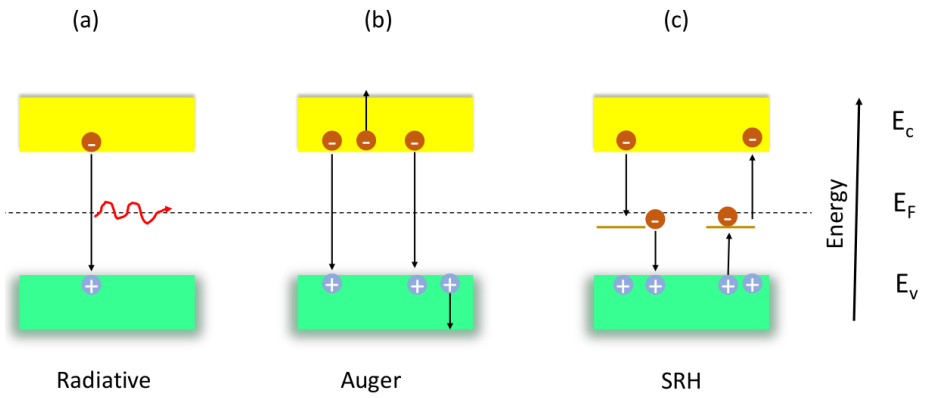

Figure 2.4: *Recombination mechanisms in semiconductors. The black arrows indicate the direction of the electron (brown circuit with minus sign) transitions. The holes (blue circle with plus sign) travel against the arrow direction. (a) depicts the schematic of spontaneous radiative recombination, (b) depicts the Auger recombination processes, (c) shows the four basic transitions that may occur during SRH recombination.*

energy approximately equal to the bandgap ($E_p h \sim E_g$) as shown in **Figure 2.4(a)**. In contrast, the Auger recombination process involves electrons recombining with holes, with the excess energy transferred to a second electron in either the conduction or valence band, rather than being emitted as light as in **Figure 2.4(b)**. In the Shockley-Read-Hall (SHR) recombination process, illustrated in **Figure 2.4 (c)**, it does not happen as a direct decay process from one band to another; instead, electron-hole pairs recombine via deep-level impurities or defects located within the forbidden band gap.

2.1.4 Solar cell parameters

Key parameters that characterize the performance of c-Si based solar cells are:

- Short-circuit current density (J_{SC}), is depends on optical losses that hinder the light from being fully absorbed in the c-Si absorber and on the collection efficiency of the photogenerated charge carriers.
- Open-circuit voltage (V_{OC}) is fundamentally determined by the band gap and quasi-fermi level splitting.
- Fill factor (FF), the ratio between the surface area covered by the filled rectangle and the outer dashed rectangle of the $J-V$ curve also represents the fill factor, and

the maximum power point (MPP) at this point, the voltage and current are at their optimal values, and the solar cell produces its maximum power output. The MPP is located near the bend on the $J-V$ curve. If the voltage across the solar cell is increased beyond the MPP, the current decreases rapidly, and the $J-V$ curve drops sharply. This region is known as the saturation region or negative-resistance region of the curve, as shown in **Figure 2.5**. The ratio between the maximum $P_{\max}= J_{\max}V_{\max}$ and the full square spanned by the V_{OC} and J_{SC} values represents the fill factor:

$$FF = \frac{J_{\max}V_{\max}}{J_{SC}V_{OC}}$$

The value of FF ranges from 50% to 82%. For a silicon solar cell, FF is typically approximately 80%. The value increases with higher shunt resistance and lower series resistance. A higher FF value is desirable because it is a direct indicator of the quality of the solar cell.

- Power conversion efficiency (η) is the percentage of solar energy incident on the solar cell that is converted and extracted into charge carriers. In other words, it is the ratio of the maximum power density that can be extracted ($P_{\max}$) to the power density of incident sunlight (P_{sun}) at which the solar cell is illuminated (100 mW/cm^2); the formula for the η is: $\eta = P_{\max}/P_{sun}$

  Based on the maximum power output of the solar cell, P_{max}, J_{SC}, V_{OC}, and FF. The efficiency can then be described as:

$$\eta = \frac{J_{SC}V_{OC}FF}{P_{sun}}$$

A typical $J-V$ curve of a solar cell is shown in **Figure 2.5**. The short-circuit current density J_{sc} is the maximum current density and is obtained in short-circuit conditions at $V = 0$. In the ideal case, it should equal the photo-generated current density J_{ph}, assuming that the dark current at short-circuit conditions can be neglected. The open-circuit voltage V_{oc} is the maximum voltage generated by the solar cell and is obtained at $J = 0$, when no net current is drawn.

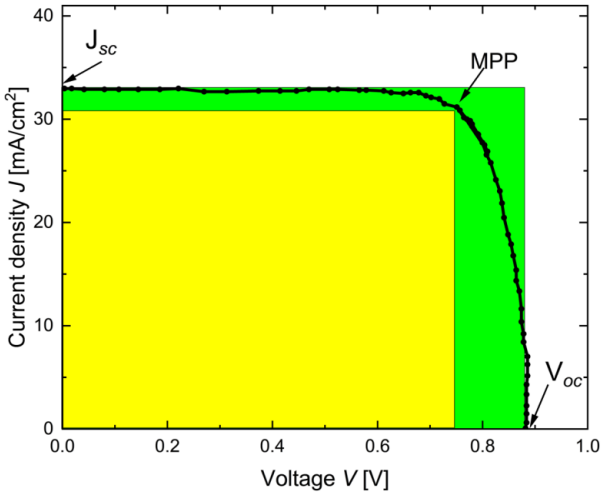

Figure 2.5: *Current density-voltage ($J-V$) curve of a solar cell and the parameters that can be evaluated: short-circuit current density J_{sc}, open-circuit voltage V_{oc}, current density and voltage at the maximum power point (MPP).*

2.2 Silicon heterojunction solar cell

The concept of a diode using a heterojunction formed on the contact between doped amorphous silicon layers and c-Si wafer was first proposed in 1974 [27]. In 1983, the silicon heterojunction (a-Si:H/poly-Si) was integrated for the first time in a tandem junction solar cell, the so-called Honeymoon cell by Hamakawa et al. [28].

In principle, positively doped (p) or negatively doped (n) crystalline silicon c-Si is used as an absorber in the SHJ device. An ultrathin intrinsic hydrogenated amorphous silicon (i-a-Si:H) layer is used to passivate both sides of the c-Si. Which are appealing candidates for buffer layers: their bandgap is slightly wider than that of c-Si, where c-Si has an indirect bandgap $\sim$1.12 eV due to its perfect periodic crystal structure, whereas a-Si:H has a wider bandgap $\sim$ 1.7–1.8 eV because of structural disorder and localized electronic states. It can also be doped relatively easily, either n or p type, enabling the fabrication of electronic heterojunctions. The function of these layers is to create the p-n junction and to further reduce recombination for charge carrier selectivity. In order to improve the transport of photogenerated charge carriers in the lateral direction, highly doped TCO layers are needed. If deposited with the right thickness, the TCO layer can

also work as an antireflection coating. It therefore requires sufficient electrical properties, effective contact properties with both the a-Si:H layer and the metallization, and suitable optical properties. Lastly, the charge carriers are collected and transported to the metal grid. Details on the working principle of the heterojunction solar cells can be found in Refs [10, 29].

The stack a-Si:H(i)/a-Si:H(n)/TCO and a-Si:H(i)/a-Si:H(p)/TCO are called front and back contact, forming the electron and hole contacts, respectively. SHJ solar cells using TCO materials have achieved a record power conversion efficiency of up to 26.81% [11]. Heterojunction cells combine a c-Si wafer with thin layers of a-Si:H, this hybrid configuration leverages the low defect density and excellent carrier transport properties of crystalline silicon alongside the effective surface passivation and bandgap tuning capabilities of amorphous silicon. The bandgap of a-Si:H can be tuned during deposition by controlling its hydrogen content, which passivates dangling bonds, and by alloying with elements such as carbon or oxygen (forming a-SiC:H or a-SiO:H), allowing the optical bandgap to be widened up to $\sim 2\ eV$ [30]. The basic layout of the most common SHJ solar cell concept is presented in **Figure 2.6**.

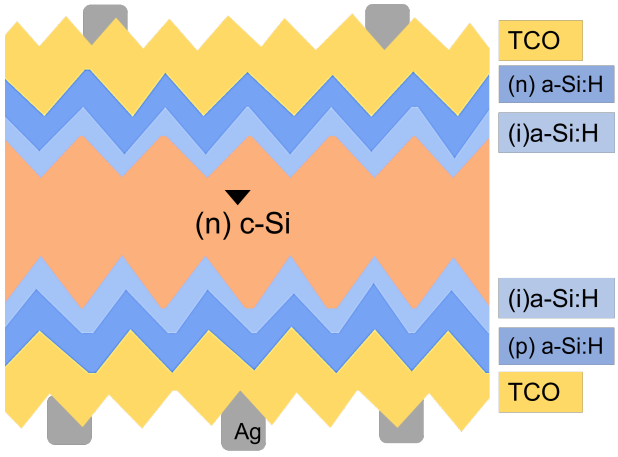

Figure 2.6: *Structure of silicon heterojunction solar cells built on pyramidal-textured n-type c-Si wafers and an intrinsic thin layer.*

2.2.1 Light trapping

Texturing plays a crucial role in SHJ solar cells by enhancing light trapping and increasing photon absorption within the silicon absorber layer. Due to silicon's indirect bandgap, a flat surface allows a significant portion of incident sunlight to pass through without being absorbed. By introducing surface texture, reflection is reduced, and the optical path length within the silicon is extended, thereby improving photon absorption.

The texturing process is influenced by the crystal orientation of c-Si. When using an alkaline potassium hydroxide (KOH) solution, anisotropic etching occurs due to the varying etch rates in different crystallographic directions. For <100> oriented silicon wafers, anisotropic etching in the presence of suitable additives leads to the formation of a pyramidal structure, which is widely used in SHJ solar cells. **Figure 2.7 (a)** represents the anisotropic KOH etching process on a c-Si wafer. The illustration shows how etching preferentially removes material along the (100) crystal orientation, while leaving behind (111) facets, which form characteristic pyramidal structures widely used for surface texturing in SHJ solar cells. Scanning electron microscope (SEM) images of textured c-Si surfaces after KOH-based anisotropic etching. The left with a scale of 20 μm, while the right image is at a smaller scale of 10 μm are shown in **Figure 2.7 (b)**. Beyond optical enhancement, texturing also impacts the electronic properties of SHJ cells. An a-Si:H film deposited on a (111) surface shows reduced epitaxial growth compared to a (100) surface. This minimizes interface defects, increases the minority carrier lifetime, and results in higher V_{oc} [31, 32].

2.2.2 Carrier transport and selectivity

The foundational operation of an SHJ solar cell relies on selective carrier transport, wherein layers with highly asymmetrical conductivity enable one type of charge carrier, electrons or holes, to flow freely while blocking the other [33]. This asymmetry may result from the intrinsic material properties or extrinsic doping techniques. For instance, electron-selective transport layers are designed to exhibit high electron conductivity but low hole conductivity, effectively allowing electrons to be collected while impeding holes. Conversely, the hole-selective layers perform opposite functions [34].

This principle translates into the SHJ design, where amorphous silicon (a-Si) layers provide both electrical selectivity and chemical passivation, optimizing carrier separation and reducing recombination losses.

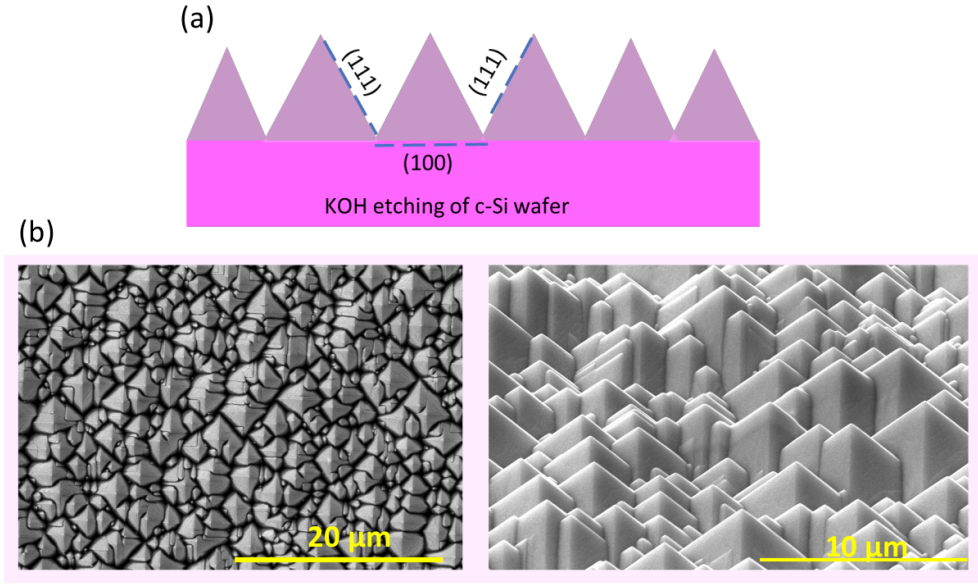

Figure 2.7: *Etched of silicon oriented along the (100) plane and textured along the (111) plane (a). SEM images of the top view of the textured SHJ solar cell(b).*

The a-Si:H bulk and a-Si:H/c-Si interfaces encounter a similar energy barrier for the reduction of deep defects. This observation substantiates the hypothesis that the defects influencing a-Si:H/c-Si interface recombination are silicon dangling bonds (DB). Notably, this barrier is independent of film properties. This is distinct from the optimal surface passivation of c-Si achievable by a-Si:H, which is highly dependent on the specific Si-H bonding configuration within the film [35].

Minimizing recombination losses is essential for improving the efficiency of SHJ solar cells. Using thin, intrinsic a-Si:H layers, usually just a few nanometers thick, effectively reduces surface recombination by passivating dangling bonds and alleviating defects during the subsequent doping layer deposition [36]. Careful optimization of the a-Si:H layer characteristics and deposition conditions helps achieve this reduction in recombination losses [10]. This includes controlling the hydrogen content, film density, and growth parameters to minimize defect formation and enhance passivation quality. Additionally, post-deposition treatments such as annealing can further improve the interface properties and reduce recombination. These strategies collectively contribute to the development of high-efficiency SHJ solar cells with superior performance characteristics. Carrier recombination at in-

terfaces can significantly reduce solar cell performance. This is often quantified by the interface recombination velocity or surface recombination rate, which should be minimized through passivation techniques. In SHJ cells, intrinsic a-Si:H layers provide both chemical passivation (by terminating dangling bonds with hydrogen) and field-effect passivation (via fixed charges that repel minority carriers).

However, the addition of TCOs can introduce interface states, roughness, or inhomogeneity that degrade passivation quality, and can introduce a high parasitic absorption of the incident sunlight when applied on the front side of the solar cell. This is why precise control over the microstructure and deposition conditions of the TCO and adjacent layers is critical. Advanced contact designs, such as transparent passivating contacts (TPCs), can further enhance interface quality, charge selectivity and overcome the parasitic absorption. The advantage of the TPC includes materials with more transparency and good passivation and conductivity. The principle of TPCs is based on using ultrathin passivating layers like SiO_x in combination with highly conductive transparent layers. The option of TPCs involves finding a wide bandgap material that is transparent to the relevant light spectrum. However, it must also provide good passivation and have an acceptable conductivity level for carrier transport. Silicon carbide SiC is an interesting material that has a wide optical band gap of 2.3–3.2 eV, which is larger as compared to the band gaps of a-Si (1.7 eV) [14, 37, 38].

2.3 Materials and properties

2.3.1 Transparent conductive oxide

TCOs are semiconductor materials commonly utilised in photovoltaic devices due to their wide band gap ($E_g > 3\ eV$). The latter demonstrates considerable transparency in both the visible and near-infrared spectral regions, along with high electrical conductivity ranging from 10^3 to 10^4 Scm^{-1} [39]. This unique trade-off in opto-electrical properties makes transparent conductive oxides highly interesting for a wide range of applications, including flat panel displays, optical coatings, and photovoltaic devices. In solar cells, TCO is utilised to maximize the number of photons reaching the device's absorber while minimizing resistance losses caused by the electronic transport of charge carriers from the absorber to the silver grid. In this section, the basic electrical and structural properties of TCOs will be addressed, with a specific focus on aluminium-doped zinc oxide ($ZnO:Al_2O_3$)

and Indium tin oxide (In_2O_3:SnO_2), which will be the most intensively investigated TCOs in this work. It is worth mentioning that most of the equations in this section are from these references [40–42].

2.3.2 Electrical conductivity

For application as an electrical contact, a high conductivity is a key parameter for TCO materials. Due to the large band gap, the charge carrier density of undoped zinc oxide (ZnO) is relatively low with $10^{17} cm^3$ [43]. However, it can be increased through either n-type or p-type doping. In the case of n-type doping, free electrons can be generated by altering the stoichiometry and dopants of the film [44]. Resulting oxygen vacancies or interstitial metal atoms lead to excess electrons with low energies for excitation to the conduction band. However, an increasing number of oxygen vacancies reduces the transparency of the film and is therefore undesirable. The dopant concentration is limited by the solubility of the impurity atom in the metal oxide lattice. Above a certain carrier concentration, the donor levels are shifted into the conduction band and the material becomes degenerated. In this case, no energy is needed to excite electrons into the conduction band, and the electrons can be treated as a free electron gas, such as in metals. For ZnO, this is the case for $N > 5 \times 10^{18}\ cm^{-3}$ [43].

The electrical conductivity of a material can be described as follows:

$$\sigma = q(N_n \mu_n + N_p \mu_p) \tag{2.1}$$

where q is the elementary charge, $N_{n/p}$ and $\mu_{n/p}$ are the carrier density and carrier mobility of electrons and holes, respectively. Accordingly, the electrical conductivity of a TCO can be increased by enhancing the carrier density and/or mobility of charge carriers in the material. In n-type TCO, the contribution from positive charges, and thus the right term in the bracket, can be neglected [45]. From that, the conductivity becomes:

$$\sigma = N_e e \mu_e \tag{2.2}$$

where the e is the elementary charge of the electron. In the other hand, the resistivity ρ of an electrical conducting material, which is defined as the inverse of the conductivity, is given by:

$$\rho = 1/N_e e \mu_e \tag{2.3}$$

In order to calculate the resistance of a TCO layer, the geometry of the layer has to be taken into account. The resistance of a geometric conducting body is inversely proportional to its width and height it and proportional to its length.

$$\rho_{sh} = 1/N_e e \mu_e (L/WH) \tag{2.4}$$

Where W and H are the width and height, respectively, and L is the length of the conducting body. Since TCOs are normally deposited as thin films on the front contact of solar cells, another quantity, called sheet resistance, is used to characterize them. The sheet resistance of a TCO is defined

$$\rho_{sh} = 1/N_e e \mu_e d \tag{2.5}$$

Where d is the thickness of the TCO layer. Now, if the conductivity of these types of materials is to be increased, either the concentration of charge carriers, the mobility or the thickness of the layer has to be increased. Each of these parameters can be adjusted to find an optimum value for the conductivity of the TCO layer.

2.3.3 Transport mechanisms

The high carrier concentrations and high mobilities in the TCO films contribute to their low resistivities. However, a high charge carrier concentration results in the absorption of light at infrared wavelengths. Additionally, heavy doping in the films could lead to reduced electron mobility due to the higher presence of scattering centers such as ionized dopant atoms [41]. From that, several phenomena can restrict electron mobility:

1. Ionized impurity scattering (μ_i): Ionized impurities such as oxygen vacancies, dopants, or excess metal atoms are common in heavily-doped TCOs. In degenerated semiconductors, such impurities serve as powerful electron scattering centers, where scattering typically increases at higher charge carrier density.
2. Neutral impurity scattering (μ_n): It is the scattering induced by the neutral impurities, such as atoms. This scattering plays a minor role in heavily-doped TCOs.
3. Scattering at grain boundaries (μ_g): It is the scattering caused by disordered atoms present at the boundaries of regions with differing lattice orientations in polycrystalline materials. This results in incomplete atomic bonding and, as a result, a

significant defect density. The electron current through the TCO is disrupted when electrons become trapped in these defects, thus creating a potential barrier. The electron transport through these potential barriers can be caused by three distinct mechanisms: field emission (tunneling), thermionic emission and thermionic field emission (a combination of field emission and thermionic emission) [46].

4. Lattice vibration scattering (μ_l): At increasing temperatures, there is a general rise in the lattice vibration scattering. As the lattice vibration increases, the lattice may deform. This gives rise to acoustic phonon generation, in turn inducing scattering that limits the mobility of electrons.
5. There are other scattering mechanisms which cause electron scattering, such as piezoelectric scattering, dislocation scattering, etc. The scattering effects on the electron mobility can be described by the equation:

$$1/\mu = 1/\mu_i + 1/\mu_n + 1/\mu_g + 1/\mu_l + ... \tag{2.6}$$

Accordingly, scattering processes limit the electronic transport. Amongst others, the main mechanisms in zinc oxide are scattering at ionized impurities, such as intrinsic lattice defects or extrinsic dopants and scattering at grain boundaries.

In case of scattering at ionized impurities, the electrical field of ionized impurities disturbs the electronic transport and correspondingly, scattering increases with increasing dopant concentration and thus n. On the other hand, the grain boundaries consist of a disordered phase and thus present a potential barrier for charge carriers. The probability of overcoming this barrier, and consequently the mobility of charge carriers, increases with increasing n. Due to the opposing trends with n, ionized impurity scattering dominates the electronic transport and thus mobility for ZnO films exhibiting $n > 10^{20}$ cm^3, while at lower charge carrier densities, scattering at grain boundaries dominates the mobility in polycrystalline TCO films [40, 46].

2.3.4 Aluminium-doped zinc oxide

ZnO has gathered considerable interest due to its three distinct phases: wurtzite, zinc blend, and rock salt. The wurtzite phase, part of the hexagonal crystal system, exhibits greater stability and resistance to radiation under normal conditions [47]. The ZnO wurtzite structure consists of two interlaced hexagonal close-packed arrangements. This

configuration results in each zinc atom being surrounded by four oxygen atoms in a tetrahedral shape, and vice versa. The Zn-O bond is primarily ionic; these polar bonds lead to planes of positively charged zinc and negatively charged oxygen atoms perpendicular to the c-axis. The four most common face terminations of wurtzite ZnO are the polar Zn-terminated (0001) and O-terminated (000-1) faces c-axis oriented, and the non-polar (11-20) a-axis and (10-10) faces, which both contain an equal number of Zn and O atoms. The combination of a lack of inversion symmetry and the polarization of the atomic planes gives ZnO the properties of being both piezoelectric and pyroelectric [47–49].

Typically, ZnO is doped with group III elements such as aluminum (Al), boron (B), and gallium (Ga), with Al being the most common donor dopant. Al doping introduces additional electrons into the structure, providing n-type doping and enhancing the conductivity of the material [44]. However, the mobility of these charge carriers is limited by factors such as ionized impurity scattering and grain boundary effects in polycrystalline films, as discussed in the last section. The carrier mobility in AZO ranges from 10 to 50 cm^2/Vs, which is lower than that of ITO due to the larger grain boundary density in ZnO-based films. When a thin film of AZO is grown on a silicon substrate, it preferentially crystallizes in a hexagonal wurtzite shape. The x-ray diffraction (XRD) analysis revealed that the growth of AZO occurred along the c-axis perpendicular to the substrate, with the (0002) plane becoming apparent. The AZO crystal structure, which belongs to the space group P63mc [50]. **Figure 2.8 (a,b)** shows the crystal model of the hexagonal wurtzite of the AZO. AZO has been increasingly explored as a TCO layer in SHJ solar cells. This interest stems from AZO's remarkable properties of AZO, including favorable electrical characteristics and a wide bandgap, as indicated in the **Table 2.1**.

2.3.5 Indium-doped tin oxide

Indium oxide (In_2O_3) is an n-type semiconductor that exhibits exceptional electrical and optical characteristics, making it suitable for optoelectronic and sensing applications [51]. In_2O_3 crystallizes in three main polymorphic structures: rhombohedral corundum structure (space group R3c), a cubic bixbyite structure (space group Ia_3) [52, 53]. The most common one is the latter, where typically indium (In) atoms are encircled by oxygen (O) atoms. ITO is a composite material in which In atoms substitute tin (Sn) atoms in the tin oxide (SnO_2) lattice, which contributes free electrons due to two sources intrinsic oxygen vacancies and extrinsic electron-donor dopant Sn_4^+ ions substituting for In_3^+ ions [54].

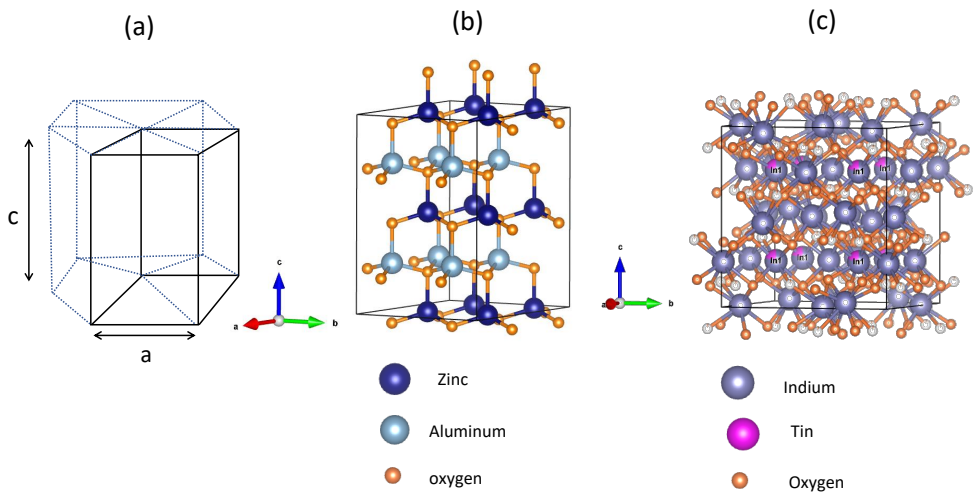

Figure 2.8: *The hexagonal wurtzitel lattice is characterized by two lattice constants: a and c in (a), crystal structure hexagonal wurtzite model of AZO (b) and cubic bixbyite ITO (c), the crystal models of AZO and ITO can be visualised using the VESTA software tools.*

The crystal structure of ITO has a space group symmetry of Ia3. **Figure 2.8** shows the crystal model of the cubic bixbyite ITO. ITO possesses a higher carrier mobility, typically between 20 and 60 cm^2/Vs, due to the lower density of grain boundaries and fewer ionized impurities in its crystalline structure. Factors such as the indium doping level, deposition technique, annealing temperature, and film thickness can affect the crystallinity, surface morphology, and overall performance of ITO films. It demonstrates low resistivity (10^{-4} to 10^{-3} $\Omega \cdot cm$) and high optical transparency (80-90%) in the visible spectrum, making it an ideal electrode material for photovoltaic and display technologies [54]. ITO thin films have been deposited using vapor transport deposition techniques, such as the chemical vapor deposition system, magnetron sputtering, and vacuum evaporation method [55, 56].

Table 2.1: *Values of the band gap and crystal lattice parameters of Si, AZO, ITO and nc-SiC.*

Material	Bandgap (eV)	a (Å), b (Å)	c (Å)
c-Si	1.12	5.431	5.431
AZO	3.46–3.54 [47]	3.249	5.206

Table 2.1: *Values of the band gap and crystal lattice parameters of Si, AZO, ITO and nc-SiC.*

Material	Bandgap (eV)	a (Å), b (Å)	c (Å)
ITO	3–3.4 [51, 53]	10.117	10.118
nc-SiC (6H-SiC)	2.0-3.3 [57]	3.081	15.124
nc-SiC (3C-SiC)	2.0-3.3 [57]	4.348	4.348

2.3.6 Silicon carbide

Silicon carbide (SiC) is a compound semiconductor composed of Si and C, which has several advantageous properties such as a wide bandgap, high carrier mobility, and high conductivity for both n- and p-type doping. Structurally, SiC exists in more than 200 different polytypes, which vary in their crystal structure. The most common polytypes are 3C-SiC (cubic), 4H-SiC, and 6H-SiC (hexagonal) [57]. These polytypes differ in their stacking sequence of silicon and carbon atoms, resulting in different electronic and physical properties. High-quality SiC is produced at substrate temperatures exceeding 1000 °C; however, achieving material growth at lower temperatures has been pursued for years. Significant epitaxial growth has been attained at approximately 700°C. However, this temperature is still too high for applications in thin-film solar cells on cheap glass substrates [58]. Unlike bulk SiC, which exists in several polytypes with distinct bandgaps and crystal structures, μc-SiC consists of nanometer to micrometer-sized crystalline grains embedded in an amorphous or polycrystalline matrix. The electrical behavior of μc-SiC is influenced by its band structure, carrier transport mechanisms, and defect-related recombination processes. The bandgap of microcrystalline SiC varies depending on its composition and crystallinity, see **Table 2.1**. This wide bandgap makes μc-SiC more resistant to thermal excitation than silicon. The electrical conductivity of μc-SiC is highly dependent on doping concentration and grain boundary effects. Intrinsic microcrystalline SiC has a relatively high resistivity due to its low intrinsic carrier concentration, but by introducing dopants such as nitrogen (for n-type conduction) or aluminum/boron (for p-type conduction), the carrier concentration can be increased significantly.

2.4 Microscopy techniques

In modern materials science, the advancement of microscopy techniques has expanded the scope of microstructural analysis from the micrometre scale down to the sub-nanometer level. This progress is particularly critical for energy materials and thus thin-film solar cells, where subtle variations at the interface between c-Si and a-Si:H can dramatically influence device performance. Additionally, due to the growth behaviour of materials used in the front and back contacts, particularly the TCO materials, variations in grain size, grain boundaries, and crystallographic orientation within TCO films can impact charge carrier mobility, resistivity, and fill factor, ultimately affecting the device's final performance.

To gain a clearer understanding of nanoscale phenomena and To effectively address the challenges inherent in modern materials research, advanced microscopy techniques have become indispensable. The principal advantage of electron microscopy lies in its exceptional spatial resolution, enabled by the extremely short wavelength of electrons. This wavelength, which depends on the accelerating voltage, typically ranges from 100 to 1500 kV, can fall between approximately 4 and 0.3 pm (picometers), which is significantly smaller than the wavelength of visible light (400–700 nm) [59]. This physical advantage allows electron microscopes to resolve features at the atomic scale, surpassing the diffraction limits of optical systems [60, 61]. High-resolution tools such as scanning transmission electron microscopy (STEM), when combined with analytical techniques like energy-dispersive x-ray spectroscopy (EDX) and Electron energy loss spectroscopy (EELS), enable detailed visualization of compositional variations and the ability to map a large range of elements with high spatial resolution. Atom probe tomography (APT) further enhances this capability by providing near-atomic spatial and compositional resolution, making it particularly useful for identifying dopants or impurities in semiconductor materials [62]. Complementary methods, such as Secondary Ion Mass Spectrometry (SIMS) and time-of-flight SIMS (ToF-SIMS), allow for depth profiling of elemental concentrations, revealing diffusion profiles and contamination layers that influence electronic behavior [63].

Despite these powerful capabilities, high-resolution microscopy has significant limitations. A primary concern is the complexity of the sample preparation. For techniques such as TEM, a certain thickness of the sample must be prepared, often below 50 nm, to allow sufficient electron transmission. This preparation can be both time-consuming and technically demanding, with a high risk of introducing artifacts that may distort the structural or compositional information. Moreover, these instruments are expensive and require

dedicated infrastructure, including vibration isolation, high-vacuum systems, and environmental controls. Operation and data interpretation demand considerable expertise, often limiting access to specialized laboratories [64]. Furthermore, high-energy electron beams used in TEM can damage sensitive materials, especially soft matter or beam-sensitive compounds such as hybrid perovskites or polymers, leading to structural degradation or elemental migration [65]. Another intrinsic limitation is the narrow field-of-view, which may restrict the statistical representativeness of the results, particularly for heterogeneous materials. Furthermore, conventional TEM provides only two-dimensional projections of three-dimensional structures, which can obscure critical spatial relationships, unless advanced methods such as electron tomography are employed [66].

3 Methods and sample preparation

This chapter introduces TEM, the main technique employed in this thesis. We focus on the imaging mode and electron diffraction technique for orientation mapping. Second, a brief description of the EDX and EELS as analytical techniques is provided to verify and complement the results obtained from the imaging and orientation mapping methods. The specimen preparation methods, including conventional and focused ion beam techniques, are described in the fourth section. Finally, the experimental details of this thesis are introduced.

For TEM specimen preparation, I refer the reader to the texts and review articles of [67]. Further information on TEM techniques can be found in Williams and Carter (2009) [61], Nobuo Tanaka's Electron Nanoimaging [68], as well as Thomas and Gemming's Analytical Transmission Electron Microscopy (2013) [69].

3.1 Transmission electron microscopy

3.1.1 Background

Rayleigh and Abbe demonstrated that the resolution of an optical microscope equipped with a glass lens is restricted by the limitation of the light wavelength, specifically the restriction of light diffraction [70]. The limit is defined as follows:

$$d = 0.61\ \lambda /\ \theta \tag{3.1}$$

where λ is the wavelength of the light and θ is the total angle subtended at the sample by the circular lens aperture [70]. The ability to distinguish and observe the shortest distance between two closely placed objects is known as point resolution or resolving power [71]. This capability is crucial in optical instruments and microscopes. The human eye

can perceive objects 0.1-0.2 mm apart [68]. Thus, any instrument showing details thinner than 0.1 mm is considered a microscope, and its highest magnification level determines its usefulness. The information limit is the highest spatial frequency that can be transferred to an image with statistical significance. For example, under a light microscope, more light can be captured by using an objective lens with a larger numerical aperture. This, in turn, provides a higher resolution. The theoretical limit of the resolution of a light microscope is approximately 200 nm. Even with improvements such as phase-contrast and fluorescence microscopy, optical techniques cannot resolve features smaller than 200 nm due to the diffraction limit.

In 1925, Louis de Broglie [72] proposed a hypothesis regarding the dual-wave/particle nature of an electron. The latter equation enables the production of electrons with wavelengths much shorter than those of visible light. Shortly after, electron diffraction experiments provided evidence of the wave nature of electrons. The next major step was taken by the physicist Hans Busch in 1927, who developed an electromagnetic lens incorporated into the first TEM. The development of electron lenses has had a significant impact on various fields such as nanoscience, materials science, energy, and nanotechnology. After developing electron lenses, Ernst Ruska invented the first electron microscope (EM) in 1931 [61]. This was a significant improvement over the best optical microscope available at the time [73, 74]. Soon after, in 1938, von Ardenne developed the STEM. **Figure 3.1** presents the historical development of microscopy resolution, illustrating how advancements in electron optics, aberration correction, and imaging technology have significantly improved our ability to study materials at the atomic scale [75].

3.1.2 Principles of electron imaging

In the following, we will give a theoretical description of imaging microscopy with electrons and how transmission electrons can be used to form atomic images based on the theory of electron-wave daul behavior [68]. According to De Broglie's theory, which is the principal idea for imaging in the TEM, the wavelength λ for electrons can be calculated using:

$$\lambda = \frac{h}{P} \tag{3.2}$$

The momentum in classical theory is given by $P^2 = 2mE = 2m_0$ (e.U_0), however, because the electron is accelerated with high voltage, it has to be treated with the relativistic theory

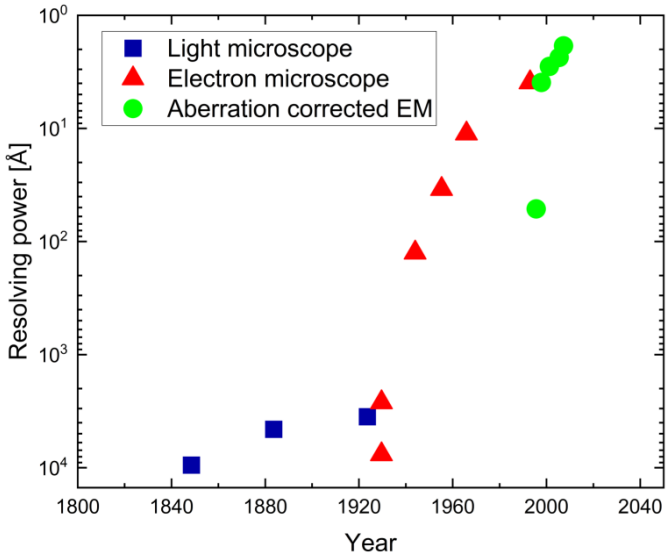

Figure 3.1: *The development of microscopy resolution during the years, adapted from H. Rose [75].*

and by defining the relativistic lorentz factor $\gamma = \frac{U}{2}(1 + \frac{eU}{m_0c^2})$ then the momentum will become $P = \sqrt{[2m_0E\left(1 + \frac{E}{2E_0}\right)]}$

The electrons are generated and accelerated from the electron gun with potential energy U, so the wavelength λ of the resulting electron wave in **Equation 3.2** is given by:

$$\lambda = h/\sqrt{2m_0eU(1 + \frac{eU}{2m_0c^2})} \tag{3.3}$$

where, $h = 6.6256 \times 10^{-34} Nms$ is Plank's constant, $E_0 = m_0c_2$, $E_0 = 0.511MeV$ the energy corresponds to the rest mass of the electron $m_0 = 9.1091 \times 10^{-31} Kg$, $c = 2.9979 \times 10^8 ms^{-1}$. When the relativistic effect is not considered, the wavelength equation becomes $\lambda = h/\sqrt{2m_0eU}$.

Equation 3.3 gives us the wavelength based on the accelerating voltage used in the experiment as follows:

$$U = 200\ kvat\ \lambda = 2.51\ pm \tag{3.4}$$

Theoretically, because of the very short wavelength of electrons in the picometer pm

range ($pm = 10^{-12}m$), the spacing between atoms in a solid is approximately a hundred times larger, so that the electrons are diffracted and the atoms act as a diffraction grating [76].

Table 3.1 Summarize the accelerating voltage used in the microscope and the corresponding electron wavelengths, highlighting the relationship between electron energy and its associated wavelength based on relativistic electron wave theory.

Nevertheless, most microscopes suffer from lens focusing imperfections, which reduce the spatial resolution compared to that indicated in **Equation 3.4**, even when optimally focused. In reality, there are more than tens of different types of aberrations in TEM lenses that impose limitations on the final resolution. Examples include Defocus ($\delta f = C_1$) first order, spherical aberration (C_s) third order, chromatic aberration (C_c) and astigmatism.

The defocus can be changed by adjusting the current in the objective lens coils. The defocus moves the Gaussian image plane up or down by a distance z. A higher lens excitation ($z > 0$) corresponds to an overfocus setting, the focus setting is at ($z = 0$), while a lower lens excitation ($z < 0$) corresponds to an underfocus setting. In analogy to spherical aberration, defocus causes blurring of an ideally sharp object point in the image plane.

Table 3.1: *Electron wavelengths at 5, 10, 200, and 300 KV, and light wavelength.*

Voltage (KV)	Wavelength (nm)
5	0.00173
10	0.00122
100	0.00370
200	0.00251
300	0.00197
light	400-700

Scherzer (1949) calculated image contrast by summing the amplitudes of waves along with their phases. He derived key parameters such as resolution, optimum aperture angles, and the best amount of defocus for observing a single atom, which are essential equations for High resolution TEM (HRTEM) theory [68]. **Figure 3.2** presents common lens aberrations in TEM. These aberrations limit the achievable resolution and image qual-

ity. **Figure 3.2(a)** presents the C_s that occurs when electrons passing through the outer zones of the lens are focused at a different point than those near the optical axis, leading to a blurred image, whereas **Figure 3.2(b)** presents C_c arising due to energy dispersion; electrons with different energies are focused at different image planes, also resulting in image blur. **Figure 3.2(c)** presents that Astigmatism is caused by asymmetries in the electromagnetic field of the lens, leading to different focal lengths in orthogonal directions and producing an image that is stretched or distorted.

Correcting these aberrations is crucial for achieving high-resolution imaging in modern TEM systems [77, 78]. To overcome the inherent resolution limits of electron microscopes, a novel strategy emerged around the 1970s aimed at correcting the aberrations of electron lenses. One of the earliest concepts was introduced by Hardy in 1967, proposing the combination of magnetic and electrostatic quadrupole electron lenses. A significant breakthrough came in 1995 when Haider et al. successfully demonstrated spherical aberration correction in TEM [79].

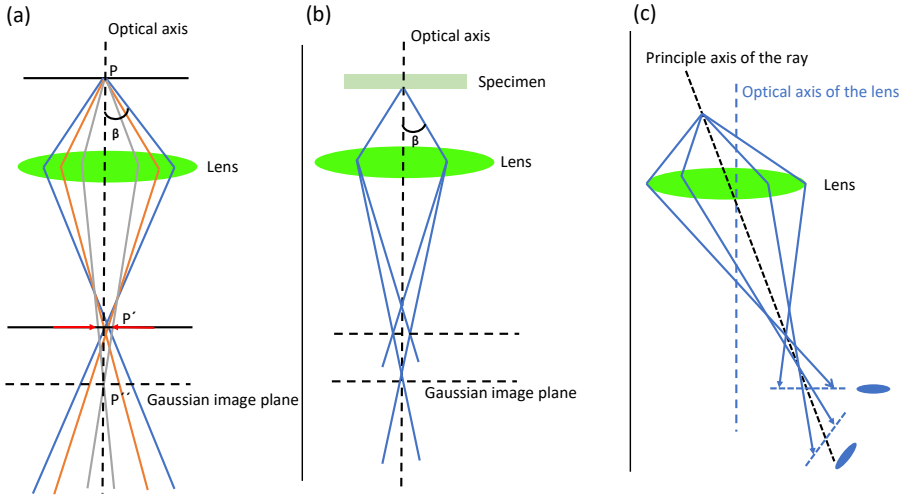

Figure 3.2: *(a) Spherical aberration(b) Chromatic aberration (c) Astigmatism.*

In addition to spherical aberrations, chromatic aberration caused by energy dispersion among incident electrons poses a major challenge to achieving high resolution. This aberration can be mitigated by minimizing the spread in electron wavelengths, which is achieved through the use of a monochromator. A monochromator acts as an energy filter,

effectively narrowing the energy distribution of the electron beam. Pioneering work in this area includes contributions by Hely [80], Hardy [81], and Koops et al. [82]. Modern TEM systems equipped with advanced monochromators are capable of reducing the energy spread to less than 0.2 eV at an accelerating voltage of 200 kV, as demonstrated by [83]. When combined with aberration correctors, these technological advances enable state-of-the-art TEMs to reach an information limit as fine as 50 pm, allowing for unprecedented spatial resolution in materials characterization [79].

3.1.3 TEM setup and components

A conventional TEM typically consists of several key components arranged in a vertical column from top to bottom. These include [74, 84]

1. Electron source
2. Illumination system
3. Specimen stage
4. Objective lens
5. System of intermediate and projector lenses, and a viewing screen.

Starting from the top of the TEM, where the electrons are emitted from the electron source or the so-called electron gun, which can be realized in different types [85]: Thermionic emission using tungsten (W), and lanthanum hexaboride (LaB6), field emission gun (FEG) using an intense electric field, and schottky field emission gun, which is a combination of both types of sources. Following that, the electrons are accelerated by the high voltage applied, typically 80-300 kV, depending on the type of microscope, and travel through the illumination system, typically consisting of two or more condenser lenses C1 and C2, where electromagnetic coils generate rotationally symmetric magnetic fields that focus the electron beam. Below the specimen, an objective lens forms images and diffraction patterns, and the next lens is an intermediate lens, which is important for projecting either a diffraction pattern or an image on the viewing screen. Finally, the images are recorded using a camera or digital detector and processed using imaging software. The electrons are first converted to photons because, until now, the devices that detect photons are more effective than the ones that detect electrons directly. The software allows contrast and brightness adjustments and stitches multiple images together to create larger images on a viewing screen [59, 61].

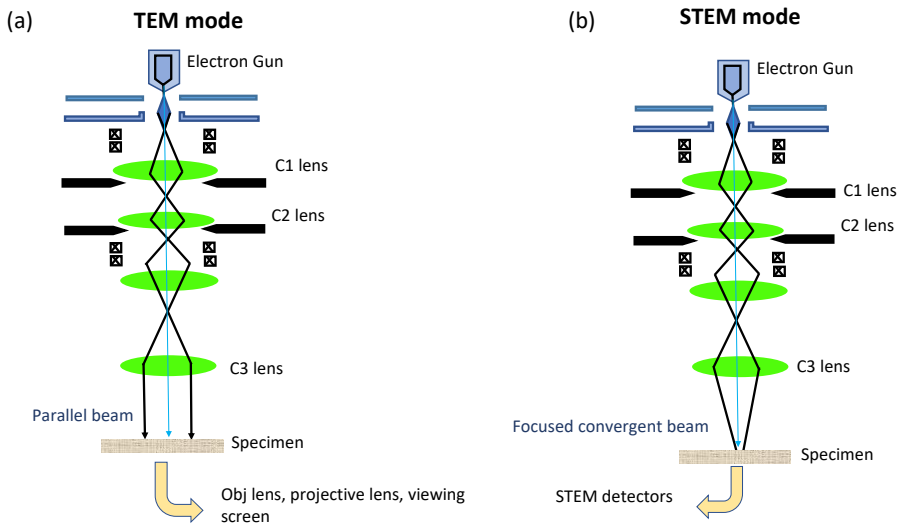

Figure 3.3: *Schematic diagram of the beam formation optics in TEM vs STEM.*

Improved capabilities in analytical TEM are achieved by incorporating components like aberration correctors, monochromators, and energy filters, along with various attachments to the electron column[74]. These attachments feature 2D pixel array detectors for both electron imaging and diffraction, bright-field/annular dark-field detectors for STEM, an EELS, an EDX detector, and an electron biprism for electron holography. The inclusion of EDX and EELS offers significant compositional insights essential for analysing diffraction data [60, 86].

The precise adjustment of the condenser lens system can create either a parallel or convergent illumination beam, each resulting in different spot sizes on the sample. For example, scanning lenses enable the shifting and tilting of the electron beam to align with the optical axis immediately before reaching the sample, which facilitates the scanning TEM (STEM) mode. When creating a focused probe, the electron beams are projected onto the sample through a probe-forming lens. **Figure 3.3** presents the difference between the TEM mode and the STEM mode [68]. Parallel beam illumination produces sharp spots, and converged beam illumination produces disks at the back focal plane of the objective lens. The size of these disks depends on the convergence angle, as we will see later in this chapter.

3.1.4 Electron interaction with sample materials

Electron propagation can be described using the concept of a wave package. A stationary plane wavefunction that propagates in the r direction, r =(x,y) is in two dimensions:

$$\psi(\mathbf{r}) = \psi_0 e^{2\pi k\mathbf{r}} \tag{3.5}$$

Where (ψ_0) is the amplitude, k is the wave vector, and ($2\pi kr$) is the phase wave.

The electron wavefunction in the image plane, the so-called image-plane wavefunction, is recorded by the detector system as an intensity distribution. The intensity I(r) in the image is given by the modulus square of the image-plane wavefunction $\Psi(r)$ and the complex conjugates ($\psi^*(\mathbf{r})$), with:

$$I(\mathbf{r}) = \psi(\mathbf{r}\psi^*(\mathbf{r})) \tag{3.6}$$

The electron's wave function propagating through the sample is modified by the interaction with the matter.

Electron scattering can be categorized into two types: **elastic** scattering, where electrons do not lose energy, and **inelastic** scattering [85], where energy loss occurs, generating signals like secondary electrons (SE), backscattered electrons (BSE), and characteristic x-rays. Secondary electrons are low-energy particles released from the sample surface, yielding high-resolution topographical data. Backscattered electrons, being of higher energy, respond to atomic number variations, providing compositional contrast. Characteristic x-rays result from the substitution of displaced inner-shell electrons by high-energy electrons, enabling elemental analysis through methods such as EDX. Furthermore, during the relaxation of excited atoms, Auger electrons may be emitted, offering surface-specific chemical insights. Together, these signals facilitate in-depth characterization of a sample's structure, composition, and electronic structure, rendering electron-based methods crucial in materials science, chemistry, and biology [86]. **Figure 3.4** demonstrates the interactions of electrons with the sample and the resulting signals. Despite these interactions, most encounters between the beam electrons and sample atoms are primarily elastic; during transit through the sample, electrons are mainly scattered by the nucleus, which can produce imaging or diffraction information due to elastic scattering [59]. The probability that an electron will be elastically scattered by an isolated atom is given by the scattering

cross-section:

$$\delta\sigma(\theta)/\delta\Omega = (\frac{Z^2e^4}{E_0^2\theta^4}) \tag{3.7}$$

where Z is the atomic number, e is the elementary charge, V is the potential of the incoming electron, and θ is the scattering angle. As a result of scattering, the intensity of the transmitted beam decreases, but new waves propagating in different directions arise. This phenomenon is a consequence of the interaction between the electron and the Coulomb potential of the atomic nucleus, which deflects the electron from its original path. The scattered waves interfere with each other, leading to a diffraction pattern that provides information about the atomic structure of the material. The scattering cross-section σ quantifies the likelihood of this interaction and depends on the energy of the incident electron and the scattering angle θ. For small angles, the cross-section is larger, indicating a higher probability of scattering, while for larger angles, the probability decreases. This relationship is crucial in techniques such as electron microscopy and x-ray diffraction, where scattering patterns are analyzed to determine the arrangement of atoms in a sample[85].

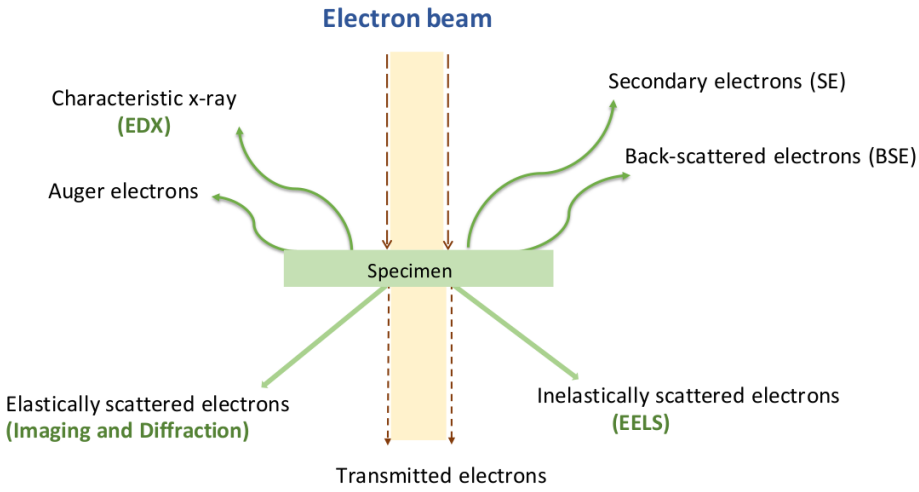

Figure 3.4: *Signals were generated by the interaction of a beam of high energy electrons with a thin specimen; modified from [61].*

3.1.5 TEM modes and contrast

The image formation from the electron beam can be of different types based on the lies of the image: imaging and diffraction modes.

In TEM imaging mode, the electron beam transmitted through a thin specimen interacts with the atomic planes of the material, causing a portion of the electrons to be diffracted. The objective lens then forms an image from the transmitted and diffracted electrons in the image plane. In contrast, in diffraction mode, electrons scattered at the same angles are focused into identical positions in the back focal plane of the objective lens, producing a diffraction pattern. This pattern represents the reciprocal-space information of the specimen and is projected onto the TEM CCD by imaging the back focal plane.

Imaging mode provides a magnified and focused real-space image of the specimen. Image contrast in TEM arises from variations in electron–matter interactions across different regions of the sample. Contrast is defined as the visibility of features within an image and can originate from several mechanisms, including diffraction (amplitude) contrast, phase contrast, and Z-contrast. **Figure 3.5** show the diagrams for the imaging (right) and diffraction (left) operation mode in the TEM.

Diffraction contrast is achieved by inserting an objective aperture into the back focal plane of the exit wave, thereby restricting the electrons contributing to image formation to a selected region of reciprocal space. This selection primarily includes electrons that have undergone elastic scattering within the specimen. When the aperture is centred on the transmitted beam, the resulting image is known as bright field (BF) image. When the aperture is displaced to select a diffracted beam, a a dark field (DF) image is formed. If no objective aperture is used, the image generally exhibits mass–thickness contrast, which increases with both specimen thickness and atomic number. This contrast arises mainly from elastic scattering at individual atoms, where incident electrons are deflected by Coulomb interactions as they pass through the specimen [64].

The HRTEM allows both transmitted and diffracted beams to pass through the objective aperture and typically operates under phase-contrast conditions. In this mode, structural information is encoded in the phase of the elastically scattered electron waves. To convert these phase variations into observable intensity differences, an additional phase shift must be introduced so that the phase difference between scattered and unscattered waves approaches 180°. In conventional TEMs, this phase shift is commonly achieved by intentionally defocusing the objective lens, as described by Scherzer [78].

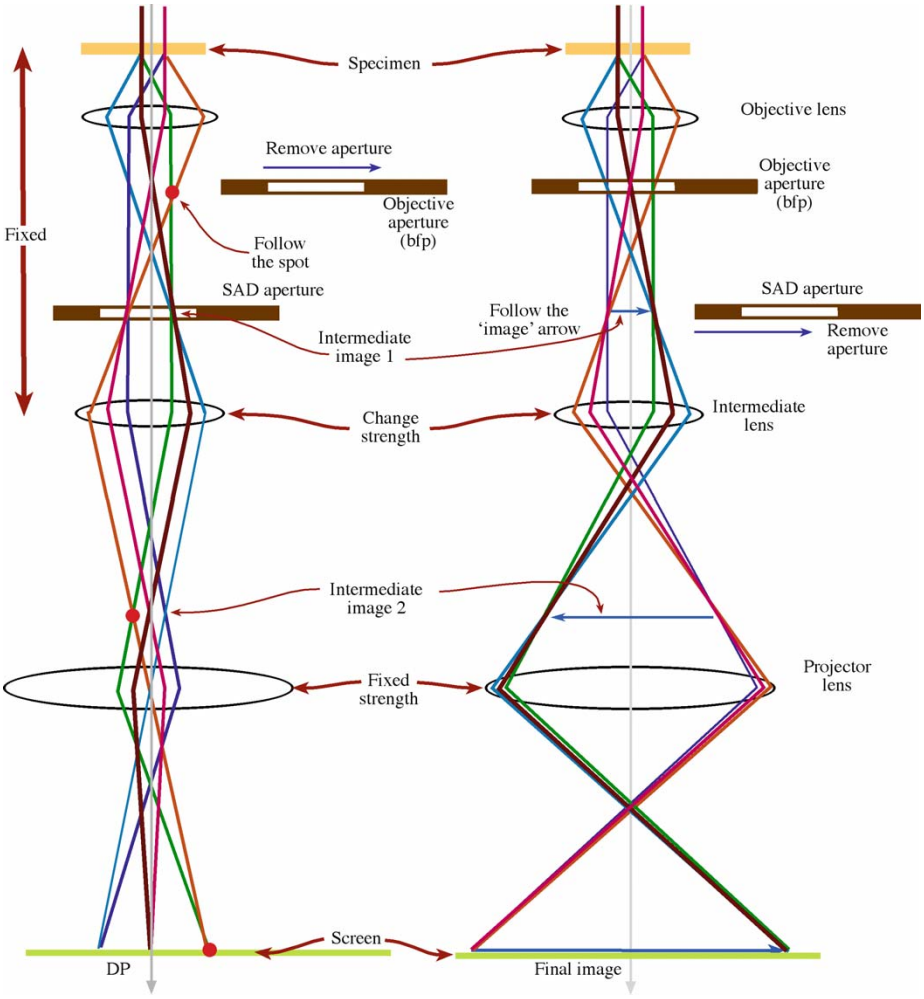

Figure 3.5: *Illustrates the ray diagrams for the diffraction (left) and imaging (right) operation modes in a TEM, adapted from [61]*

3.2 Scanning transmission electron microscopy (STEM)

In STEM, a finely focused electron probe with a diameter smaller than 1 Å is rastered across a thin specimen. The achievable spatial resolution is primarily limited by aberrations in the probe-forming lenses. With the development of aberration-corrected electron optics, spatial resolutions below sub-50pm have been achieved [76, 78]. STEM imaging makes use of both elastically and inelastically scattered electrons that have interacted with and passed through the specimen. The scatter collection angle (β) in (mrad) plays a critical role in image formation and interpretation; for reference, 1 rad corresponds to approximately 57 °. The principal STEM imaging modes, classified according to the scattering angles collected by the detector, are shown schematically **Figure 3.6** [87].

By selecting different ranges of scattering angles, STEM enables a variety of imaging modes, each characterized by distinct contrast mechanisms. When incoherently scattered electrons at high angles are collected, the resulting image is referred to as a high annular dark-field (HAADF) STEM image. In this mode, image contrast is governed by the efficiency of the Rutherford scattering process at the selected collection angles and is approximately proportional to the square of the atomic number ($\sim Z^2$). At these high angles, phonon-induced thermal diffuse scattering dominates, such that incoherent electrons scattered by thermally vibrating atoms are preferentially collected by the detector, producing monotonic, Z-dependent contrast without interference effects or contrast reversals. As a result, atomic columns appear with high spatial fidelity and are straightforward to interpret. As a result, atomic columns appear with high spatial fidelity and without contrast reversals. Although HAADF-STEM is one of the most widely used imaging techniques due to its intuitive interpretation, it is less suitable for imaging light elements, as Rutherford scattering is relatively inefficient for atoms with low atomic numbers.

Low-angle annular dark-field (LAADF or ADF) STEM collects electrons scattered at lower angles, where scattering remains partially coherent. LAADF images retain several advantages of HAADF imaging, including the absence of contrast inversion and robust interpretability of atomic columns over a wide focus range. In addition, LAADF-STEM is particularly sensitive to strain-related features and is effective for imaging strongly diffracting regions such as dislocations, as well as nanoscale coherent or semi-coherent precipitates.

In Annular bright field (ABF or BF) STEM, electrons within the inner portion of the scattering disc are collected, resulting in images dominated by phase contrast. When combined with image simulations, ABF-STEM has proven effective for visualizing both heavy

and light atomic species. Notably, electrons collected from the outer region of the BF disc contribute to a more incoherent imaging regime, allowing atomic columns including light elements such as oxygen and hydrogen to appear as dark contrast features. BF imaging is well suited for integration with analytical STEM techniques, where localized chemical information is required, and STEM operation is generally preferred for such analyses [88].

In STEM diffraction mode, a pixelated detector is used to record the diffracted probe after interaction with the specimen. Diffraction acquired at a single probe position is commonly referred to as convergent beam electron diffraction (CBED) or microdiffractio. When diffraction patterns are recorded as a function of probe position during scanning, the technique is classified as 4D-STEM, which includes methods such as nanobeam electron diffraction (NBED), scanning electron nano-diffraction (SEND) [59].

In this thesis, multiple STEM detection modes including HAADF and 4D-STEM were employed to generate orientation and phase maps of the investigated materials.

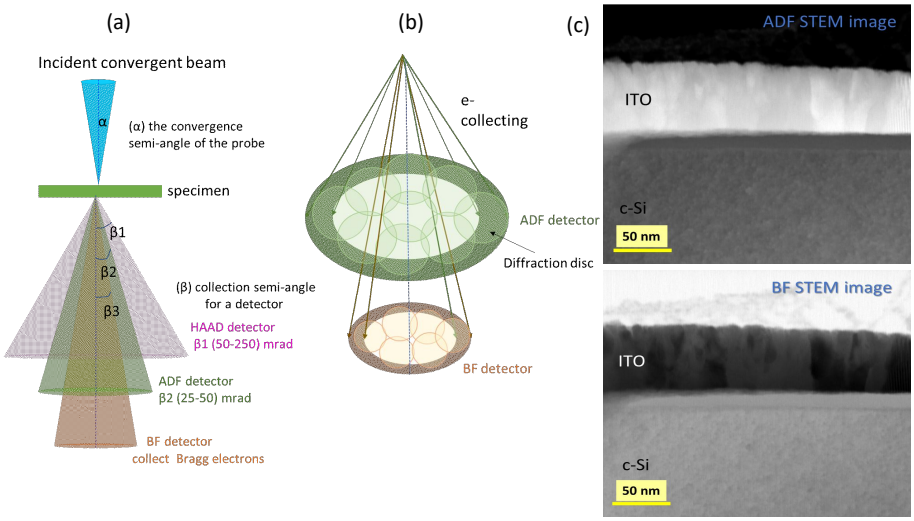

Figure 3.6: *Schematic configuration of STEM detection set-up. Annular DF (ADF), Annular BF and HAAD detectors conditions (a) and (b) the relative positions of the ADF and ABF detectors. The LAADF detector (top) forms an annular region capturing scattered electrons at low angles, while the ABF detector (bottom) is more centrally positioned, capturing Bragg-scattered electrons. The corresponding images formed ADF and BF images as in (c).*

3.3 Electron diffraction

The incident electron beam interacts with the atoms in a crystalline specimen and diffracts from the planes within the specimen. Then some of the incident beam are diffracted and the rest are transmitted through the specimen, with each path undergoing specific phase shifts. The constructive interference occurs at specific angles, where the path difference between the scattered electron waves corresponds to an integer multiple 2 π of the wavelength. By applying Bragg's law:

$$n\ \lambda = 2\ d\ sin\ \theta \tag{3.8}$$

Where λ is the wavelength of the electron, n is an integer representing the order of diffraction, d is the interplanar spacing of the atomic structure and θ is the angle of diffraction. **Figure 3.7(a)** presents a diagram illustrating the constructive interference condition as dictated by Bragg's law, wherein the path difference between reflected waves is an integer multiple of the wavelength.

Bragg's law helps understand the intensities associated with diffraction patterns by incorporating the Ewald sphere construction along with the reciprocal space lattice. The reciprocal lattice is an array of points that describes single-crystal diffraction, each points correspond to the particular real plane (hkl) in the crystal lattice. This means that the wave is diffracted if the difference between the diffracted and incident wave vectors equals a reciprocal vector of the lattice g ($|g| = 1/d_{hkl}$), which is called the diffraction vector of reciprocal lattice and it is perpendicular to the plane of the crystal lattice. Diffraction pattern and reciprocal lattice are related to each other, and this relation is used for the interpretation of different diffraction patterns.

As shown in **Figure 3.7(b)**, the Ewald sphere in a reciprocal lattice and the formation of a diffraction pattern are represented geometrically. The relationships between the incident, transmitted, and diffracted beams and the Ewald sphere are drawn. In reciprocal space, the analogue of Bragg's law takes the form of the Laue equation:

$$k_g - k_0 = g \tag{3.9}$$

Where k_g and k_0 are the wave vectors of diffracted and incident waves, respectively. In terms of the Ewald sphere, which has its center (0) at the origin of the incident wave

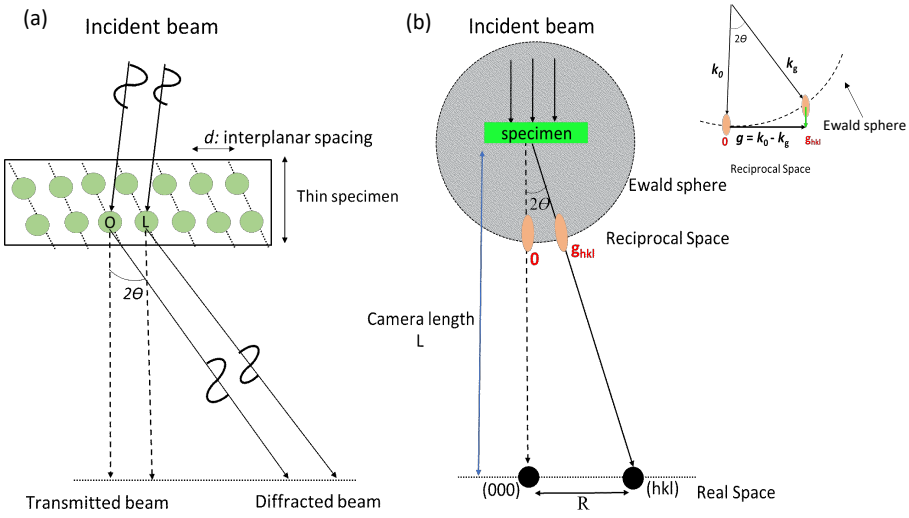

Figure 3.7: *Schematic representation of the constructive interference condition, governed by Bragg's law, where the path difference between reflected waves equals an integer multiple of the wavelength. The Ewald sphere is shown in a reciprocal space with a radius of* $|k_0| = |k_g| = 1/\lambda$. *The formation of a diffraction pattern is shown geometrically in real space. The vectors* k_0 *and* k_g *are the wave vectors of the incident and diffracted beam, and* g *is the reciprocal lattice vector; the dashed black line represents the Ewald sphere.*

vector k_0 and radius $r = |k_0| = 1/\lambda$, diffraction will occur when the Ewald sphere passes through the point in the reciprocal lattice. Again from **Figure 3.7(b)**, the angle between transmitted and diffracted beams is 2θ, R is the distance between the collision points of transmitted and diffracted beams with the screen, and L is the distance between the specimen and the screen, called the camera length.

Using the Bragg law and with the assumption of a small θ, we can equation as follows

$$Rd = L\lambda \tag{3.10}$$

where Lλ is a camera constant. The effective camera length and wavelength of the electron remain constant, influenced by the characterization of transmission electron microscopy.

To obtain lattice fringes in TEM from the previous equations. The integers h, k, and l are named Miller indices in crystallography. For cubic crystals, we have a formula between the lattice constant of unit cell a and the lattice spacing d as follows:

$$d_{hkl} = \frac{a}{\sqrt{h^2 + k^2 + l^2}} \tag{3.11}$$

Selected area electron diffraction (SAED)

When an electron beam illuminates a specimen, it generates both transmitted and diffracted beams, which together form a diffraction pattern seen in the back focal plane of the objective lens. Suppose an aperture is inserted in the image plane, referred to here as the selected area aperture (SAD aperture). In that case, it restricts the beams contributing to the final diffraction pattern seen on the phosphor screen. This aperture allows only electrons passing through a specific region of the specimen to form the diffraction pattern, enabling localized analysis. However, all transmitted and diffracted beams still contribute to the diffraction pattern at the back focal plane; the aperture merely filters which beams are projected onward. This technique, known as SAED, is essential for correlating the microstructure with the crystallographic information. **Figure 3.8(a)** presents the SAED pattern for crystalline silicon and AZO/ITO thin-film solar cells.

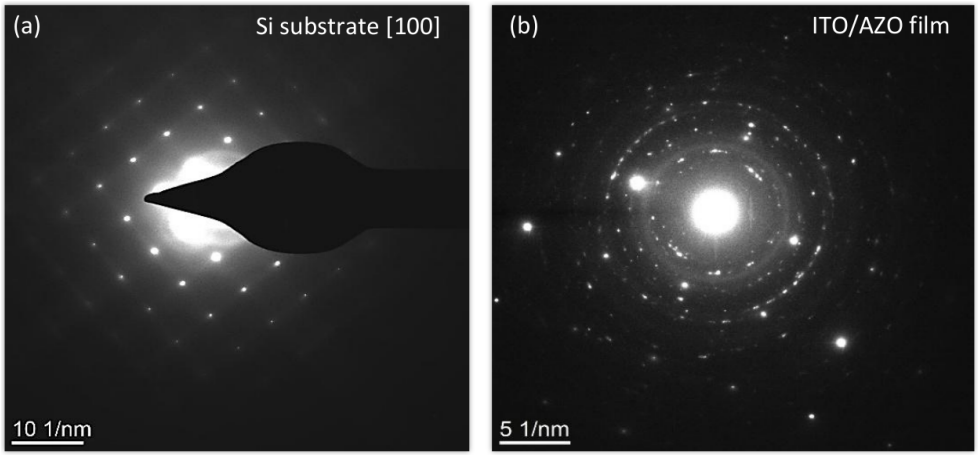

Figure 3.8: *A SAED pattern obtained from a crystalline silicon substrate in [100] direction (a) and the SAED pattern displays diffraction rings characteristic of a nanocrystalline AZO/ITO thin film (b).*

Four-dimensional STEM (4D-STEM)

4D-STEM is an evolution of scanning transmission electron microscopy that takes full advantage of innovations in the field of hybrid-pixel direct electron detectors to capture the electron diffraction patterns at each pixel in STEM images. With this methodology, the microscope acquires a 2D reciprocal space image (k_x,k_y) tagged to every pixel, as the transmitted electron beam is scanned across a 2D region of interest (ROI) in real space (x,y); hence, the term 4D-STEM. **Figure 3.9 (b)** presents the schematic of the 4D STEM technique.

A convergent electron beam is rastered across the sample, and at each probe position, a 2D convergent beam electron diffraction pattern is recorded using a pixelated detector. This generates a four-dimensional dataset comprising spatial (x, y) and reciprocal space (k_x,k_y) information, enabling advanced analysis such as strain mapping, phase identification, and electric field imaging.

One of the key 4D-STEM applications explored in this thesis is crystal orientation mapping. When computer image processing methods are utilised to classify crystal orientations automatically, this approach is referred to as automated crystal orientation mapping. [89]. The two main tools used to study polycrystalline material orientation mapping are electron backscatter diffraction (EBSD) in SEM and nanobeam electron diffraction

(NBED) in TEM [90]. EBSD can measure the orientation of bulk crystalline materials with a spatial resolution of typically 50 nm when using a FEG-SEM, see table 3.2.

A recently developed technique based on TEM, which utilizes electron beam precession in conjunction with spot diffraction pattern recognition, now offers the possibility of acquiring reliable orientation/phase maps with a spatial resolution of 2 nm on a FEG-TEM. The technique may be described as precession-assisted crystal orientation mapping in the TEM, also known by its product name, ASTAR, and consists of scanning the precessed electron beam in nanoprobe mode over the specimen area, thus producing a collection of precession electron diffraction (PED) spot patterns, to be thereafter indexed automatically through template matching [91, 92].

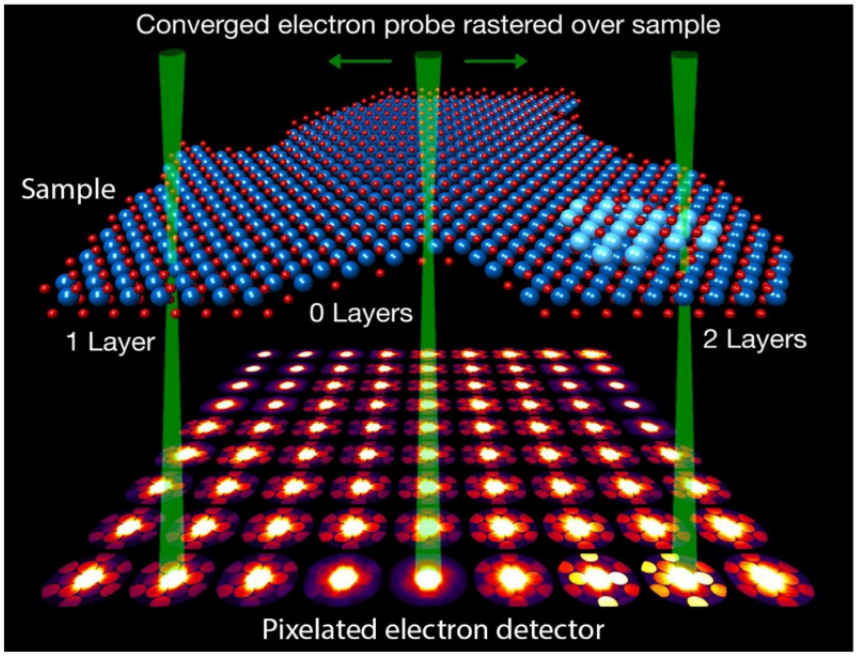

Figure 3.9: *A Schematic of four-dimentional STEM (4D-STEM), Adapted with permission from Ophus (2019) [93].*

Analytical investigation, particularly in polycrystalline materials, via 4D-STEM mapping allows the selection of orientation/phase measurements for near-real-time orientation and phase mapping of single and multiphase polycrystalline and amorphous materials [94]. In this method, an electron beam with approximately 1 nm in size was scanned across

the specimen while acquiring diffraction patterns at a high speed of hundreds of frames per second using an integrated hybrid-pixel direct electron detector. A template matching algorithm is used to index each experimental diffraction pattern by automatically matching the templates from the kinematic diffraction modeling. The diffraction templates were precomputed for each orientation of the given material, based on its crystal structure [95].

Template matching is fully automated and can generate an estimate of the measurement confidence using cross-correlation between the templates and experimental diffraction patterns. Precession electron diffraction was also applied to average out dynamical diffraction effects and increase the reliability of orientation and phase identification. A reliability map is particularly useful for identifying grain boundaries because these areas typically have low reliability [96]. **Table 3.2** highlighting key differences and similarities between EBSD, NBED, and 4D-STEM when used for orientation mapping.

Table 3.2: *highlighting key differences and similarities between EBSD, NBED, and 4D-STEM when used for orientation mapping.*

Feature	EBSD	NBED	4D-STEM
Instrument	SEM	TEM/STEM	STEM
Probe size	(10-50) nm [90]	(1-5) nm	0.1 nm [89]
Spatial resolution	(20-50) nm	(1-5) nm	1 nm
Sample requirements	Bulk (μm)	thin TEM $<$ 50nm	thin TEM$<$ 50nm
Detector	EBSD CC camera	TEM CCD/CMOS	hybrid-pixel detector
Data dimensionality	2D	2D	4D (x,y,k_x,k_y)
Crystallography accuracy	1-2 Å	$<$1Å	$<$1Å

3.4 Analytical electron microscopy technique

Analytical Electron Microscopy (AEM) employs techniques that allow for the detection of local chemical composition. The interaction between an electron beam and matter generates intricate signals.

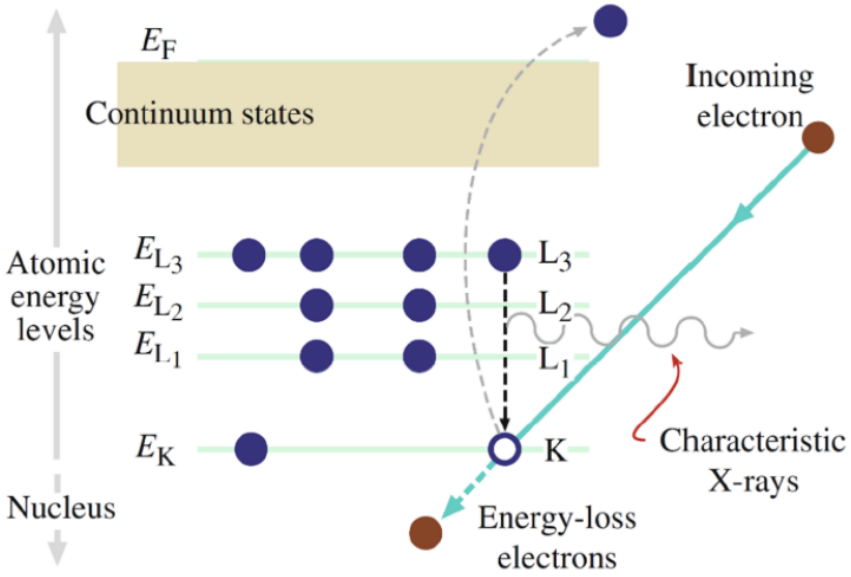

Figure 3.10: *Schematic representation of x-ray emission. Adapted with permission from Williams and Carter(2009) [61]*

3.4.1 Energy dispersive x-ray (EDX)

When the electron beam interacts inelastically with inner shells of the atoms of the material, it effectively displaces the inner-shell electrons. To occupy the resulting vacancy, an electron from a higher energy level transitions to a lower energy level, thereby releasing energy in the form of characteristic x-rays. These x-rays exhibit characteristic energies (keV) for each element, which facilitates the precise identification of the elements present within the sample. An EDX detector collects the emitted x-rays, accurately measuring their energy and intensity with a high degree of precision. It typically consists of a Si(Li) detector or a silicon-drift detector (SDD), a collimator, an electron trap to avoid contribution from electrons, and a window to isolate the detector under vacuum. The EDX detector operates when the monitored X-ray creates electron–hole pairs in the detector material. By applying a high voltage across Si(Li) crystal the two electrodes collects the electrons and holes, where the signal strength is proportional to the X-ray energy [71].

Figure 3.10 illustrates the schematic of the X-ray emission process. An electron from the K shell is ejected by an incoming electron, and the resulting vacancy in the K shell is

filled by another electron from the third subshell of the L shell. The energy difference is subsequently released as characteristic X-ray emission. X-rays can be detected using the SDD detector, which determines the energy of the incident X-ray by counting the number of electron-hole pairs generated in a thick slab of high-purity silicon.

3.4.2 Electron energy loss spectroscopy (EELS)

EELS is a widely utilized technique in TEM for analyzing the electronic structure and composition of materials at high spatial resolution. It uses the inelastic scattering from the materials; by measuring the energy loss, one can derive valuable information about the sample's physical and chemical properties [61, 70, 85] A typical EELS spectrum is composed of three primary regions: the zero-loss peak (ZLP), the low-loss region, and the core-loss region. The ZLP, located at or near 0 eV, corresponds to electrons that have traversed the sample without losing significant energy. This peak is essential for calibrating the energy scale and assessing sample thickness [70].

The low-loss region (0–50 eV) contains features such as plasmon peaks and interband transitions, which are indicative of the sample's dielectric response and collective electron behavior [60]. This region is particularly useful for studying band gaps, optical properties, and thickness variations in nanostructures [97].

In contrast, the core-loss region (>50 eV) provides element specific information, as it arises from the ionization of inner-shell electrons. Each element displays characteristic ionization edges such as K, L, or M edges, that can be used for chemical identification. Moreover, the fine structure near these edges, known as energy-loss near-edge structure (ELNES), can reveal details about bonding environments and oxidation states [98]. Advances in monochromated electron sources and spectrometer design have significantly improved the energy resolution of EELS, enabling vibrational spectroscopy in the mid-infrared regime and more precise chemical analysis at sub-nanometer scales [97].

3.5 TEM sample preparation

A very thin sample area is necessary for TEM, typically between 10 and 100 nm [69, 84], particularly for HRTEM imaging, to guarantee sufficient electron transparency and strong electron-specimen interactions. However, thick specimen leads to maximum absorption,

low penetration, and high scattering of incident electrons brings poor resolution, low contrast information [99]. This makes sample preparation a crucial part of the TEM. For thinning a sample to the point of electron transparency, this can be achieved through mechanical, chemical and/or ion beams.

When preparing samples, it is essential to exercise caution to prevent the introduction of structural or chemical artifacts, as this can lead to problems such as electrical charging of the sample, chemical smearing of interfaces, and the presence of deformation defects during subsequent microscopic studies. Proper planning and careful sample preparation can help avoid these issues. We will have some examples in Chapter 4.

Therefore, if we examine the structural and chemical variations close to the interface, we must prepare specimens in which the interface is parallel to the electron beam, which involves cross-sectioning the sample. The most widely studied cross-sectional samples are semiconductor devices, which often have multiple layers and, therefore, multiple interfaces.

In this thesis, two methods of TEM sample preparation were used to prepare thin-film solar cell samples: the **conventional technique** and **focused ion beam (FIB)**.

3.5.1 Conventional method

In the conventional TEM method [100], the steps of the conventional sample preparation method are illustrated in **Figure 3.11**. This procedure starts with the preparation of a sandwich, where the solar cell and single silicon crystal are cut into slices, which are then glued face-to-face together using epoxy and hardener glue. The number of dummy slices of a single silicon crystal used as the substrate was different; we used four slices of a single silicon crystal glued underneath and above the solar cell slices to create a sandwich structure. The second step involves cutting slices in which the stack of the sandwich structure is cut into thin slices (less than 1 mm) using a precision diamond wire saw. In the third cutting disk step, the resulting stack was punched into a standard disk with a diameter of 3 mm using an ultrasonic disc drill, which aligns with most microscope holders. Afterwards, the thinning step, in which mechanical polishing is performed using a polishing diamond paste on both sides until it reaches a thickness of approximately 100 µm. The grinding and polishing steps aim to pre-thin the bulk sample to the desired thickness for subsequent dimpling and ion milling. For this purpose, silicon carbide abrasive paper disks with grit sizes ranging from 800 to 4000 were used. Both the grinding and polishing speeds, as well as the pressure of the sample on the rotating abrasive paper disc, can be controlled

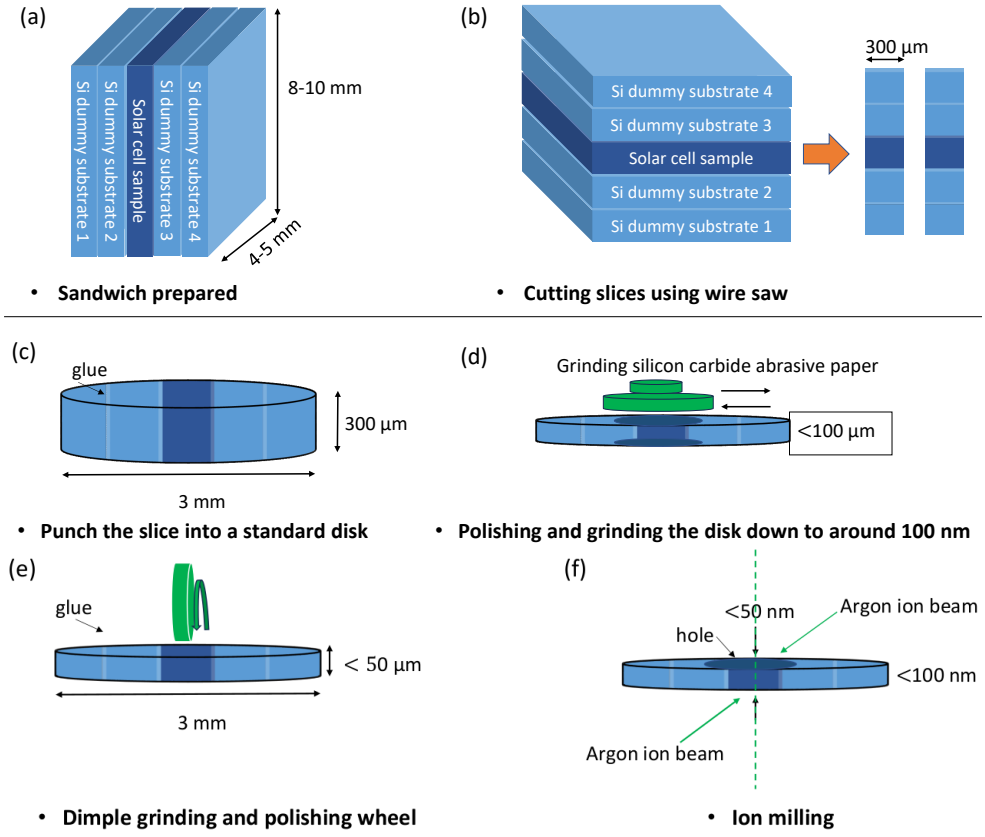

Figure 3.11: *Schematic illustration of the TEM sample mechanical preparation process for a solar cell device. (a) Preparation of the sandwich structure using Si dummy substrates with the solar cell sample placed in the center. (b) Cutting the sandwich into thin slices (∼300 µm) using a wire saw. (c) Punching the slices into 3 mm diameter standard disks. (d) Initial polishing and grinding of the disks down to ∼100 µm thickness using silicon carbide abrasive paper. (e) Dimple grinding and polishing to achieve < 50µm thickness at the center. (f) Final thinning by argon ion milling to obtain an electron-transparent region (< 50 nm) suitable for TEM analysis.*

manually. Using grinding and polishing pastes in combination with different solvents helps to optimize the surface of the sample and gently remove the material.

Subsequently, the Gatan 656 dimpling grinder enables mechanical thinning and polishing of the central area of the pre-thinned sample disk. The desired specimen thickness was achieved by grinding and polishing with the aid of different metallic and felt wheels, in combination with diamond polishing pastes of variable gradation. Appropriate selection of the grinding speed, grinding load, polishing paste, and lubricant helps minimize surface damage. The dimpling grinder introduces circular deepening in the sample, resulting in a dimpled sample of approximately 50 and less µm at the center and a greater thickness of 100 and lee µm on the outside, thus providing the mechanical strength required for easy handling.

Finally, an Ar^+ ion beam at small angles ($2 \sim 6°$) using the Gatan precision ion polishing system (PIPS) resulted in a specimen with a hole at the interface between the solar cell slices. In other words, in the side view, the specimen has the shape of a wedge with decreasing thickness toward the hole [101]. The production of a beam of Ar^+ ions that is accelerated and directed toward the center of the sample is used to lift atoms from the surface. It is used to reduce bumps and remove any strain hardening caused by a preliminary mechanical preparation. Machining with the ion beam can be performed in a longitudinal plane cut, in a cross section, or a wedge cut. The acceleration voltage of the ions can be varied between 0.1 kV and 8 kV. The accelerated ions hit the rotating specimen surface at manually adjustable angles, which allowed for the precise control of the thinning speed and uniform removal of the sample material. Low angles in combination with low accelerating voltages and low temperatures provided a gentle polishing of the electron-transparent area. The types of equipment used in the conventional preparation of TEM samples are illustrated in **Figure 3.12**.

3.5.2 Focused ion beam (FIB)

In recent years, the focused ion beam (FIB) technique has emerged as a powerful method to produce sufficiently thin lamellae from large samples. In this study, cross-sectional samples of solar cell structures were prepared using a dual-beam FIB (FEI Helios NanoLab 460F). An electron beam was employed for scanning electron microscopy (SEM), and an ion beam using a liquid Ga^+ source for focused ion beam illumination. The ion beam was accelerated at voltages ranging from 5 to 30 kV to sputter the samples at specific

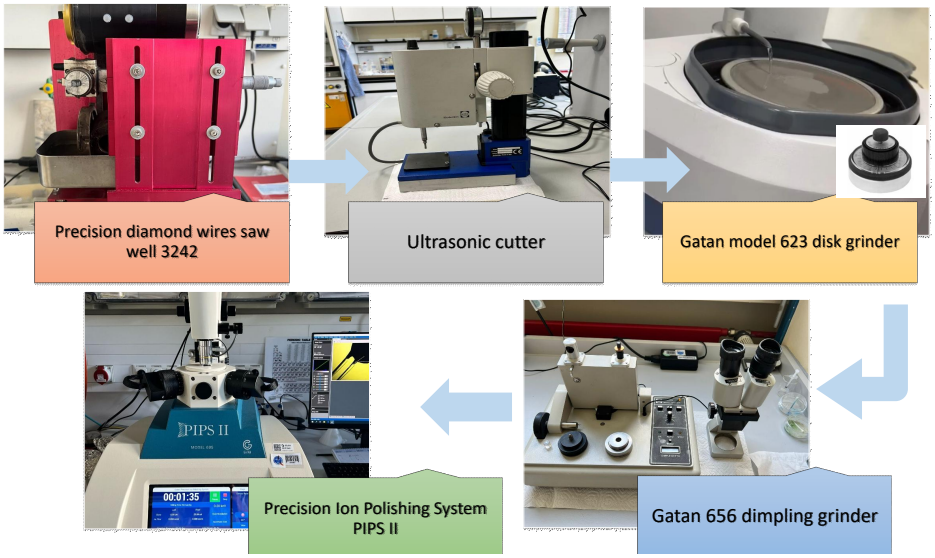

Figure 3.12: *Equipment used in the conventional TEM samples.*

positions. Adjusting the beam energy facilitated the transition from imaging to highly localized sputtering (milling). The preparation of a TEM sample enabled the selection and isolation of a specific area as an electron-transparent sample through trenching. The thin section is subsequently lifted from its host using a micromanipulator or cut in a form that permits direct inspection under a microscope. **Figure 3.13(a)** and **(b)** show the regions of interest in the solar cell sample at 400 and 30 µm, respectively.

As illustrated in **Figure 3.13 (c)**, a protective layer was deposited by injecting Pt precursor gas near the area of interest. Upon the impact of an electron or gallium beam on the sample, secondary electrons are emitted, resulting in the decomposition of the precursors and subsequent localized growth of the Pt/Ga/C mixture. Subsequently, **Figure 3.13 (d)** shows the wedge-shaped shape of the specimen obtained via focused ion beam milling. In the following step, as depicted in **Figure 3.13 (e)** 30 kV Ga ions were utilized to perform the J-cut side, which remained attached to the sample solely at the upper right portion. The FIB manipulator needle was subsequently affixed to the lamella using a Pt/Ga/C precursor.

Fixing the final connection with the sample facilitated a "lift out" of the lamella, which was then attached to the TEM grid, as illustrated in **Figure 3.13 (g)**. TEM grids

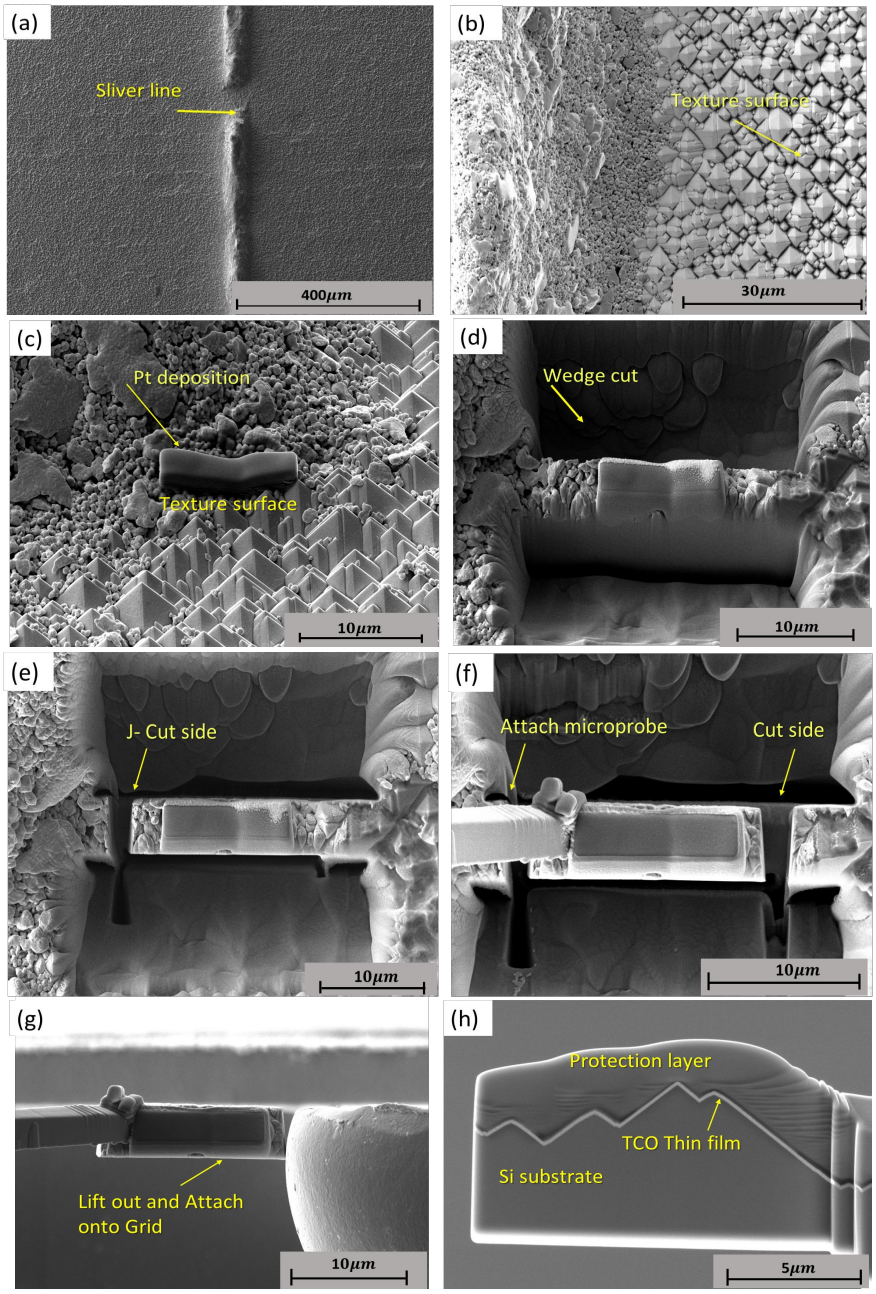

Figure 3.13: *SEM images illustrating the focused ion beam (FIB) technique steps. For detailed explanation of individual steps see text.*

can be fabricated from various materials, including Cu, Mo, Au, Be, Si, and Ni. In the final stage, the manipulator needle was detached from the lamella was further thinned using reduced Ga^+ ion voltages and currents, as shown in **Figure 3.13 (h)**. A final thinning step with Ga^+ ions was conducted at 5 kV and an angle of 5° to the lamellar surface to minimize the thickness of the amorphous surface layer formed during the thinning process [102, 103]. **Figure 3.13** depicts SEM images showing the focused ion beam (FIB) technique steps **(a,b)** show the region of interest in the solar cell sample at 400 µm and 30 µm, respectively; **(c)** deposition of the protective Pt layer on the interest region; **(d)** cutting a wedge shape from the specimen by focused ion milling, **(e)** fixing a micromainoulator, **(f)** lifting out and fixing the lamella on a half-grid; **(g)** removing the micromainpulator and tilting the lamella; and **(f)** thinning the lamella to approximately 30-50 nm for electron transparency.

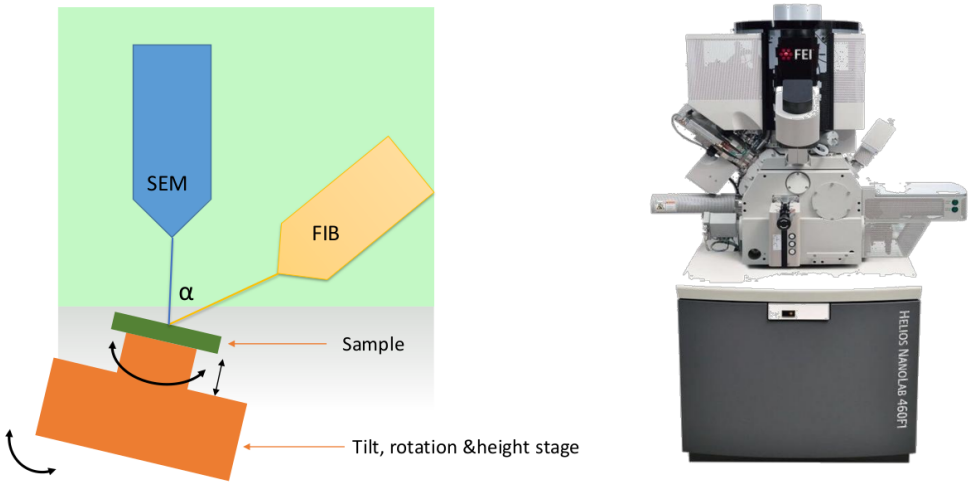

Figure 3.14: *Schematic illustration of a dual beam FIB/SEM (left). The angle (α) between the electron beam and ion beam is normally in the range of 52 and 54° the FEI nanolab 460F1 scanning electron microscope (right).*

Plasma cleaning

To obtain clear TEM and STEM images, a plasma cleaner have used for sample cleaning prior to TEM and STEM analysis. This method allows fine-probe microanalysis for an extended period without carbonaceous accumulation under electron beam irradiation

in TEM and STEM. To ensure correct cleaning and prevent contamination, we need to optimize the following parameters:

- Proper reactive gas plasmas: The efficiency of plasma cleaning significantly depends on the gas used in the process. For instance, the Fischione plasma cleaner model 1400 was used to clean FIB-prepared specimens with a mixture of 75% Ar and 25% O [104, 105].
- Furthermore, it has been demonstrated that some multi-step processes are more efficient in eliminating contamination than single-step processes. A minimum ion energy is required for effective cleaning of the TEM specimens.
- Plasma density: A higher plasma density means there are more reactive species (such as ions and radicals) available to interact with contaminants on the sample surface. This increases the efficiency and rate of the cleaning process. However, if the plasma density is too high, it can lead to unwanted damage or etching of delicate specimens, particularly those prepared by FIB.
- Electron temperature: Higher electron temperatures generally enhance the plasma's reactivity and can improve the breakdown of hydrocarbon contaminants. However, excessively high electron temperatures can increase the risk of damaging sensitive samples or altering their surface chemistry. Thus, maintaining an optimal electron temperature is essential for controlled and gentle cleaning, especially for high-resolution imaging applications like TEM and STEM.

3.6 Fabrication of solar cells

In this section, the fabrication of solar cells was introduced, including the key processes involved in converting single-crystal silicon substrates into functional photovoltaic devices. The following subsections will focus on three important components: silicon heterojunction (SHJ) solar cells, transparent conductive oxides (TCOs), and transparent passivating contacts (TPCs).

3.6.1 Silicon heterojunction solar cell

The SHJ solar cells were fabricated using flat or textured n-doped (111) c-Si wafers with a thickness of 135 µm. Afterwards, chemical processing, such as saw damage removal, was

performed. The c-Si wafers were cleaned and SiO_2 was fabricated on both sides of the wafers using ozone water at 30°C for 10 min. The c-Si wafer surface should be clean and non-oxidized to obtain good solar cell performance in terms of surface passivation. Then, texturing was performed using a wet electrochemical etching process that formed a unique texture on the wafer surface to reduce the reflectivity of the surface and trap photons. In the second stage, passivating (i) a-Si:H deposited on both sides of the c-Si wafer with a typical thickness of (3-4) nm has a crucial effect on the performance of the SHJ cells, see **Table 3.3**.

Table 3.3: *Summary of layer, thickness, and deposition techniques for the solar cell structure.*

Layer	Thickness	Grown by
a-Si:H(n)	3-4 nm	PECVD
a-Si:H(p)	3-4 nm	PECVD
c-Si	135μm	Cz
nc-SiC:H(n)	4-5 nm	HWCVD
nc-SiC:H(p)	25-30 nm	HWCVD
ITO	60-70 nm	RF-sputtering
AZO	70-100 nm	RF-sputtering

After that, a (3-4) nm of n-doped (n) a-Si:H and p-doped (p) a-Si:H were fabricated on both sides using plasma-enhanced chemical vapor deposition (PECVD). The deposition of TCO materials followed these steps. The final step, metallization, either a silver evaporation system or a screen printer, was used. The silver evaporation system was built in-house, and the screen printer was an MT-650TVC by Micro-tec Co. The evaporated silver results in 2 µm high silver fingers and busbars on the front side and a full area of the silver rear side with a thickness of 700 nm. The screen-printed fingers had a height of 30 µm and a width of 55 µm. For a 2×2 cm^2 solar cell, a busbar-less ten-finger design with a squared silver frame around the active area was used. After screen-printing, the cells were annealed for 40 min at 170°C.

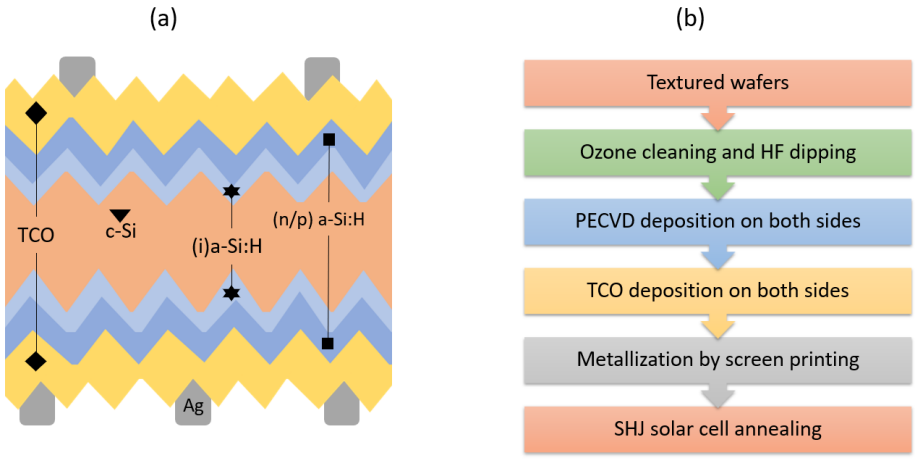

Figure 3.15: *Silicon heterojunction solar cells built on pyramidal-textured c-Si wafers (a), The main steps of the manufacturing process of the SHJ(b).*

3.6.2 Transparent conductive oxide

Due to the high resistance of thin doped a-Si:H layers, they are typically overlaid with TCO layers to facilitate the collection of current generated by light exposure. In this thesis, TCO materials AZO and ITO were deposited by magnetron sputtering with Ar^+ gas from a planar AZO target with a doping ratio (1% Al_2O_3 and 99% ZnO). AZO films were fabricated in the radio frequency mode (RF) using 1 kW power, 1×10^{-3} mbar pressure, and 100°C temperature. ITO films with a doping ratio (3 wt% SnO_2 and 97 wt% In_2O_3), ITO films were fabricated in the direct current mode at 5 kW power, 3×10^{-3} mbar pressure, and 200°C temperature. In the standard configuration for solar cells, ITO was sputtered through a mask to define four 2×2 cm^2 solar cells on each wafer.

The film thickness of TCO was approximately 70 nm to fulfil the requirements of SHJ solar cells. Typically, SHJ cells are composed of n-type c-Si wafers coated on both sides, with thin intrinsic and doped a-Si:H layers. These layers were then fully covered with TCO films, followed by screen-printing of the contact metal grids for current collection using a low-temperature Ag conductive paste. **Figure 3.15 (a,b)** A cross-sectional view of a conventional SHJ solar cell and the main steps of the manufacturing process.

3.6.3 Transparent passivating contact

For TPC solar cells, symmetric samples and solar cells were fabricated with Czochralski-grown n-type double-side textured, 170-µm-thick, 1 Ω cm silicon <100> wafers produced by LONGi. The wafers were cleaned in a cleanroom according to the standard RCA (Radio Croporation of America) cleaning. The native oxide was removed in 1% diluted hydrofluoric acid for 5 min. Subsequently, wet chemical oxide was produced in a mixture of H_2O_2 and H_2SO_4 in a ratio of 2:1 at a temperature of approximately 60°C for 10 min. This resulted in a SiO_2 thickness of approximately 1 nm. As a standard rear side for the SHJ solar cell, a stack of (i)a-Si:H and (p)a-Si:H was deposited by PECVD. The final structure of the front side TPC silicon solar cell and the back-side, and the main steps of the manufacturing process are shown in **Figure 3.16 (a,b)** respectively.

The nc-SiC:H(n) layers were deposited by hot wire chemical vapor deposition (HWCVD), partly in an in-house built system and partly in a commercial system built by MRG. As precursors, 5% monomethyl silane diluted in H_2 (MMS, 6 standard cubic centimeters per minute (sccm)), hydrogen (H_2, 94 sccm), and nitrogen (N_2, 30 sccm) were used unless stated otherwise. Three 15 cm curled rhenium wires were used as the catalysts. The deposition chamber was then heated to 250°C using a chamber heater. The deposition pressure was 0.75 mbar. The filament temperature was tuned by adjusting the electrical current flowing through the wires. For double-layer stacks, the temperature of the hot-wire filaments increased during deposition. For the symmetric samples, the first layer of nc-SiC:H(n) with a thickness of 4-5 nm was deposited at T_f= 1775°C. The filament temperature to produce the second conductive layer was varied between T_f = 1.895 and 2.055°C with layer thicknesses of 25–30 nm. The solar cells for ITO development were deposited with (n) nc-SiC:H layers deposited at T_f = 1.775°C with a thickness of 3 nm, followed by T_f= 1.950°C with a thickness of 30 nm. In the standard ITO, a thickness of 70 nm was deposited to enhance the anti-reflection effect of the TCO.

The back side consists of intrinsic and p-type hydrogenated amorphous silicon (i/p) a-Si:H and an ITO layer.

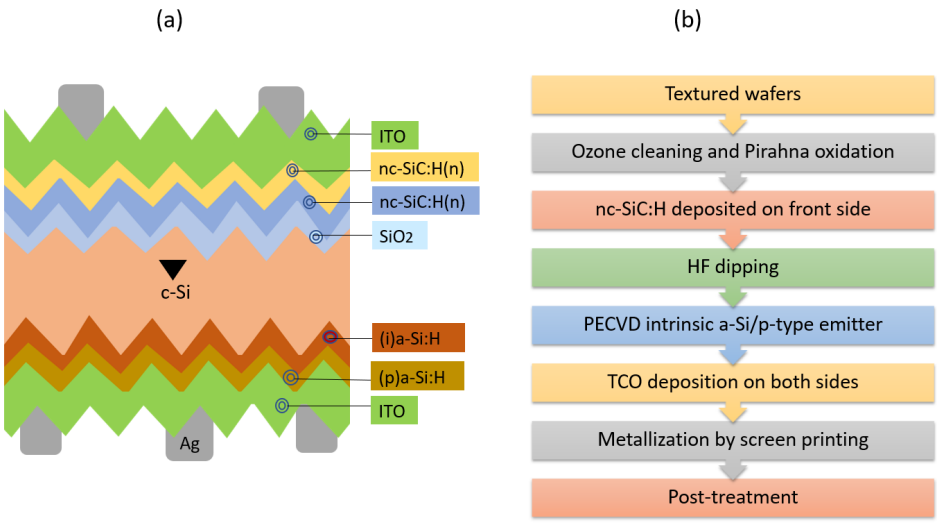

Figure 3.16: *Sketch of a silicon solar cell using an n-type wafer with a TPC on the front side (a), The main steps of the manufacturing process of the TPC (b).*

3.7 Experimental details

This section outlines the experimental procedures and characterization techniques employed during the fabrication and analysis of high-efficiency silicon based solar cells.

Structural characterization techniques

HRTEM images of the thin films on the SHJ solar cell in this thesis were obtained using a FEI Tecnai F20 TEM operated at 200 kV, but not equipped with any corrector. The Digital Micrograph software from Gatan was used for image processing. The cross-section TEM samples in this thesis were prepared using both the FIB and the ion milling methods.

Elemental composition analysis and line scans for different regions along the thin film were conducted using EDX performed on a Thermo Fisher Spectra microscope at 300 kV. The STEM-EDX line scans were recorded and evaluated using the Velox software. Detailed mapping of the orientation, phase mapping, and further grain size investigation were performed by integrated and near-real-time 4D-STEM data acquisition and analysis using a TESCAN TENSOR operated at an acceleration voltage of 100 kV. At each pixel

in the STEM dataset, TENSOR rapidly acquired a diffraction pattern with a size of 120 mrad and a precession angle of 0.8°. The template of the diffraction pattern was created using a Crystallographic Information Framework (CIF) file for each material. AZO has a hexagonal wurtzite structure belonging to the space group P63mc, with a lattice constant of a = 3.2495 Å, and c=5.2069 Å (JCPDS #36-1451). ITO is cubic bixbyite, and the symmetry of the space group is (Ia3 #206), with a lattice constant of a = 10.117 Å, and c=10.118 Å(JCPDS # 06-0416). 3C-SiC refers to nc-SiC:H layers, which are cubic, with lattice parameter a= 4.348 Å, and c= 4.348 Å.

Hall Effect Measurement

Hall effect measurements facilitated the evaluation of charge carrier density (N) and charge carrier mobility (μ) in the TCO layer. This technique positioned four contact pins at the edges of an 11x11mm^2 sized sample. A current, I, was applied to the two opposing contacts. Because the magnetic field (B) is applied perpendicular to the substrate surface, the Lorentz force affects the moving charge carriers in the TCO film with a known thickness d.

A counteracting electrical field induces a voltage V_H between the contacts perpendicular to the current-applying pins, which is proportional to the charge-carrier density N:

$$V_H = \frac{IB}{qdN}$$

The charge carrier concentration, charge carrier mobility, and resistivity (R) of the AZO and ITO films on glass substrates were measured using a Hall measurement system RH2030 from PhysTech GmbH by applying the van der Pauw method. This method has the advantage of not being affected by the sample geometry. However, to minimize measurement error, contact pins should preferably be placed at the edges of the sample. Before each measurement, the ohmic contact between the contact pins and the sample was verified. The measurements were performed at room temperature in ambient air.

J-V characterization

A double-source (xenon and halogen lamp) class A solar simulator (Wacom-WXS140s-Super) was used to conduct $J-V$ measurements. For measurements, the solar cell is

placed and fixed by aspiration on top of a copper plate, which is connected to a temperature controlling system. The contacting pins were coated with gold to achieve good electrical contact. During the measurement, the pins were raised through holes in the sample plate and the back-side contact of each solar cell with a cell area of 10 $\times$ 10 mm^2.

The solar cell conversion efficiencies (η), the fill factor (FF), open-circuit voltage (V_{oc}) and short-circuit current density (J_{sc}) are determined at standard test conditions (AM 1.5G, 100 mW/cm^2, 25°C) using a LOANA characterization system from pv-tools with a wave labs Sinus 220 light source. The ideality factor, n, and saturation current density, J_0, were obtained under dark conditions. A photodiode-type Hamamatsu S1336-BQ was used for calibration.

Quantum-efficiency and reflection measurements

For external quantum efficiency (EQE), the LOANA system from pv-tools was used. EQE measurements provide valuable insights into the absorption and charge carrier extraction of solar cells as a function of the wavelength of the incident light. For the measurement, calibrated monochromatic light was illuminated stepwise onto the solar cell. The generated current was then measured. Because of the very low currents, the measurement was performed using lock-in amplifiers. The number of photons per wavelength interval is known because of the calibration. EQE measures the collected charge carriers divided by the number of incident photons. The internal quantum efficiency (IQE) is the number of collected charge carriers divided by the number of absorbed photons. Therefore, the number of reflected photons was subtracted from the number of incident photons,

$$IQE = \frac{EQE}{1 - R}.$$

3.8 Conclusion

This chapter presented a comprehensive overview of the primary methodologies employed in this thesis, with a particular emphasis on TEM and its associated spectroscopic techniques. The fundamental principles and operational modes of TEM were introduced, establishing the foundation for the analytical approaches used in subsequent chapters. Furthermore, the chapter discussed and compared various sample preparation methods, focusing on conventional mechanical thinning and advanced focused ion beam (FIB) techniques, both of

which are critical for producing high-quality specimens suitable for high-resolution TEM analysis. Special attention was given to the preparation of solar cell samples, which require tailored procedures due to their layered structures and material sensitivities. The methodologies described here are instrumental for the structural and compositional characterization conducted throughout this research.

4 Challenges in TEM sample preparation of solar cell and solutions

"TEM is only as good as your sample."

Colin Humphreys

4.1 Limitations and practical difficulties in TEM sample preparation

The process of studying materials and their changes and finding ways to develop them begins with the mechanism of preparing samples, processing them, and preparing them for examination under a TEM, which ultimately determines the success rate of the research process. For details on the sample preparation method, refer to Chapter 3.

Preparing high-quality TEM samples is a critical process due to its impact on the investigation and examination process. Any modification introduced during preparation whether mechanical, chemical, or ion-beam induced can alter the true microstructure of the specimen and potentially lead to misinterpretation of results. This challenge is particularly pronounced in complex, multilayered devices such as SHJ solar cells, where ultrathin passivation layers and delicate interfaces must be preserved with nanometer precision. Both conventional preparation methods and FIB techniques offer distinct advantages, but they also introduce characteristic artifacts that can obscure or distort structural information. Understanding these limitations is therefore essential to evaluate TEM data critically and to adopt mitigation strategies that ensure representative microstructural imaging. Before undertaking TEM specimen preparation, several key aspects must be carefully evaluated to ensure that the prepared lamella accurately represents the intrinsic properties of the material system. As summarized in **Figure 4.1**. These include:

- Growth mechanism: Understanding the fabrication or deposition conditions under which the material was produced is essential, as these parameters directly influence the microstructure, grain size, phase distribution, and defect density. Factors such as temperature, pressure, deposition rate, gas composition, and substrate type can alter the final morphology and composition of the sample. A clear record of these parameters enables correlation between the processing conditions and the resulting structural or chemical features observed under the TEM.
- Motivation for the structure and materials: It is important to consider the scientific or engineering rationale behind the selection of the specific material or structure. This includes understanding the desired functional properties, such as mechanical strength, electrical conductivity, magnetic response, or corrosion resistance, and how these relate to the material design or synthesis route. Recognizing the motivation helps guide which regions or interfaces should be targeted during TEM analysis and ensures that the microstructural characterization aligns with the overall research objectives.
- Crystallography of the structure: A thorough understanding of the crystallographic characteristics—such as crystal orientation, lattice parameters, symmetry, and possible defects—is vital for both specimen thinning and imaging. Certain crystallographic orientations may be more prone to damage or bending during sample preparation, while others may offer clearer diffraction patterns or atomic-resolution imaging. Knowledge of the material's crystallography aids in selecting appropriate cutting directions, ion milling parameters, and imaging modes, such as bright-field, dark-field, or high-resolution TEM, ensuring an accurate interpretation of the observed features.

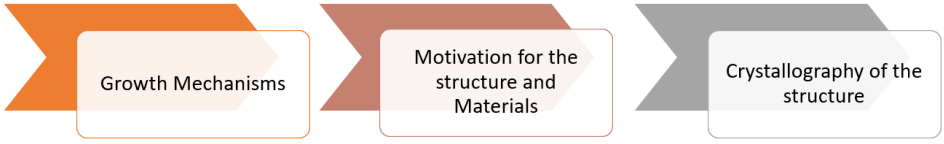

Figure 4.1: *Schematic overview of the key considerations prior to TEM specimen preparation, growth mechanisms, motivation for the structure and materials, and crystallographic orientation of the structure.*

Ideally, samples should be uniformly thin, stable under both electron beam and lab-

oratory conditions: that is, resistant to degradation or alteration in ambient air, moisture, and at room temperature. They must also be electrically conductive, non-magnetic, and sufficiently robust to withstand manipulation during transfer and analysis. In addition, the specimen should transmit enough electrons to produce a high-quality image with minimal energy loss while remaining structurally stable under prolonged electron bombardment in a high-vacuum environment. Finally, the prepared sample must conform to the geometric and dimensional requirements of the TEM specimen holder to ensure proper alignment and imaging performance [106].

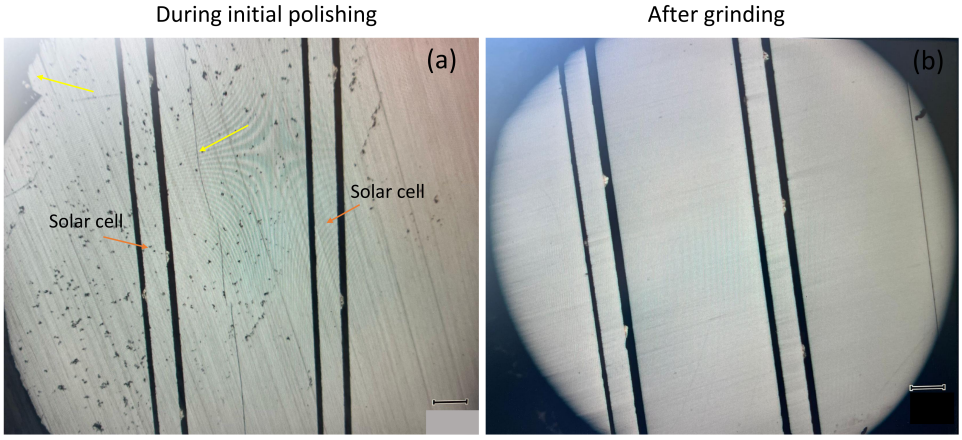

Figure 4.2: *Optical microscope images of the TEM sample at grinding stages. During initial polishing, surface roughness and scratches are visible, along with debris (indicated by yellow arrows) (a). After grinding, the surface appears smoother and more uniform, with a significant reduction in polishing defects, resulting in a sample better suited for subsequent thinning and TEM analysis (b).*

Depending on the material and application, samples can be prepared as self-supported flakes or supported by grids or thin films. In practice, it should be recognised that sample preparation may introduce defects that alter or obscure the true structure of the material. Therefore, these defects must be avoided or, if this is not possible, understood and taken into account during analysis. Finally, the duration of sample preparation can vary greatly from one sample to another, for example, from a few minutes to several days, even for the same material, which highlights the importance of technique, expertise and experience

[61]. Preparing TEM specimens typically involves techniques such as mechanical grinding, electro-polishing, and ion beam thinning. However, each of these steps can potentially introduce artifacts or damage that may affect the accuracy of the final analysis. **Figure 4.2** illustrates an optical microscope image of a solar cell sample before and after grinding, which is part of a conventional TEM sample preparation method, demonstrating small cracks (scratches) along its surface. The images show the progressive improvement in surface quality of the TEM lamella during sample preparation. In the initial polishing stage, scratches, irregularities, and debris are prominent, which can introduce artifacts in TEM imaging. After grinding, the sample surface becomes much smoother and flatter, reducing potential sources of scattering or imaging distortion [107–109].

Mechanical preparation can be performed either manually or with the aid of specialized equipment. The main advantages of this approach include its ability to produce TEM wedges and to remove surface damage completely. It also avoids the implantation of foreign material and, with sufficient experience, can be performed both quickly and reproducibly. In addition, the required equipment is relatively inexpensive, and the method reduces reliance on ion milling, thereby lowering overall preparation time and cost. However, the method also presents several disadvantages. It requires careful handling at all stages and involves a steeper learning curve than some alternative techniques. Furthermore, certain samples, particularly metals with significant internal strain, may not be well-suited to purely mechanical preparation and may require the use of alternative TEM specimen preparation methods. **Figure 4.3 (a-c)** show optical microscope images during different conventional TEM sample preparation, see 3.5. Dummy Si substrates are attached to both sides of the solar cell to provide mechanical stability. Mechanical thinning and polishing gradually reduce the thickness of the lamella, highlighting a region of excellent thinness, essential for TEM transparency, until the formation of a hole is reached, as observed in panel (c). **Figure 4.3 (d–f)** shows a TEM image at different magnifications and preparation stages. The glue line is visible in (d), while (e) shows strong bending contours due to strain and thickness variations. (f) demonstrates a hole space between the solar cell layers.

However, this conventional preparation route introduced several limitations and challenges. First, mechanical stress and bending occurred during thinning, especially near the edges of the transparent region, causing curvature in the lamella that complicated imaging alignment. Second, non-uniform thinning often produced strain and thickness variations across the area of interest, as evident from the strong bending contours observed in **Fig-**

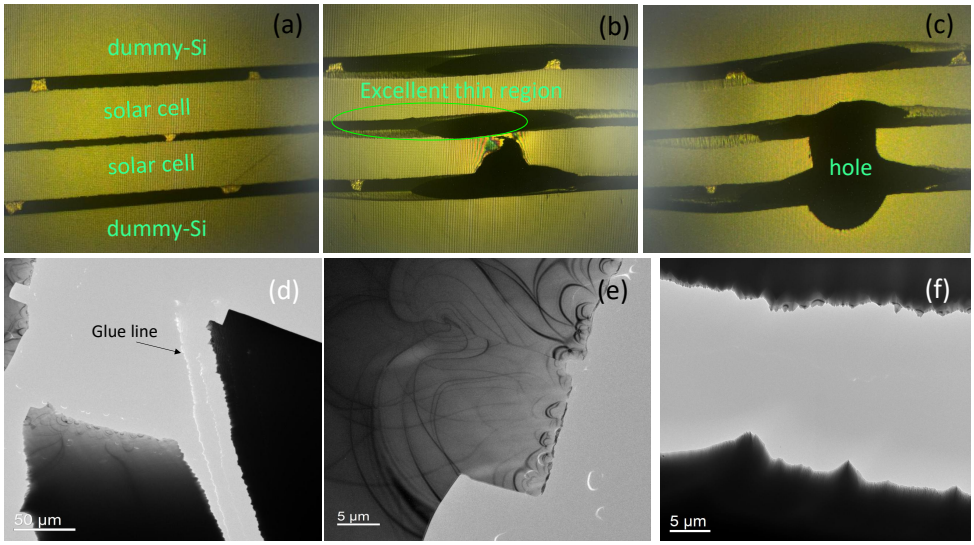

Figure 4.3: *Optical image of the glued sandwich structure, where the solar cell layers are embedded between dummy Si substrates for mechanical support (a). Formation of an excellent thin region during ion milling, suitable for electron transparency (b). Final stage showing hole formation at the center of the sample, indicating complete perforation (c). (d) Low-magnification TEM image showing the glue line and layer interfaces (d), intermediate thinning region exhibiting pronounced bending contours caused by strain and thickness variations (e), uniformly thinned area demonstrating suitable electron transparency but also revealing edge roughness from ion milling (f).*

ure 4.3 (e). Third, the glue layer between the solar cell and the supporting Si substrate (visible in **Figure 4.3 (d)**) introduced contamination and in some cases chemical residues that interfered with accurate interface analysis. Finally, over-thinning led to the formation of holes between device layers, as shown in **Figure 4.3 (f)**, making it difficult to preserve continuous cross-sectional information across the multilayer structure.

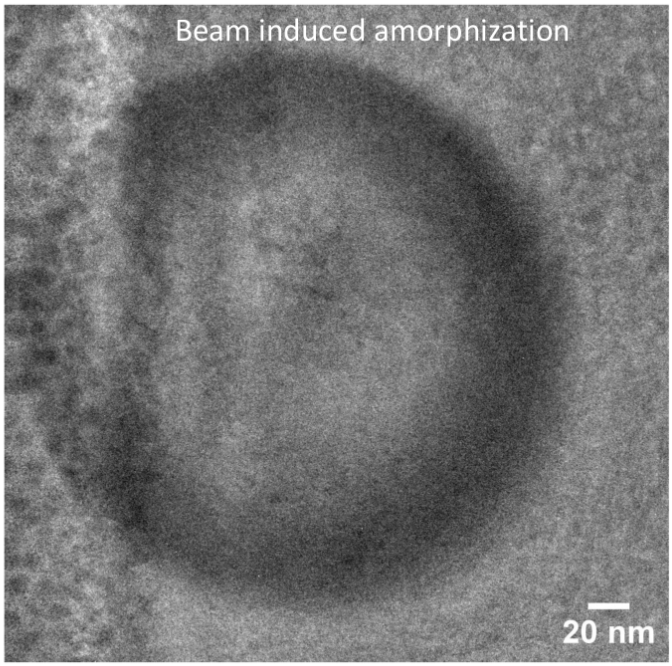

Figure 4.4: *TEM image of a FIB-prepared lamella from a SHJ solar cell, showing localized amorphous damage (dark halo) caused by ion implantation and beam-induced amorphization with scale bar 20 nm.*

On the other hand, FIB preparation involves bombarding a TEM specimen with energetic ions to sputter away material until the sample becomes sufficiently thin for TEM analysis. This is the most versatile thinning technique, applicable to a wide range of materials, and it is particularly common in semiconductor research. However, the method has significant drawbacks: it requires a very high initial investment and operating costs, and it often results in implantation of the source material as well as the formation of an amorphous surface layer that may complicate interpretation. As summarized by Liao in Practical Electron Microscopy and Database (2006) [110]. The FIB technique offers

several advantages for TEM specimen preparation. It allows for site-specific thinning and enables the extraction of multiple specimens from a small region of interest, making it also time-efficient.

Achieving uniform electron transparency across the entire sample is another significant challenge in TEM sample preparation for solar cells. This uniformity is essential for obtaining high-quality, representative images of the entire device structure. However, the diverse materials present in a solar cell often respond differently to thinning processes, potentially leading to uneven thinning rates and thicknesses across the sample. Consequently, researchers must carefully optimize ion beam energies, currents, and milling angles to achieve consistent thinning across all layers while minimizing damage to sensitive structures [111].

Figure 4.4 illustrates an example of such FIB-induced damage, where a localized amorphous region with a characteristic darkened halo indicates gallium implantation and beam-induced disorder near the SHJ interface. **Figure 4.5** presents TEM images highlighting common preparation artifacts that can arise during focused ion beam (FIB) milling. In **Figure 4.5 (a)**, the redeposition of the sputtered material is visible near the ITO layer, which can obscure fine interfacial details and affect local contrast. **Figure 4.5 (b)** shows residual material from the FIB lift-out needle embedded in the poly-Si layer, indicating incomplete removal during sample preparation. These artifacts emphasize the challenges in achieving artifact-free lamellae and the importance of careful optimization of ion milling and cleaning steps for reliable structural analysis. The high-energy Ga^+ beam used during coarse milling can induce ion implantation and amorphous surface layers, typically up to tens of nanometers thick, which may obscure fine microstructural details and alter the chemical state of the surface layers. This effect is particularly relevant for semiconducting absorbers and passivation layers in SHJ cells, where hydrogenated amorphous silicon (a-Si:H) can be modified by ion bombardment. Low-energy final polishing (2–5 kV) and protective Pt or C capping layers have been reported to reduce this damage significantly [67, 112, 113]. The better approach is using cryo-FIB to limit diffusion and beam damage, and employing low-energy Ar^+ ion polishing for final cleaning [111].

Textured and multilayer surfaces, such as silicon wafers e.g., SHJ with front and back texturing, often develop curtaining artifacts during ion milling due to non-uniform sputtering rates across rough topographies [114, 115]. Such artifacts manifest as vertical striations, complicating interface analysis. Strategies such as rocking-stage milling, variable tilt orientations, and thick e-beam Pt caps are commonly applied to suppress curtaining

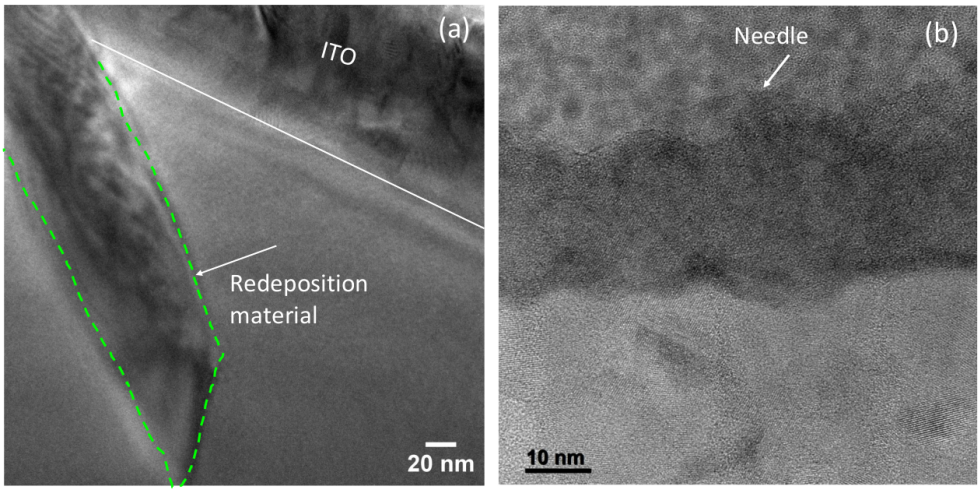

Figure 4.5: *TEM images showing preparation artifacts, redeposition near the ITO layer (a), residual needle material within the poly-Si layer. (b).*

[116, 117]. Additionally, orientation difficulty, selecting a suitable cross-sectional plane through a textured surface is non-trivial. It becomes hard to obtain a representative view of all layers across the texture. The target-specific features (e.g., pyramid tip vs. valley) are based on analysis goals.

Interface delamination and mechanical fracture: Solar cell stacks frequently incorporate weakly bonded interfaces for the TCO/a-Si:H in SHJ that may delaminate or crack during lift-out or thinning. This risk is exacerbated by mechanical stresses introduced during lamella transfer. Mitigation includes staged thinning with residual "tabs" for support, low-current finishing near sensitive interfaces, and e-beam-deposited stabilizing straps. Conventional polishing can also bend or scratch the sample, and even FIB thinning can create an amorphous surface layer if done improperly. Such damage may produce microcracks or blurred structures that obscure the true material features [118].

Achieving a consistent electron-transparent thickness of less than 100 nm on highly textured or multilayered solar cells presents a significant practical challenge.

4.2 Conclusion

This work has addressed the most important requirements and challenges in preparing a TEM sample of solar cells. Preparation of TEM samples for SHJ solar cells is particularly challenging because of the complex nature of these multilayered and textured devices. Conventional methods often lead to mechanical deformation, while FIB techniques can result in material sources implantation and amorphization. Future improvements should focus on: Advanced low-damage thinning techniques (e.g., plasma or cryo-FIB), real-time monitoring of thickness and strain using EELS or digital image correlation, machine learning-assisted optimization of preparation parameters and enhanced operator training to improve reproducibility and reduce defect introduction.

5 Microtructural evaluation of AZO-front contact on SHJ solar cell

Part of the following chapter is a published article [119]. The purpose of this paper is to investigate the microstructure of AZO films using advanced electron microscopy techniques, yielding insights beyond normal microstructural investigations, identifying their crystalline orientation, and measuring the grain size to understand how these factors influence charge carrier mobility and the electrical properties of AZO thin films with three different structures. Besides, examining the impact of incorporating an ITO seed layer beneath the AZO film, focusing on how this configuration enhances grain size, reduces resistivity, and improves electrical conductivity. Particular attention is given to the effects of grain size and boundaries on charge carrier mobility and the overall performance of SHJ solar cells.

5.1 Introduction

The common goal in solar cell technology is to increase the power conversion efficiency (η) of solar cells. Most photovoltaic research focuses on improving the performance of innovative materials and reducing manufacturing costs. To date, crystalline silicon solar cells have remained dominant in the photovoltaic market, accounting for approximately 97% of the global production of solar cells and modules [9]. So far, SHJ cells using TCO materials have achieved a record power conversion efficiency of up to 26.81%[11, 21]. TCOs are commonly utilized as electrode contacts on both sides of SHJ solar cells, owing to their appealing physical properties. The TCO provides lateral conduction for charge carrier collection and acts as anti-reflective coating [120]. For efficient solar cell performance, TCOs must possess high optical transparency and electrical conductivity [12]. For instance, ITO, Tungsten doped indium oxide (IWO) [121], titanium-doped indium oxide (ITiO) [122], indium zirconium oxide (IZrO) [123], hydrogenated indium cerium oxide (ICO:H) [124] and AZO are

among the high-performance TCO materials. These materials are polycrystalline materials consisting of small crystalline grains separated by grain boundaries, offering potential advantages in terms of stability and transparency for different photovoltaic applications.

AZO has been extensively studied for many years [125, 126] because it is a promising alternative to In_2O_3-based TCO films, which have better optoelectrical properties but are more expensive and require rare materials such as indium. Despite AZO's potential as a cost-effective and abundant material, its performance trails behind that of ITO for some reasons: on the one hand, the initial crystallinity of AZO films near the substrate is often suboptimal, resulting in high resistivity or even insulation in this region, necessitating the use of appropriate seed layers to enhance crystalline growth; on the second hand, AZO exhibits poor stability when exposed to air-borne oxygen or moisture, a problem typically addressed through high-temperature post-annealing or the application of ultrathin capping films [127]. Additionally, AZO microstructural limitations, such as grain boundary scattering and reduced charge carrier mobility, remain inadequately understood.

Charge carrier mobility and free charge carriers are crucial for the electrical conductivity of TCOs, where a high charge carrier mobility increases the conductivity without compromising transparency by free-carrier absorption [121, 128]. To reduce free-carrier absorption, it is crucial to decrease the concentration of free carriers and enhance the carrier mobility in the TCO, resulting in high optical transparency while preserving good electrical conductivity [127, 129]. Previous studies have detailed many factors that limit the mobility of thin films, which are predominantly related to the compensation of charged defects like grain boundaries and impurities such as oxygen and aluminum [121, 127, 130, 131]. The charge carrier mobility limitation, free carrier concentration, grain boundaries, and polycrystalline structural properties of TCO materials have been previously reported [12, 130–133]. In a study conducted by A. Cruz et al. [134], it was found that the electrical mobility (μ_e) of ITO deposited on hydrogenated nanocrystalline silicon (nc-Si:H) layers is significantly lower than that deposited on hydrogenated amorphous silicon (a-Si:H) films.

The nc-Si:H layers possessed greater crystallinity and higher surface roughness than the a-Si:H. The decrease in mobility in ITO/nc-Si:H is due to the decrease in the grain size of the ITO or an increase in trap density at the ITO grain boundaries. In contrast, AZO has nearly identical mobility when deposited on nc-Si:H and a-Si:H, which aligns with the similar structural properties observed through transmission electron microscopy using NBED [134]. Similar findings were observed in the present study. Specifically, we compared the performance of AZO by adding an ITO seed layer underneath it. In addi-

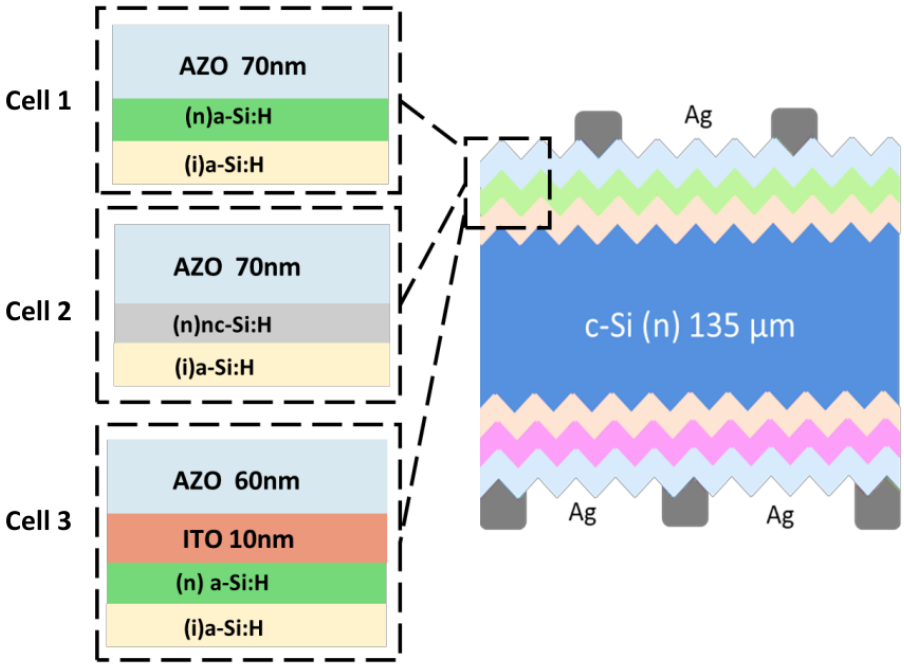

Figure 5.1: *The schematic illustration of a standard n-type c-Si substrate SHJ solar cell, the window layers of three groups of SHJ cells fabricated for this study, and the zoomed-in view of the front side of Cell 1: AZO/(n/i) a-Si:H, cell 2: AZO/(n)nc-Si: H/(i)a-Si:H and cell 3: AZO/ITO/(n/i)a-Si:H.*

tion, Tang et al. reported that adding an ultrathin layer of ITO under AZO influences the initial grains and protects the intrinsic a-Si:H layer from damage, which improves the crystallinity; the grain size increases by approximately 1.1 nm to 1.7 nm [127]. Furthermore, adding the ITO layer under AZO resulted in a higher mobility and lower resistivity compared to AZO deposited directly on doped/intrinsic amorphous hydrogenated silicon. Therefore, the polycrystalline structure of both AZO and ITO, and thereby, the presence of grains and defects in the film, may affect the charge-carrier mobility [135, 136]. Therefore, it is crucial to understand the microstructure of AZO thin films to enhance their electrical conductivity while preserving their transparency. The present study aims to investigate the microstructure of AZO films using advanced electron microscopy techniques yielding insights beyond normal microstructural investigations, identify their crystalline orientation, and measure the grain size to understand how these factors influence charge carrier mobility and the electrical properties of AZO thin films with three different structures. Besides, this research examines the impact of incorporating an ITO seed layer beneath the AZO film, focusing on how this configuration enhances grain size, reduces resistivity, and improves electrical conductivity. Particular attention is given to the effects of grain size and boundaries on charge carrier mobility and the overall performance of SHJ solar cells.

The 70 nm AZO film was grown on two types of hydrogenated silicon thin films, (n/i)a-Si:H and (n)nc-Si:H/(i)a-Si:H, as well as on an approximately 10 nm ITO seed layer. TEM is an invaluable tool for examining the nano- and sub-nanoscale functional structures of materials and has been employed for studies on thin-film devices, providing deep insights and precise information by uncovering the microscopic details and correlating them with the macroscopic properties of the material [136–138]. The innovative application of 4D-STEM with automated crystal orientation analysis was employed. The orientation and size of the grains were determined using an electron pattern-matching algorithm. Finally, this study demonstrates an in-depth structural analysis of AZO and ITO thin films in SHJ solar cells. HRTEM combined with analytical TEM methods were employed to correlate the electrical properties and performance of the SHJ solar cells [139].

A schematic illustration of the SHJ solar cells used in this thesis is shown in **Figure 5.1**. A rear-junction SHJ solar cell was fabricated on an n-type Czochralski (Cz) silicon wafer. On the front side, and for simplicity, we named the samples cell 1, consisting of (n)a-Si:H, cell 2 with (n)nc-Si:H followed by AZO and cell 3, which has (n) a-Si:H, ITO, and AZO layers. Rear-junction SHJ solar cells were produced using n-type Czochralski silicon wafers $< 100 >$ from LONGi with a thickness of 135 µm and a resistivity of 1

Ohmcm.

5.2 Electrical Performance of SHJ solar cells with AZO and AZO/ITO layers

Figure 5.2(a,b,c and d) shows the J-V measurements of the SHJ solar cells with different front contacts. When (n)nc-Si:H was used, the V_{oc} of the SHJ solar cells was higher than that when (i)a-Si:H was used, as shown in **Figure 5.2(a)**. However, **Figure 5.2(b)** shows that the average J_{sc} of the cells with AZO/a-Si:H and AZO/nc-Si:H are similar, whereas the AZO/ITO contact has a 0.2-0.4 mA/cm^2 higher J_{sc}.

Figure 5.2(c) shows the FFs of solar cells with AZO-only layers, which are comparable regardless of whether they are grown on a-Si:H or nc-Si:H. A difference was observed when 10 nm ITO was inserted between the AZO and n-type a-Si:H. A higher FF in AZO/ITO films was also reported by Tang et al., showing that the AZO/ITO stack has better contact with the a-Si:H layer and significantly improves the V_{oc} significantly to 732.7 mV compared with AZO only [127]. Overall, the η of AZO/ITO stacks was the highest among the cell types, reaching 23.6%, as seen in **Figure 5.2(d)**.

Figure 5.3 (a and b) show the electrical properties of the AZO films. Specifically, the resistivity and carrier concentration measurements indicate that cell 1, which uses AZO only, has a resistivity of 2.01×10^{-3} Ohm cm. Cell 2 also has a slightly higher resistivity of 2.20×10^{-3} Ohm cm and in cell 3, the combination of AZO and ITO provided a lower resistivity of around 1.43×10^{-3} Ohm cm, this is attributed to the superior charge carrier mobility in cell 3 and can translate into a reduced series resistance, leading to a higher FF and improved power conversion efficiency, as shown in **Figure 5.2(c and d)**. Ultimately, in cell 1, AZO-only films typically reveal a good charge carrier concentration in the range of $1.86 \times 10^{20} cm^{-3}$, whereas cell 2 reveals a higher charge carrier concentration of $2.40 \times 10^{20} cm^{-3}$. However, cell 3 with AZO/ITO has a charge carrier concentration of $2.16 \times 10^{20} cm^{-3}$. Despite cell 2 having the highest charge carrier concentration among all the cells, it had a lower charge carrier mobility, as shown in **Figure 5.3(b)**.

Nevertheless, the improvement in the charge carrier mobility of the AZO/ITO layer (up to 20.3 cm^2/Vs) might be a result of the larger grain size of 34 nm, allowing more efficient charge carrier transport compared to moving through the AZO/ITO layer more easily, reducing recombination losses, and resulting in more efficient solar cells with a higher

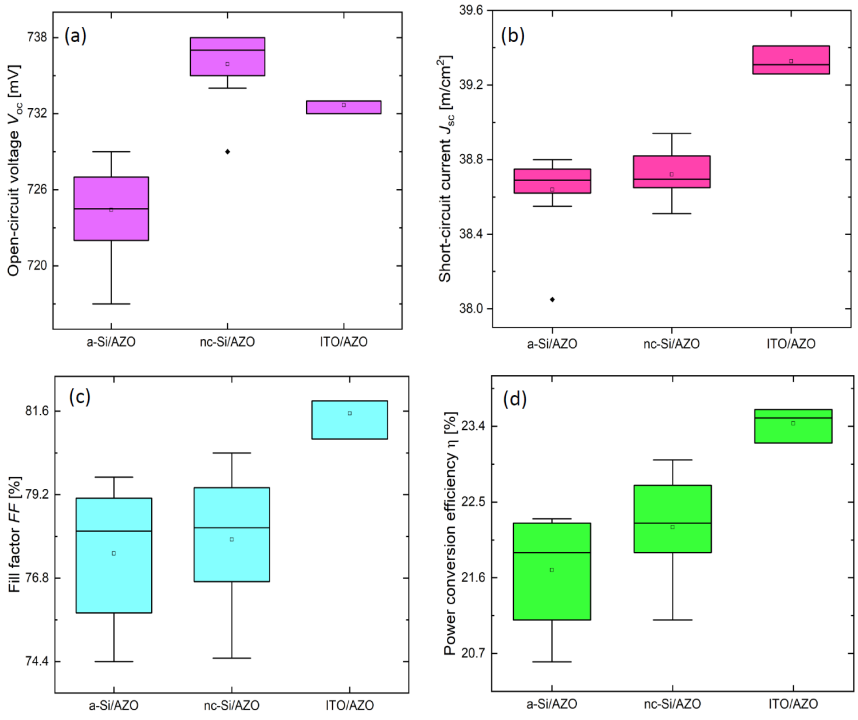

Figure 5.2: *The open-circuit voltage (V_{oc}) (a), short-circuit current density (J_{sc}) (b), fill factor (FF) (c), power conversion efficiency (η) of the solar cells with AZO front contacts (d).*

FF and improved overall electrical performance, as shown in **Figure 5.2**.

On the other hand, the charge carrier mobilities are 16.7 cm^2/Vs and 14.1 cm^2/Vs, and the grain sizes of 31 nm and 26 nm for cells 1 and 2, respectively, as shown in **Figure 5.3(b)**. The lower charge carrier mobility might be due to smaller grain sizes compared with the cell 3 AZO/ITO double-layer; for example, in the case of cell 2, the small and undefined grains, especially close to the interface of the nc-Si:H, lead to increased grain boundary scattering and subsequently increase the resistivity, as will be discussed later.

In general, the increase in charge carrier mobility is ascribed to the larger grain size, which reduces grain boundary scattering, allows for better carrier transport, and lowers the resistivity of the film. Meanwhile, from the electrical properties, cell 3 exhibited a higher charge carrier mobility and a larger FF than the AZO-only structure in cells 1 and 2 regardless of the charge carrier concentration, which means that the charge carrier concentration may not affect it as much as the charge carrier mobility [133, 140]. However, Zhang et al. examined the impact of low sputtering pressure on the structural, electrical, and optical characteristics of AZO thin films. The study was conducted on the effects of reduced working pressure on AZO thin films at ambient temperature using RF magnetron sputtering, regardless of the Ar flow rate. As the working pressure varied from 0.02-0.32 Pa, changes in morphological properties were observed. The lowest resistivity achieved is 6.40×10^{-4} Ohm cm, with charge carrier mobility playing a more significant role than carrier concentration in this outcome [133].

A comprehensive review of the literature, as presented in **Table 5.1**, highlights the performance of AZO-related SHJ solar cells. Our AZO-based SHJ solar cell stands out with remarkable efficiency.

In order to link the electrical and optical properties with the grain size and orientation detailed descriptions of the following literatures, Park et al. showed that the grain size was calculated in the range of 46 nm. The lowest electrical resistivity was 4.65×10^{-4} to 2.98×10^{-4} Ohmcm and the average transmittance was 79 to 82% [141]. Zhang et al. estimated the grain size of AZO deposited by magnetron sputtering to be in the range of 36.3 nm. The grain sizes of the different samples were calculated from the corresponding full width at half maximum (FWHM) of the (0002) diffraction reflection based on the Scherrer formula, with an electrical resistivity of 6.4×10^{-4} Ohmcm and the average transmittance of 74% [133]. In addition, the grain size ranged from 30 nm to 39 nm. Misra et al. reported the electrical resistivity was 1.90×10^{-2} to 8×10^{-4} Ohmcm and the average transmittance

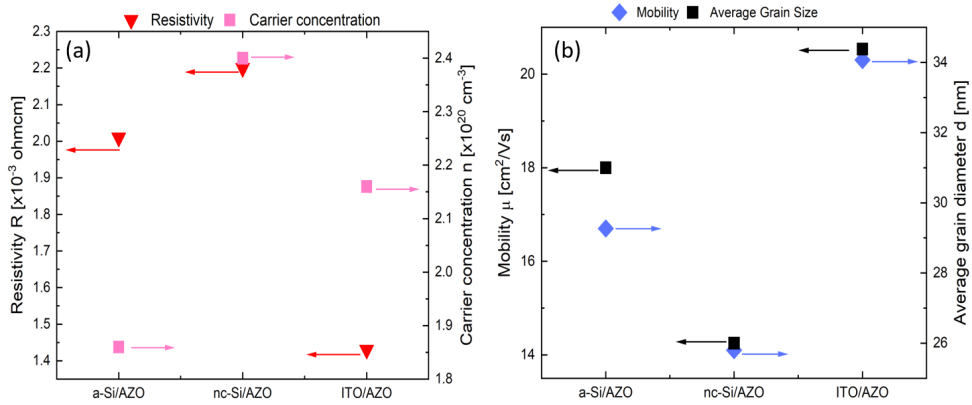

Figure 5.3: *(a) Resistivity and carrier concentration for the three cells in this study, and (b) Charge carrier mobility and average grain diameter.*

was above 87% [142]. Interestingly, all these studies showed a considerable influence of grain size on the electrical properties of AZO films, one can find further information on the optical properties of the SHJ solar cells with AZO thin layers reported in Ref [143–145]. AZO and ITO as front layers in SHJ solar cells require high transparency across the UV-Vis-NIR wavelengths. In our laboratory, it have been successfully developed AZO and ITO films with transparency exceeding 80%, making them well-suited for our applications. Regarding the AZO/ITO bilayer, it has been ensured that our films maintain sufficient transmittance and low absorptance, which are crucial for allowing light to reach the absorber layer in SHJ solar cells. Additionally, carefully control the thickness of the bilayer AZO/ITO to function as an effective anti-reflection coating, thereby enhancing the generation of photogenerated carriers. Furthermore, the improved crystallinity of the bilayer ITO/AZO film enhances charge carrier mobility, leading to lower film resistivity and better electrical performance.

Table 5.1: *Summary of the performance of AZO-related SHJ solar cells, adapted by [127].*

AZO Percentage (%)	V_{oc} (mV)	J_{sc} (mA/cm^2)	FF (%)	η(%)	Ref.(Year)
100	708	34.35	79.1	19.2	[125] (2015)
100	718	37.0	76.1	20.2	[144] (2018)
100	730	39.6	78.9	22.8	[146] (2018)
50	/	/	/	22.6	[147] (2019)
100	/	/	/	22.5	[147] (2019)
/	726	40.81	80.87	23.96	[148] (2019)
50	741	39.0	81.6	23.6	[149] (2021)
85.6	738	38.62	83.4	23.8	[127] (2023)

For this study, the observed changes in crystallographic structure between AZO-only and ITO/AZO films further emphasize the role of the ITO seed layer in enhancing grain growth and thus reducing resistive losses in SHJ solar cells, as shown in the next section.

5.3 TEM investigation of TCO thin film

TEM cross-sectional images were taken for sample structures featuring AZO deposited on different substrates, and the TEM images were taken along the low zone axis for the c-Si substrate, including **Figure 5.4 (a)** AZO on (n/i)a-Si:H, **Figure 5.4 (b)** AZO on (n)nc-Si:H/(i)a-Si:H, and **Figure 5.4 (c)** AZO on a seed layer ITO/(n/i)a-Si:H. The images confirmed that the AZO film featured a polycrystalline structure with varying grain sizes that grew at different rates. The interfaces between (i)a-Si:H/c-Si are marked with a dashed black line.

Figure 5.5 (a and b) presents BF and dark-field TEM images of the sample AZO/(n)nc-Si:H/(i)a-Si:H/c-Si, respectively. The strong diffraction contrast emphasises the columnar grain structure of the AZO film. This columnar morphology is typical of AZO thin films and appears in all three sample structures, playing a key role in determining their electrical conductivity and transparency, which are crucial for device applications such as transparent electrodes in solar cells.

The following figures present the HRTEM images for cell 1 and cell 2 and the cor-

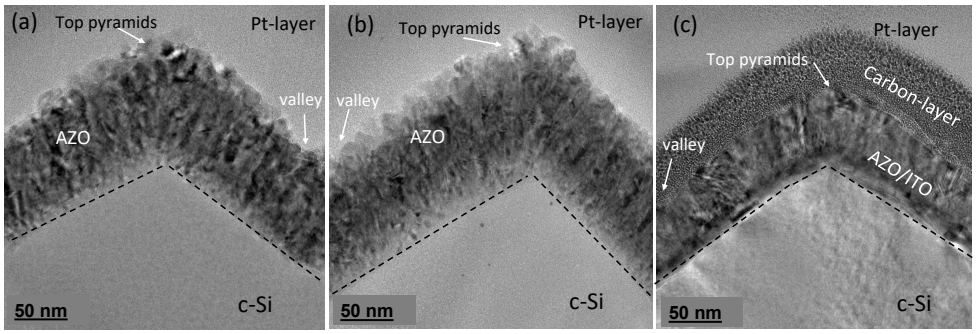

Figure 5.4: *Cross-section TEM images obtained from the sample cell 1 with AZO/(n/i)a-Si:H in (a), cell 2 with AZO/(n)nc-Si:H in (b) and cell 3 with AZO/ITO. All with scale bar 50nm*

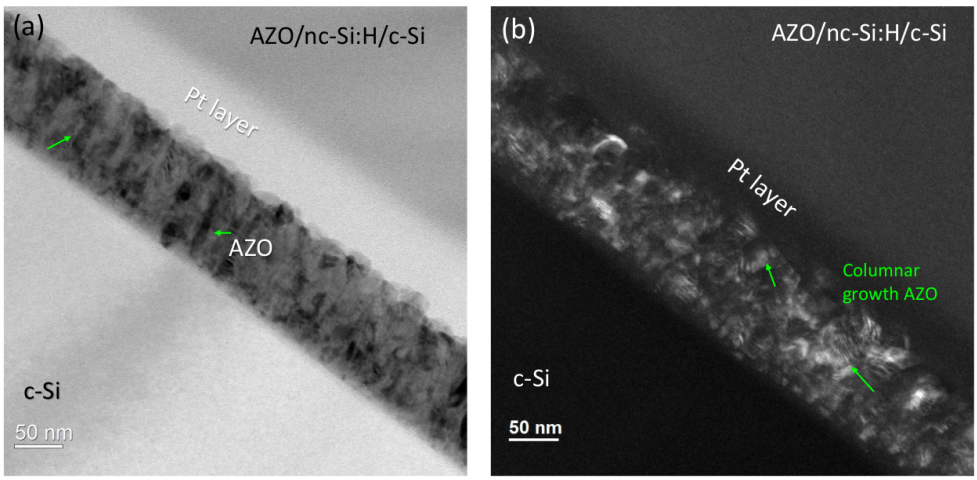

Figure 5.5: *Bright field (BF) image of the side of sample cell2 AZO/(n)nc-Si:H in (a). DF image of the same sample in (b).*

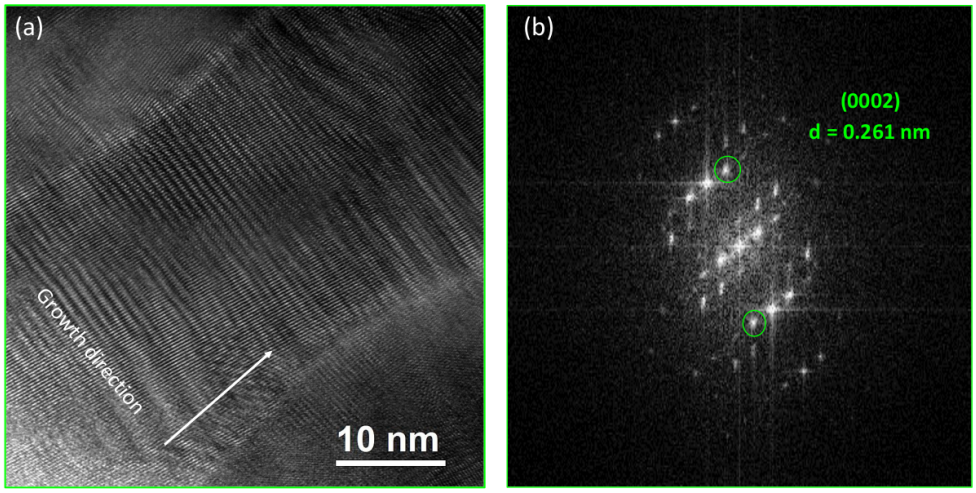

Figure 5.6: *HRTEM image of sample with AZO deposited on (i/n)a-Si:H/c-Si a scale bar of 10 nm has an average grain size of 53.8 nm (b), and the corresponding FFT pattern (b).*

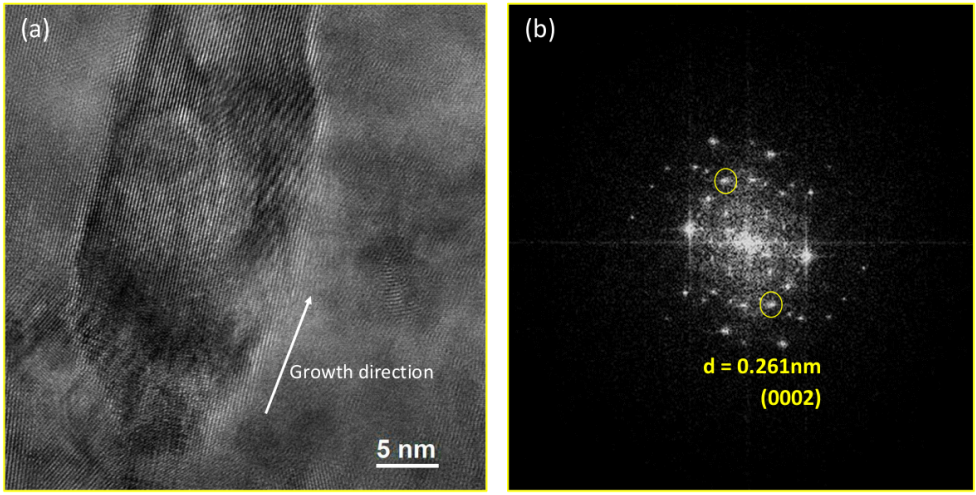

Figure 5.7: *HRTEM image of sample with AZO deposited on (i/n)a-Si:H/c-Si with a scale bar of 5 nm and its average grain size of 26.2 nm (a), and the corresponding FFT pattern (b).*

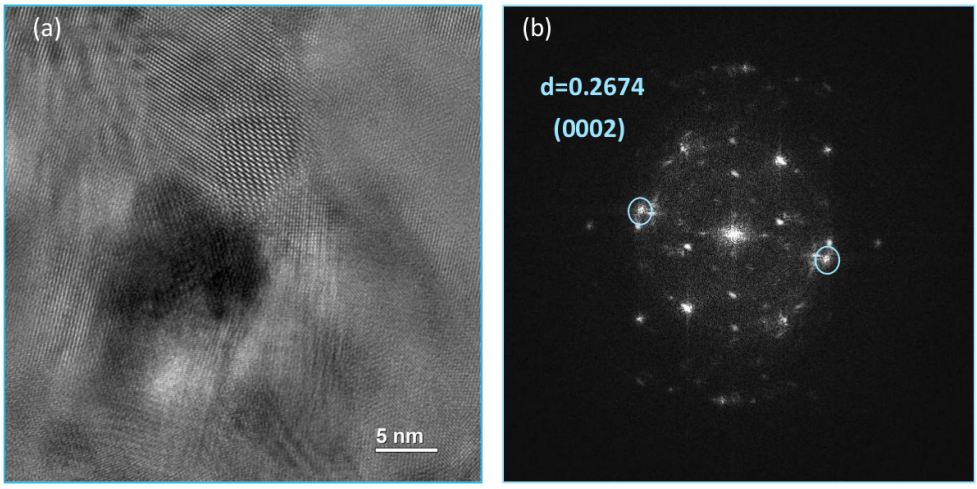

Figure 5.8: *HRTEM images of the structure with AZO deposited on (n)nc-Si:H/(i)a-Si:H/c-Si, with scale bars of 25 nm average grain size of 14.8 nm (a), and the corresponding FFT pattern(b).*

responding Fast Fourier transform (FFT), providing detailed structural insights into the typical columnar grains of AZO thin films deposited by RF sputtering on the a-Si:H film. **Figure 5.6(a,b)** shows HRTEM images of one grain of the AZO film with a size of 53.8 nm. **Figure 5.7(a,b)** shows a different grain of the same layer with a size of 26.2 nm. A similar experiment was conducted in cell 2, composed of AZO on nc-Si:H, resulting in even smaller grain sizes present in **Figure 5.8(a,b)**, the HRTEM images of one grain of the AZO film with a size of 14.8 nm.

The FFT diffraction pattern exhibited a strong intensity corresponding to an interplanar spacing of d = 0.2610 nm for the (0002) plane of the AZO hexagonal phase. The preferential growth along the c-axis, perpendicular to the silicon substrate, as indicated by the arrow in the growth direction is a characteristic feature of highly oriented ZnO-based thin films. This vertical grain alignment can reduce grain boundary density along the conduction path, minimizing carrier scattering and charge trapping at defect sites, which can significantly impact electron transport and reduce series resistance in solar cells. The combination of HRTEM imaging and FFT analysis confirmed the crystalline nature of the AZO grains. The strong alignment along the (0002) plane supports the idea that the deposition process creates a film with a well-defined crystalline structure, which generally improves the conductivity of the AZO thin film [133], electron mobility, resistivity, and

overall performance of the AZO layer. Further observations of the columnar microstructures of ZnO-based thin films have been reported in Refs [136, 146].

5.4 Microstructural and elemental characterization

This section presents a comparative structural and compositional analysis of the thin-film stacks from the three investigated solar cell samples (cells 1–3), using STEM imaging of HAADF, elemental mapping EDX and the XRD.

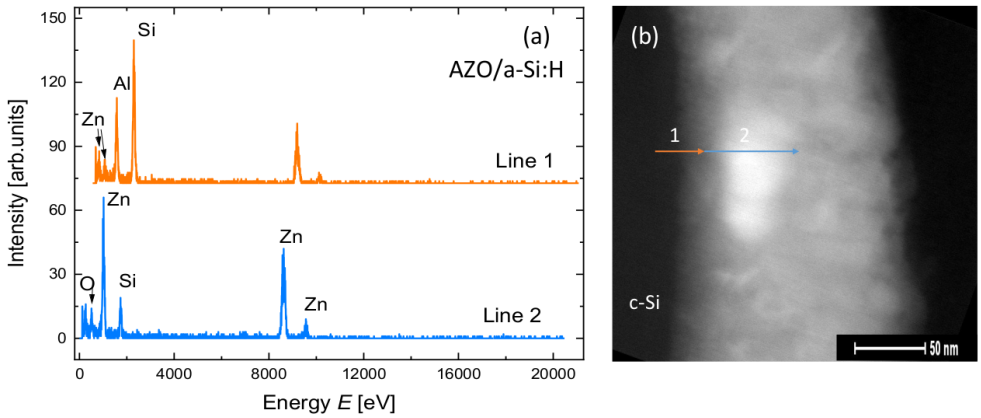

Figure 5.9: *EDX analysis was performed at the same position (a). HAADF-STEM image obtained at a comparable position within cell 1 (b).*

Figure 5.9 (a and b) show the EDX elemental maps and the HAADF-STEM of the sample with the thin film in cell 1 consisting of the AZO/a-Si:H. Lines 1 and 2 indicate the direction of analysis of the compositional map.

Figure 5.10 (a and b) show the EDX elemental maps and the HAADF-STEM of the sample with the thin film in cell 2 consisting of the AZO/a-Si:H. Lines 1 and 2 indicate the direction of analysis of the compositional map.

Figure 5.11 (a and b) HAADF-STEM overview image of the sample cell 3 showing the full multilayer stack, including AZO/ITO, a-Si:H, and c-Si. A specific region of interest highlighted in the image is zoomed in to provide a detailed view of the AZO/ITO interface. **Figure 5.12 (a and b)** show the HAADF-STEM and EDX elemental maps of the sample with the thin film in cell 3 consisting of the ITO/AZO double-layer. The arrow indicates

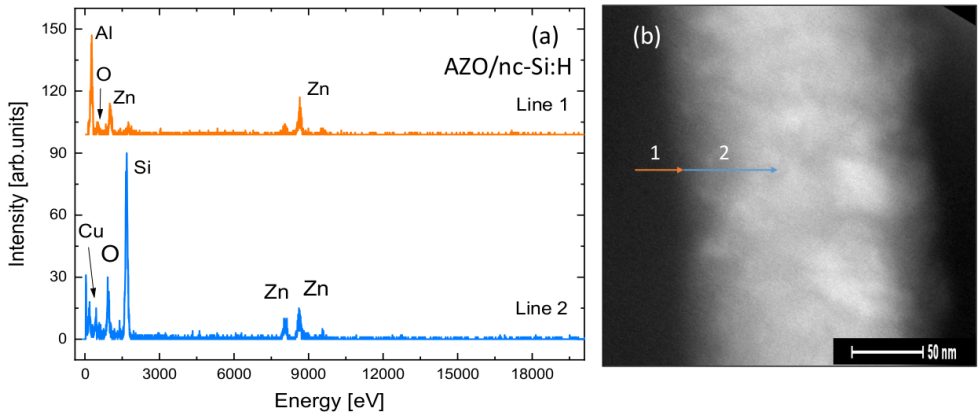

Figure 5.10: *EDX analysis was performed at the same position (a). HAADF-STEM image obtained at a comparable position within cell 2 (b).*

the direction of elemental distribution analysis corresponding to panel (b). The EDX spectra are shown in **Figure 5.12 (c)**.

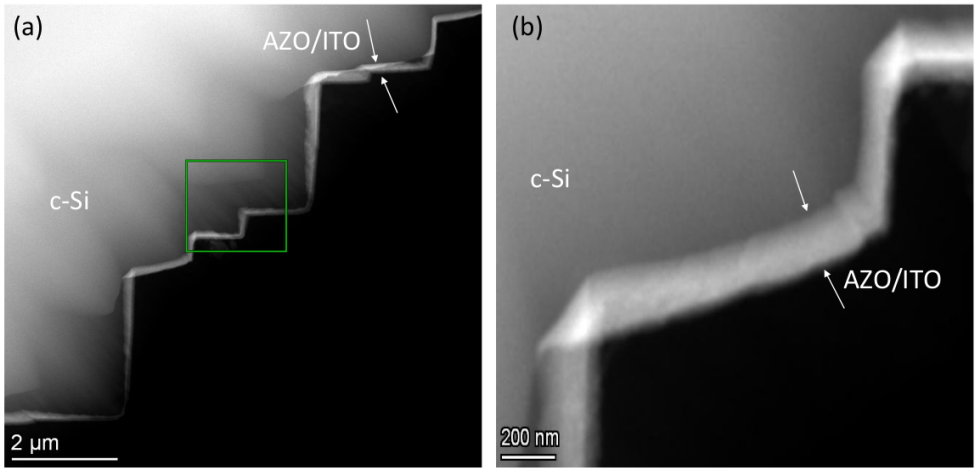

Figure 5.11: *HAADF STEM overview image obtained within cell 3 with scale bar 2µm (a) HAAD-STEM image at the different scale bar 200 nm (b).*

Indium (In) is the brightest line in the HAADF-STEM image owing to its large atomic number based on Z-contrast imaging. Therefore, the darker contrast indicates a light element and the bright contrast indicates a heavier element at that location [150],

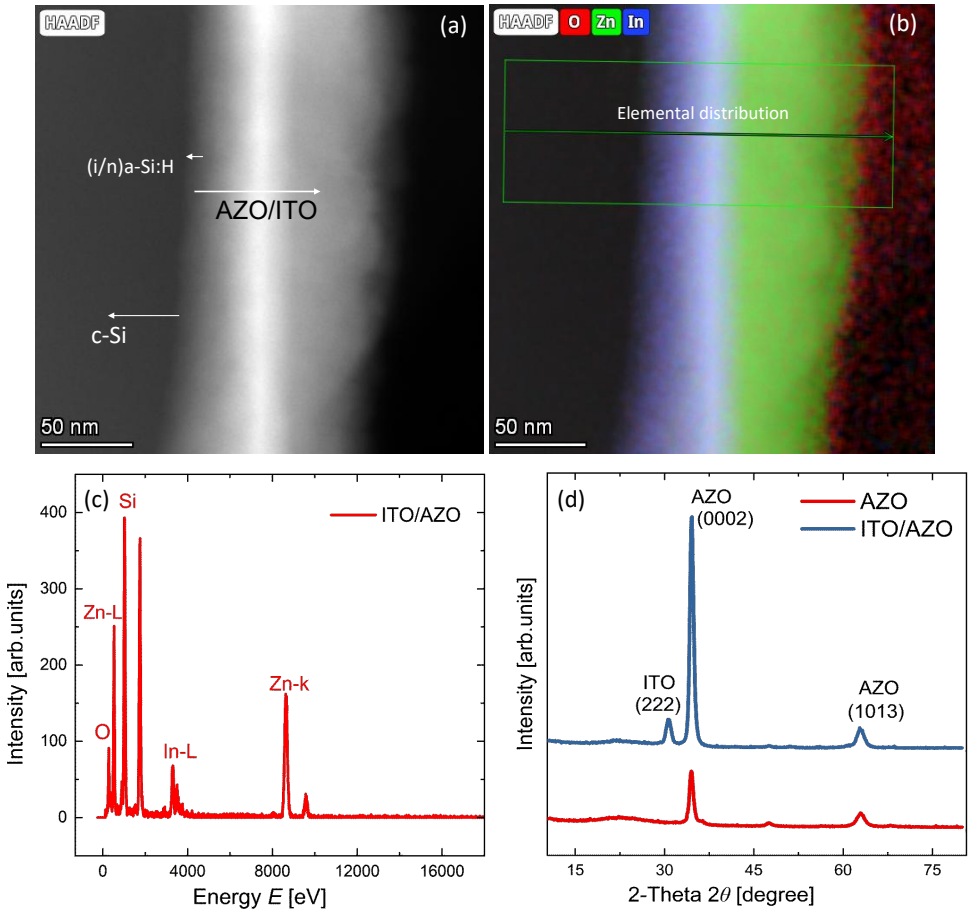

Figure 5.12: *HAADF-STEM image obtained at a comparable position within cell 3 (a), The composite image of elemental mapping (indicated with the arrow the same as growth direction) (b), EDX analysis was performed at the same position (c), XRD pattern of the TCO film, where red indicates cell 3 and black indicates cell 1 (d), adapted from [127].*

which offers an understanding of the elemental distribution within the AZO/ITO double-layer. The microstructure and morphology of ZnO-based materials were studied using XRD characterization as described in Refs [132, 135, 151–153]. For cell 1 with the AZO-only film, x-ray diffraction showed stronger reflections for the (0002) and (1013) planes, indicative of the polycrystalline wurtzite hexagonal structure. In contrast, cell 3 with the ITO/AZO film exhibited (222), (0002), and (1013) reflections. In the XRD pattern, the (0002) and (1013) reflections emerge from the AZO film and the cubic (222) reflection from ITO appears, indicating that the ITO crystallites were preferentially arranged with the (222) planes parallel to the substrate surface, which can contribute to improved electrical conductivity and charge carrier mobility [127].

5.5 Orientation mapping and influence of grain size and boundaries

Analytical investigation via 4D-STEM mapping allows the selection of orientation/phase measurements for near-real-time orientation and phase mapping of single- and multiphase polycrystalline and amorphous materials. In this method, an electron beam with approximately 1 nm in size was scanned across the specimen while acquiring diffraction patterns at a high speed of hundreds of frames per second using an integrated hybrid-pixel direct electron detector. A template-matching algorithm is used to index each experimental diffraction pattern by automatically matching the templates from the kinematic diffraction modelling. The diffraction templates were precomputed for each orientation of the given material, based on its crystal structure [95]. Template matching is fully automated and can generate an estimate of the measurement confidence using cross-correlation between the templates and experimental diffraction patterns. Precession electron diffraction was also applied to average out dynamical diffraction effects and increase the reliability of orientation and phase identification. A reliability map is particularly useful for identifying grain boundaries because these areas typically have low reliability [96].

The BF-STEM images were recorded along the [100] direction of the silicon substrate; the scanning area for each image was $2\mu m \times 2\mu m$, providing a resolution of approximately 2 nm per spot size. **Figure 5.13 (a,b)** show the virtual BF-STEM images and the diffraction patterns for the silicon substrate and the phase reliability maps, respectively. The formation of sharp edges of the textured film was observed in all three samples, indicating

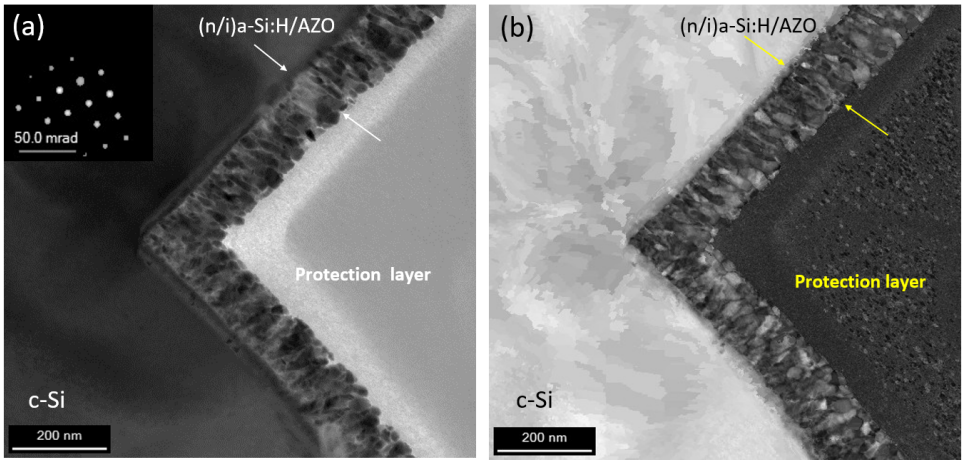

Figure 5.13: *(a) Virtual BF-STEM and diffraction patterns of the silicon substrate in the inlets for sample cell 1, AZO only, and the phase map image in (b).*

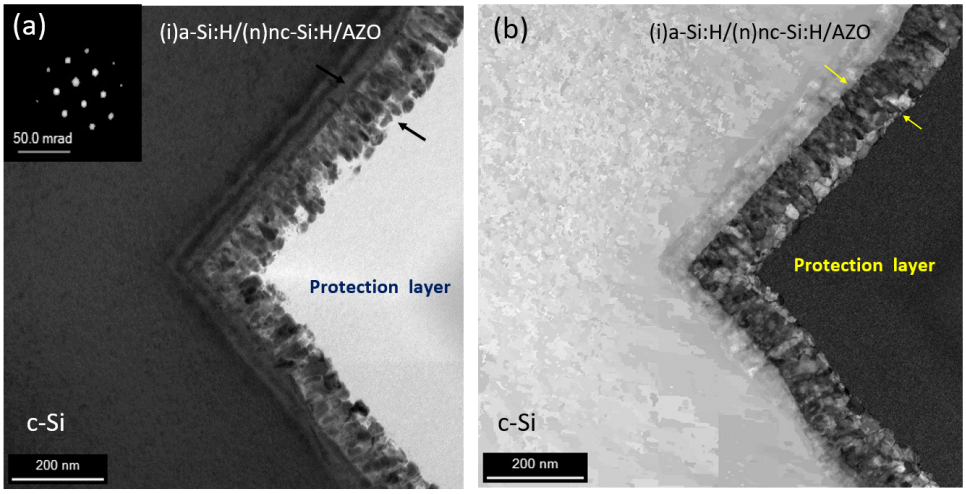

Figure 5.14: *(a) Virtual BF-STEM and diffraction patterns of the silicon substrate in the inlets for sample cell 2, and the phase map image in (b).*

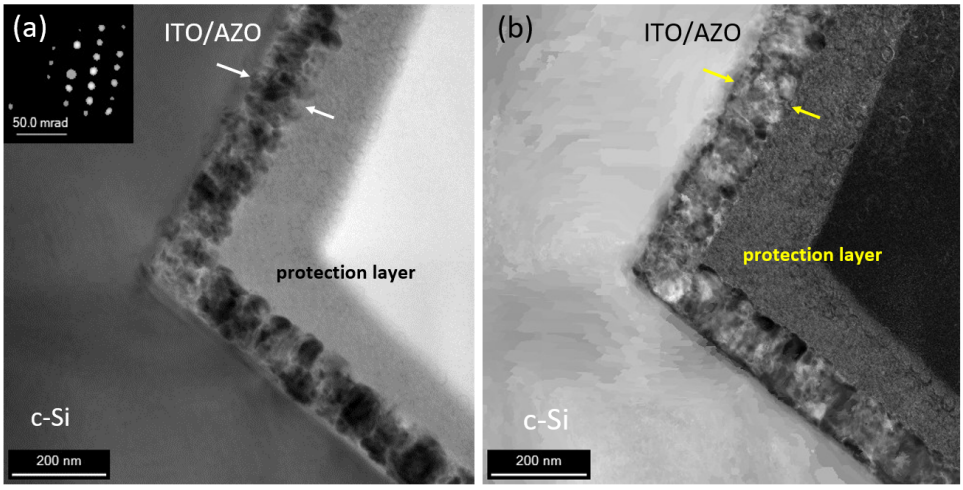

Figure 5.15: *(a) Virtual BF-STEM and diffraction patterns of the silicon substrate in the inlets for sample cell 3, and the phase map image in (b).*

a good growth quality and characterization tool resolution. The predominantly perpendicular grain orientation is relative to the silicon substrate, forming a columnar structure. This columnar growth is typical for RF sputtered AZO films and is associated with improved carrier transport due to reduced grain boundary scattering [132]. However, the grain size remains relatively moderate, which can still lead to some resistive losses in the AZO layer, especially close to the interface with the silicon substrate. **Figure 5.14(a,b)** displays the virtual BF-STEM images and the diffraction patterns for the silicon substrate and the phase reliability maps for the AZO film deposited on the nc-Si:H in cell 2, respectively.

It still has perpendicular growth concerning the substrate, similar to cell 1; however, it has been noticed that there are a small grains close to the substrate. These smaller grains can introduce a higher grain boundary density, increasing charge carrier scattering and limiting charge carrier mobility. This observation suggests that the underlying nc-Si:H layer may influence the nucleation process, leading to a finer grain structure near the interface. **Figure 5.15(a,b)** shows virtual BF-STEM images and the diffraction patterns for the silicon substrate and the phase reliability maps for the AZO with the ITO seed layer in cell 3, the grains are larger than those of cells 1 and 2. The presence of the ITO seed layer appears to promote enhanced grain growth and improved crystallinity, resulting in reduced grain boundary density and higher charge carrier mobility. The larger grain

structure in cell 3 correlates well with the improved electrical conductivity and reduced resistivity observed in previous measurements.

The orientation map along the (x,y and z) direction, where the electron beam of the microscope is along the z-direction of the grains, in which the grains in the AZO films for all cells tend to overlap and expand along the film thickness in the textured samples, resulting in depth-related uncertainties in the orientation maps. The texturing effect is particularly relevant for understanding charge transport behavior, as grains overlap and alignment along the growth direction can influence charge carrier mobility and resistivity. **Figure 5.16** shows the orientation map for cell 1, where AZO deposited on the a-Si:H layer shows somewhat large and laterally extended grains along the silicon substrate, and the images also show the existence of different crystalline phases. **Figure 5.17** for AZO deposited on nc-Si:H in cell 2 shows undefined and disordered small grains in the middle of the film, gradually forming randomly on the film surface. This leads to a more heterogeneous and less organized structure compared to cell 1. This irregular grain distribution may contribute to higher resistivity due to increased grain boundary scattering, which can impede charge carrier mobility and negatively affect the electrical performance of the AZO layer.

Figure 5.18 shows the AZO sample on the ITO seed layer in cell 3, which exhibits undefined and irregular large grains along the silicon substrate. This contrasts with the more uniform columnar grains seen in cells 1 and 2. The structural differences observed in cell 3 suggest that the ITO seed layer plays a critical role in modifying grain growth dynamics, promoting lateral grain expansion near the substrate and facilitating a more efficient charge transport pathway. Considering that the color-coded orientation maps from the silicon substrate, which is the cubic phase, are different from those of AZO thin films, which are hexagonal.

In summary, 4D-STEM results have demonstrated a structural comparison of the three different cell configurations: cell 1: AZO on a-Si:H, cell 2: AZO on nc-Si:H, and cell 3: AZO/ITO. The 4D-STEM is complemented by an automated crystal orientation analysis. The orientation and size of the grains were determined for all three cell types. Cell 1 had larger grains that were typically started at the interface. However, sample cell 2 started with small grains close to the substrate and the grain size increased along the thickness of the AZO film, which may explain the higher resistivity of cell 2. Typically, most of the grains in cells 1 and 2 were perpendicular to the substrate. This can be attributed to the on-par fill factor for cells 1 and 2. Sample cell 3 demonstrated higher grain sizes in the lateral direction close to the substrate and exhibited some perpendicular

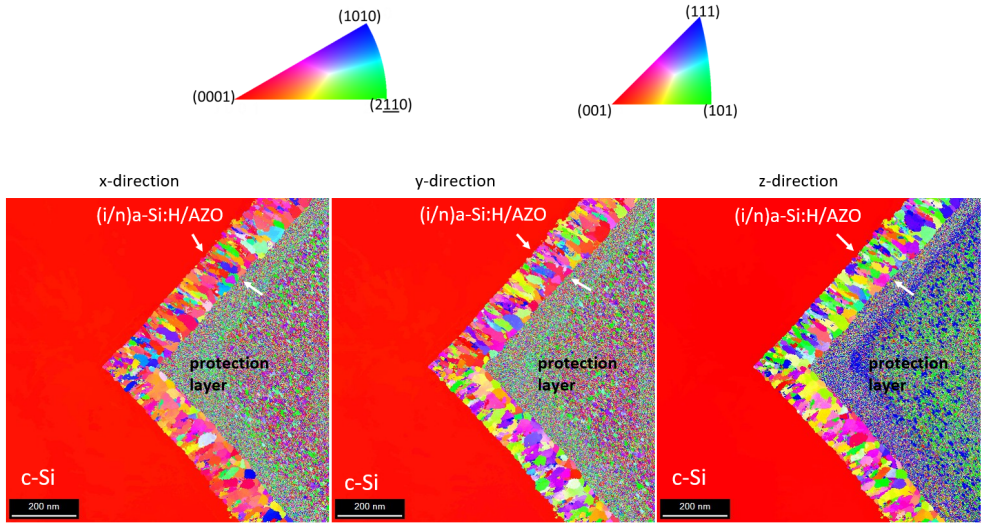

Figure 5.16: *The orientation map along the (x,y and z) direction of cells 1 from left to right. color code inverse pole figures for the Si substrate and AZO.*

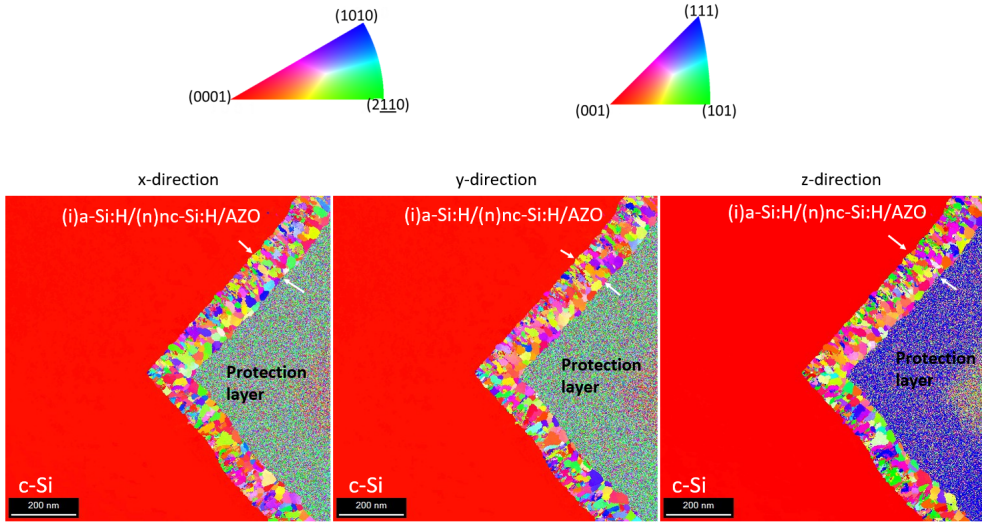

Figure 5.17: *The orientation map along the (x,y and z) direction of cell 2 from left to right. color code inverse pole figures for the Si substrate and AZO.*

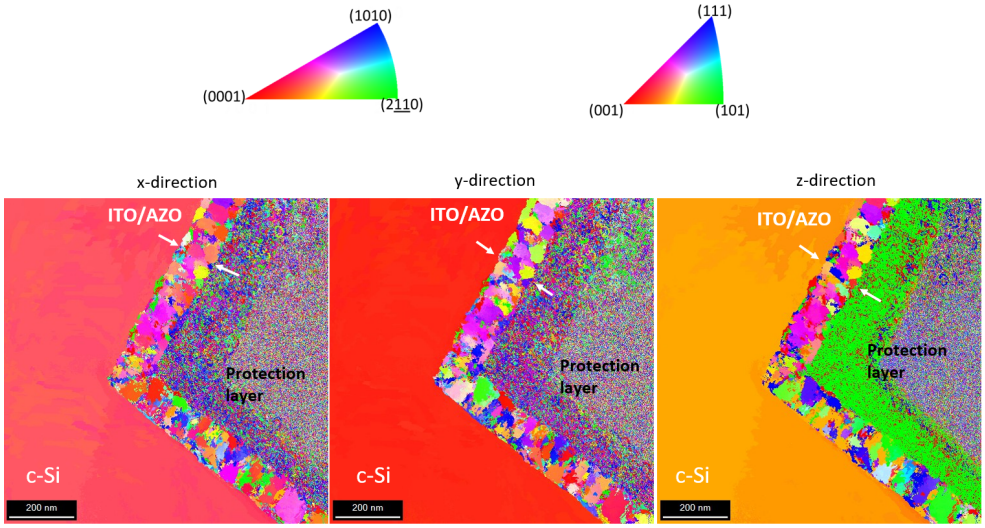

Figure 5.18: *The orientation map along the (x,y and z) direction of cell 3 from left to right. color code inverse pole figures for the Si substrate and AZO.*

growth at the top of the AZO film, which was attributed to the lower resistivity of cell 3 and a higher fill factor FF. On the other hand, cell 3 demonstrated superior grain growth, with larger lateral grains near the substrate and a transition to perpendicular growth at the top of the AZO film. This unique microstructure is likely responsible for lower resistivity and an improved FF in cell 3, further confirming the beneficial effects of incorporating an ITO seed layer in optimizing AZO-based TCO performance for SHJ solar cells.

Figure 5.19 shows the quantitative evolution of the change in the microstructure, specifically the grain size and diameter distributions, for different cell types. A minimum of 100 grains was selected, and the histograms for the grain diameter were measured based on the orientation of the grain boundary annotation layer.

The identified size of the grains varies for cell 1 is 70 nm, cell 2 is 50 nm and cell 3 is 90 nm, where smaller grains were observed in sample cell 2, whereas larger grains were observed in sample cell 3, suggesting a direct influence of the underlying substrate and seed layer on grain growth dynamics. For sample cell 1, as shown in **Figure 5.19 (a)** with AZO deposited on a-Si:H, grain boundaries were present in columnar growth, originating from the initial stages of growth. **Figure 5.19 (b)** shows sample cell 2 with AZO deposited on nc-Si:H, which exhibited irregular and small grains during the initial stages

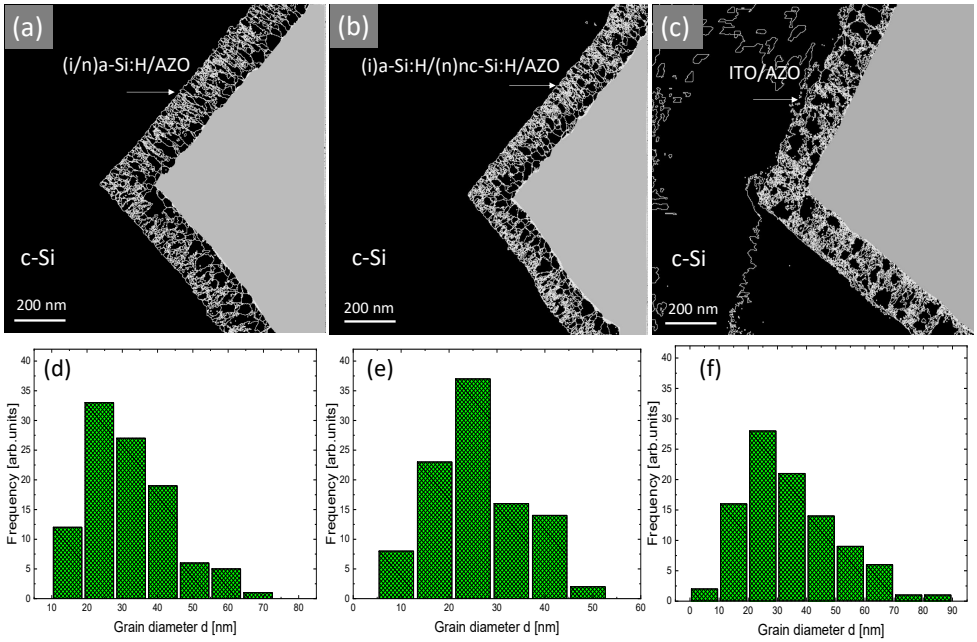

Figure 5.19: *(a, b, and c) Grain boundary annotation layer for cell 1 with AZO/a-Si: H, cell2 with AZO/nc-Si:H, and cell3 with AZO/ITO, respectively; (d, e, and f) Statistical analysis of grain size distribution.*

of the films. **Figure 5.19 (c)** sample cell 3 with AZO and seed-layer ITO exhibited large grains and irregular boundaries. The ITO seed layer appears to promote enhanced grain growth, facilitating the formation of fewer grain boundaries and a more uniform crystalline structure. The increase in grain size in cell 3 correlates well with its lower resistivity and higher charge carrier mobility, as observed in previous electrical performance. The irregular grain boundaries, while present, are significantly less dense than those in cell 2, further supporting the role of ITO in improving grain connectivity and overall film quality.

The statistical study revealed that the AZO deposited on a-Si:H had an average grain size of 31 nm, the AZO deposited on nc-Si:H has an average grain size of 26 nm and the AZO deposited on seed layer ITO had a 34 nm as illustrated in **Figure 5.19 (d, e, and f)**. The correlation between grain size, film morphology, and electrical conductivity suggests that optimizing the underlying layer composition can be an effective strategy for improving charge transport efficiency and device performance.

Analysis of the STEM images shows that the crystal structures of both cell 1 where AZO is deposited on the (n/i)a-Si:H/c-Si stack—and cell 3 where AZO is grown on an underlying ITO seed layer above the (n/i)a-Si:H/c-Si exhibit structural defects such as grain boundaries, vacancies, and impurities. These defects introduce scattering centers that hinder charge-carrier transport and reduce mobility. In AZO specifically, the grains display a columnar morphology oriented perpendicular to the substrate, which is characteristic of ZnO growth due to its polar lattice and the piezoelectric behavior along the c-axis [43]. In contrast, the nonpolar nature of In_2O_3 means that its surfaces do not exhibit spontaneous polarization effects similar to those of ZnO [13, 140]. This might also explain why the growth behavior of ITO contributes to high lateral conductivity, which is further supported by the increased carrier concentration and high fill factor, featuring a double-layer AZO/ITO in cell 3.

Overall, the improved mobility and higher fill factor observed for the AZO/ITO sample cell 3 can be largely attributed to its large grain size and grain boundaries. Conversely, the reduced charge carrier mobility of AZO on nc-Si:H can be attributed to a decrease in grain size within the bulk material. This may also suggest an increase in the film resistivity and a decrease in the fill factor for cell 2. Interestingly, the AZO on a-Si:H exhibited a consistent range of charge carrier mobility and fill factor, similar to that of AZO on nc-Si:H. This suggests that grain size alone may not be the sole determinant of electrical performance, and additional factors such as interface quality, defect density, and film passivation may also contribute to the overall device behavior.

5.6 Impact of magnetron sputtering on the structural properties

In this section, we study the influence of AZO sputtering methods on interface damage in SHJ solar cells. In a typical SHJ structure, the intrinsic and doped (i/n)a-Si:H layers are used to passivate the c-Si wafer surface [154], enabling effective carrier selectivity and minimal interface recombination [155]. To extract charge carriers laterally and maintain optical transparency, TCO layers, such as ITO or AZO are sputtered on top of the (i/n) a-Si:H layers [156]. For the fabrication of TCOs, magnetron sputtering is the most widely used technique due to its high deposition rate, good reproducibility, and capability for large-area deposition. Magnetron sputtering operates under vacuum conditions, utilizes the plasma excitation of a gas, typically argon, initiated by either a direct current (DC) or radio frequency (RF) power source. Nevertheless, sputtering processes, DC sputtering, especially at high power, often introduce more intense ion flux and energetic particle bombardment compared to RF sputtering [157]. **Figure 5.20 (a)** shows the diagram of the sputtering process, illustrating the differences between the various types of power.

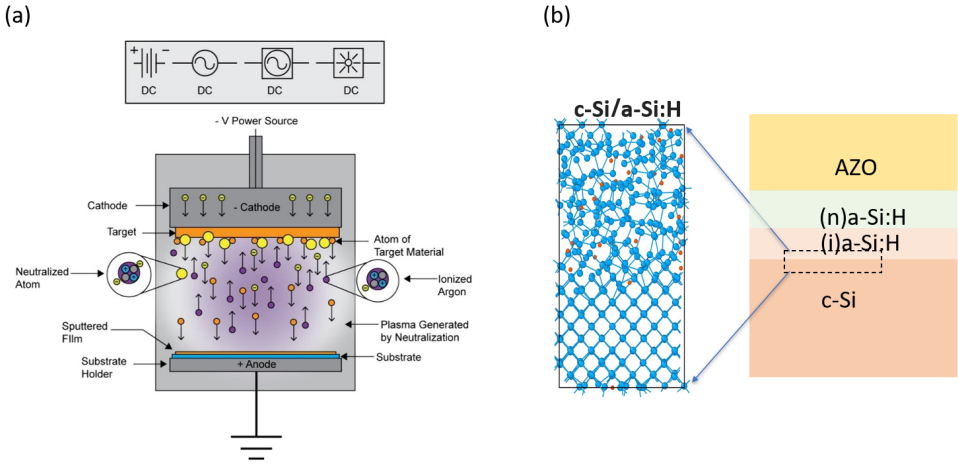

Figure 5.20: *(a) Diagram sputtering process, explaining the difference between the types of power [158]. (b) Schematic illustration of the SHJ solar cell layers, the inset shows an atomic-scale view of the a-Si:H/c-Si interface, highlighting the structural disorder and hydrogen passivation with red atom within the a-Si:H layer [158–160].*

These energetic interactions can disrupt the a-Si:H/c-Si interface, degrade passivation

quality, and consequently reduce V_{oc} and overall device efficiency [157]. Post-deposition treatments such as annealing or light soaking may partially recover electrical performance, but often cannot fully mitigate the underlying structural damage introduced during the AZO deposition step [157]. The damage is often attributed to fast particles generated at the cathode and directed to the substrate [156]. The major damage mechanisms are outlined below:

Figure 5.20 (b) shows the schematic of the crystal structure at the interface between c-Si and (n/i) a-Si:H [159]. First, DC sputtering usually produces high-energy argon ions (Ar^+) in the plasma, which ejects atoms from the AZO target. However, these ions can also strike the growing film and transfer kinetic energy to surface atoms. In thin-film stacks such as SHJ, where the a-Si:H layer is often only about 5–10 nm thick which is necessary for good passivating properties, ion penetration can go beyond the a-Si:H layer, affecting the a-Si:H/c-Si interface and creating dangling bonds at the a-Si:H/c-Si interface on a very short time scale, resulting in a lower level of surface passivation [156, 161, 162]. However, high-energy particle bombardment may also lead to local heating and energy transfer sufficient to partially recrystallize amorphous silicon at the a-Si:H/c-Si interface, such as epitaxial growth [163], which has been observed in HRTEM studies after TCO sputtering. Depending on the sputtering conditions, this can manifest as columnar crystal growth extending into an amorphous layer and the formation of small crystalline grains within the amorphous silicon region. Non-abrupt interfaces lead to band misalignment or potential wells. While epitaxial growth in the a-Si:H/c-Si may disrupt the passivation layers and thus decrease the efficiency of the solar cells [164].

Moreover, these epitaxial intrusions can also introduce strain, dislocations, or dopant redistribution, all of which adversely affect the electronic performance. Previous work by Shin et al. (2011) [165] demonstrated that increasing sputtering power during pulsed DC magnetron deposition of AZO significantly increases in-plane compressive stress in the films, caused by high-energy collisions of recoiling Ar^+ and O^- ions. This strain was correlated with degradation in crystallinity, increased resistivity, and chemical non-stoichiometry highlighting the critical role of stress in sputter-induced damage mechanisms. Similarly, Cebulla et al. (1998) [166] compared AZO films deposited by RF, DC, and combined RF/DC magnetron sputtering and demonstrated that RF excitation leads to lower intrinsic stress and better crystallinity, due to higher ion-to-neutral flux ratios and improved mobility. Their findings confirmed that lower mechanical stress particularly in RF-sputtered films directly results in higher carrier mobility and better conductivity.

These studies underscore that managing stress during deposition is essential for minimizing sputter damage and preserving interfacial and electrical integrity in AZO-based contact stacks. Huang et al. (2015) [167] compared ITO films deposited by pulsed DC and RF sputtering under low-temperature conditions, showing that while both methods introduce sputter damage, PDC causes more severe ion bombardment damage, whereas RF-induced UV radiation leads to surface distortion and defect formation in the amorphous layer. High-resolution TEM images revealed epitaxial-like silicon growth near the ITO/a-Si interface more pronounced in PDC-deposited samples further confirming that sputtering conditions critically affect structural integrity at the a-Si/c-Si interface. Conventional TEM provides limited information on the lattice stress and orientation gradients, particularly near the amorphous/crystalline boundaries. This technique enables high-resolution, spatially resolved analysis of strain gradients and grain orientation, which accounts for the observed electrical differences, such as the reduced V_{oc} in DC-sputtered devices. By correlating structural changes with solar cell performance, this study aims to provide new insights into sputter-induced interface degradation and inform optimized TCO deposition strategies for high-efficiency SHJ solar cells [159].

5.6.1 Electrical Performance

The performance of SHJ solar cells is significantly influenced by the TCO deposition process. In particular, the choice of sputtering technique for AZO plays a critical role. J-V measurements reveal that DC-sputtered AZO layers result in a lower V_{oc} compared to RF-sputtered AZO. This suggests that the DC sputtering process introduces more severe damage to the underlying layers damage that is not fully recoverable even after post-deposition annealing and light soaking treatments [167].

Figure 5.21 presents the J–V characteristics of SHJ solar cells fabricated with different front contact materials. From these measurements, it is evident that the use of DC-sputtered AZO leads to a lower V_{oc} compared to RF-sputtered AZO, as shown in **Figure 5.21(a)**. This reduction in V_{oc} suggests that the DC sputtering process may introduce damage to the underlying layers, which cannot be fully mitigated by post-deposition annealing or light soaking treatments. In terms of J_{sc}, RF-sputtered AZO demonstrates a comparable or slightly higher J_{sc} than DC-sputtered AZO, as shown in **Figure 5.21(b)**. Furthermore, the FF is noticeably higher in cells employing RF-sputtered AZO as in **Figure 5.21(c)**, indicating improved contact quality and reduced series resistance. As a result,

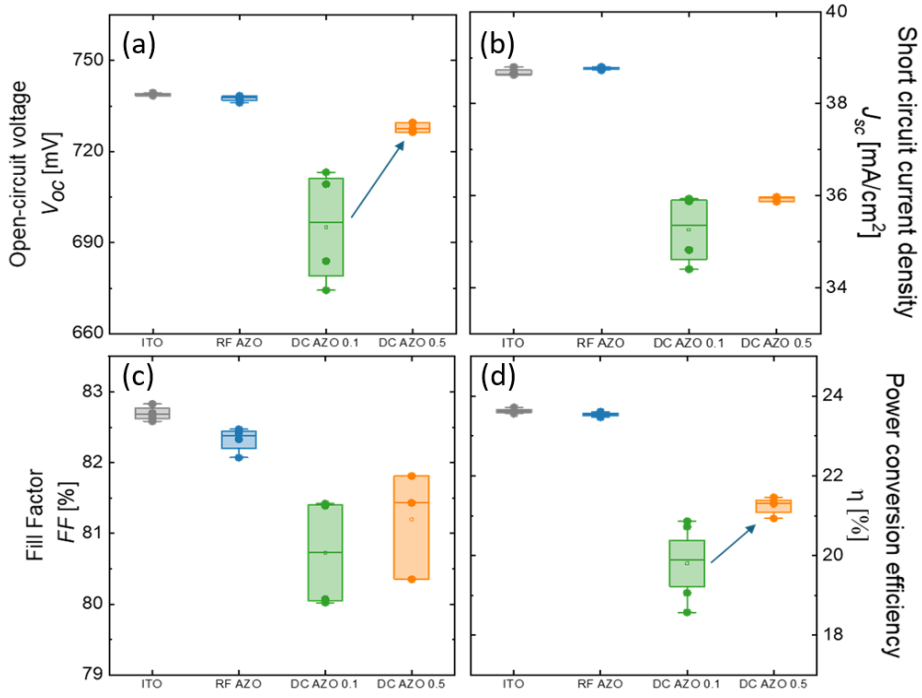

Figure 5.21: *The evolution of (a)open-circuit voltage (V_{oc}),(b) short-circuit current density (J_{sc}), (c) fill factor (FF), and (d) efficiency (η) of silicon heterojunction solar cells.*

the overall η is significantly enhanced in RF-sputtered AZO-based devices. In contrast, the DC-sputtered AZO-based cells exhibit the lowest efficiency among the samples tested, with a maximum efficiency of approximately 21%, as depicted in **Figure 5.21(d)**.

Figure 5.22 show the high-resolution TEM provides further evidence supporting this observation. Huang et al. (2015) [167] have reported that plasma damage caused by pulsed direct current sputtering (PDC) leads to more pronounced alterations in the a-Si layer. In these cases, epitaxial silicon growth, typically indicative of structural recovery or crystalline quality, is found to extend much closer to the ITO/a-Si interface when DC sputtering is used. Conversely, RF-sputtered samples exhibit epitaxial features only near the a-Si/c-Si interface, suggesting less plasma-induced damage. This difference in structural impact between DC and RF sputtering highlights the importance of selecting a deposition method that minimizes damage to the delicate a-Si passivation layers in SHJ cells. Detailed TEM analysis thus serves as a crucial diagnostic tool for understanding sputtering-induced degradation and guiding process optimisation toward higher-efficiency solar cells.

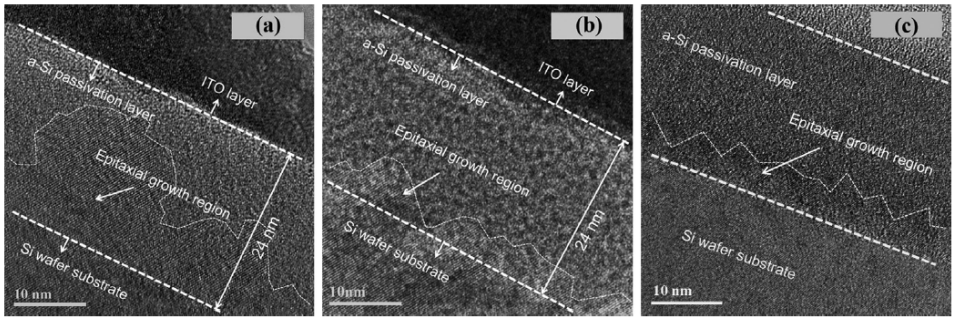

Figure 5.22: *TEM images showing sputter damage caused by (a) PDC and (b) RF sputtering methods, along with (c) a reference a-Si sample without any ITO coating (free from sputter damage), adapted by [167].*

5.7 Conclusion

In conclusion, the study used 4D-STEM and HRTEM to characterize the microstructure of AZO and ITO thin films on silicon heterojunction solar cells. It demonstrates that the incorporation of an ITO seed layer beneath the AZO film substantially enhances grain growth, improves crystallinity, and reduces film resistivity. AZO films deposited on a-Si:H

exhibited well-oriented columnar grains aligned perpendicular to the substrate, promoting better carrier mobility. In contrast, AZO deposited on nc-Si:H displayed smaller, irregular grains, which introduced higher grain boundary density and reduced mobility. The AZO/ITO configuration showed the most favorable microstructure, with larger, laterally extended grains that contributed to superior charge transport, higher fill factors, and improved overall efficiency. Moreover, this chapter highlights that the magnetron sputtering process critically affects the structural integrity of the passivation interface. While magnetron sputtering is advantageous for large-area deposition and uniformity, its plasma conditions, particularly in DC mode can induce energetic ion bombardment that damages the thin amorphous silicon passivation layers. Such damage introduces defects and epitaxial intrusions at the a-Si:H/c-Si interface, reducing surface passivation quality and lowering the V_{oc}. Comparatively, RF sputtering produces less energetic plasma, resulting in reduced interface damage, lower intrinsic stress, and improved crystallinity and conductivity in the deposited AZO layers.

6 Ultraviolet-induced degradation in TPCs solar cells

Ultraviolet (UV) radiation presents a critical reliability concern for SHJ solar cells, as high-energy photons can induce structural and electronic changes within passivation and contact layers. These alterations may compromise interface quality, increase defect densities, and degrade overall device performance. This chapter examines the impact of UV exposure on SHJ devices, with particular focus on TPC structures, to clarify the material mechanisms underlying their observed performance deterioration. This chapter covers the brief review of TPCs solar cells and the degradation of the solar cells in section 6.1, while section 6.2 describes the samples used in this study, in section 6.3 evaluates the influence of UV irradiation on TPC-SHJ device performance. lastly section 6.4 presents the corresponding microstructural and crystallographic analyses.

6.1 Brief review of UVID degradation in TPCs solar cells

One of the significant advancements in silicon solar cells in recent years is the enhancement of silicon surface passivation [156, 168]. This is evident in the record-breaking silicon solar cells developed recently. Examples include tunnel oxide passivated contact (TOPCon), poly-Si on oxide (POLO), and SHJ technologies. All of these utilise poly-Si or hydrogenated a-Si layers as passivation layers deposited on the silicon wafer surface [38]. A substantial portion of these generated electron–hole pairs will be lost due to recombination without significantly contributing to charge carrier collection at the terminal of the device. The parasitic absorption from the passivating layer remains an issue, particularly on the front side of such well-passivated cells. TPCs have been introduced as a novel alternative to a-Si:H-based front contacts. TPCs are designed to decouple the passivation and carrier selectivity functions using a wide bandgap material such as SiC, deposited in combination

with an ultrathin silicon oxide (SiO_2) tunnel layer at the c-Si interface. This structure significantly reduces parasitic absorption losses in the short-wavelength spectral region, efficient electron transport, and high optical transparency [14, 143, 169]. Recent studies have demonstrated that μc-SiC:H/SiO_2 stacks fabricated via hot-wire chemical vapor deposition (HWCVD) can achieve excellent passivation quality with implied exceeding V_{oc} 728 mV, and enable device efficiencies approaching 24% without requiring any post deposition [170]. The thin film deposition of μc-SiC:H by various established chemical vapour deposition (CVD) techniques has been proven to be difficult, since unwanted phase mixtures of Si and SiC occur. HWCVD has successfully enabled the growth of μc-SiC:H films at low temperature with c-SiC grains [171]. The optimum conditions for crystalline growth are governed by the growth conditions, such as pressure during growth [58] or dilution of monomethylsilane (MMS) in hydrogen. Typically these films are of microcrystalline nature, showing a columnar growth of SiC crystals. Its crystallinity gives rise to both the high transparency and the high electrical conductivity [172].

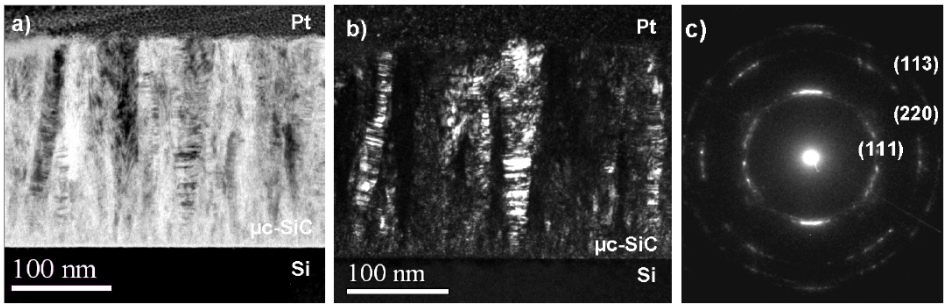

Figure 6.1: *Bright-field (BF) (a), dark-field TEM image (DF) (b), and electron diffraction pattern (c) of a μc-SiC:H film with a relative doping level of 0.001. The film exhibits a columnar arrangement of crystalline grains. The diffraction pattern confirms the predominance of the cubic phase, while the arc-shaped intensity along the (111) ring indicates a preferred orientation of the (111) planes perpendicular to the film growth direction [172].*

Figure 6.1 (a,b) show BF and DF images of a μc-SiC:H film with a relative doping level of 0.001 reveal a columnar structure varying between 8 nm and 30 nm in width, **Figure 6.1 (c)** electron diffraction pattern showing an arc-like intensity distribution along the (111) ring. The diffraction pattern is dominated by reflections, which can be assigned to the cubic phase of SiC (3C-SiC) [171].

Additionally, Köhler et al. have shown that a proper deposition of double-layer nc-SiC:H together with SiO_2 layer can be an option providing not only transparency but

also passivation and an acceptable level of conductivity [14]. **Figure 6.2 (a)** depicts the schematic of the c-Si solar cells used in this study. In the diagram, nc-SiC:H, pass. refers to the passivation layer, while nc-SiC:H, cond. indicates the conductive layer within the double-layer structure of nc-SiC:H.

The two primary challenges to maintaining the TPC's competitiveness against other innovative methods are the iV_{OC} – FF trade-off related to the passivation layer thickness, as discussed in [173], and the reduction in V_{OC} after sputtering, as discussed in [14]. Degradation studies have shown that nc-SiC:H layers are prone to structural disorder, hydrogen depletion, and increased resistivity under prolonged UV illumination, which can compromise both passivation quality and electrical performance.

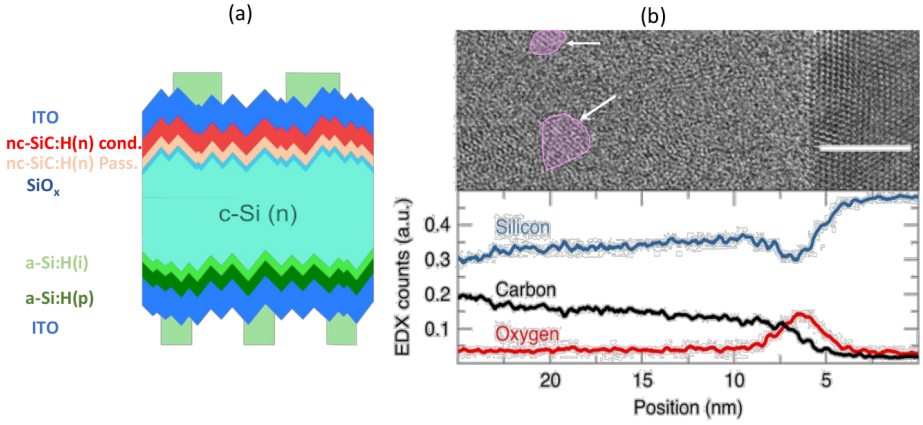

Figure 6.2: *(a) The schematic illustration of a standard n-type c-Si substrate SHJ solar cell used TPC on the front side, using stack layers ITO, nc-SiC:H pass. represents the passivation layer, whereas nc-SiC:H cond represents the conductive layer and SiO_2. (b) HRSTEM bright-field image and EDX measurement of the c-Si(n)/SiO_2/nc-SiC:H(n) interface. The arrow is to show the SiC crystallites embedded in an amorphous matrix. The EDX line profile is obtained at a similar location, which clearly shows the oxygen presence at the interface to the silicon substrate, scale bar, 5 nm [14].*

Over the past decade, researchers have taken a closer look at stability and failure mechanisms in SHJ cells and modules. Several studies highlight the important role of hydrogenated passivating contacts in these degradation processes. For example, degradation can occur even before module assembly, during the storage of the cell. This early dark degradation has been linked to the structural rearrangement in the metastable (i)a-Si:H passivating layer [174]. Research highlights that SHJ solar cells, particularly those with-

out encapsulation, are notably affected by UV radiation compared to other contemporary c-Si solar cells [175]. After UV exposure, V_{oc} and FF of SHJ cells decreases significantly, probably due to UV-induced hydrogen effusion near the interface of a-Si:H/c-Si.

It is worth noting that this study focuses on front-junction SHJ cells, in which the a-Si:H(p)/a-Si:H(i) stack is positioned on the illuminated side and is therefore directly exposed to the UV photons. These front-side p/i layers are known to contain metastable hydrogen configurations and are significantly more susceptible to UV driven hydrogen effusion, bond breaking, and interface defect formation. As a result, the degradation in V_{oc} and FF reported in this study [176] is strongly linked to the front-junction architecture and may not fully represent the behavior of rear-junction SHJ cells, where the UV exposure and material sensitivity of the front stack differ substantially. Fourier transform infrared (FTIR) spectra obtained by Ye et al. revealed that UV exposure leads to a reduction in the total bonded hydrogen content in a-Si:H layers and at the a-Si:H/c-Si interface, pointing to this as a root cause of UVID [176]. However, the investigation into different a-Si:H layers and cell precursors reveals that high-energy UV photons can break Si-H bonds in all types of a-Si:H layers, thereby increasing the defect density at the a-Si:H/c-Si interface [177].

The SiO_2 prevents interface damage and simultaneously reduces the dangling bond density at the c-Si(n) surface [178]. Köhler et al reported that the interface of c-Si(n)/SiO_2/nc-SiC:H(n) is undamaged, which is revealed in the HRSTEM image in **Figure 6.2 (b)**. Close to the SiO_2/c-Si interface, the SiC layer is amorphous, whereas nc-SiC crystals embedded in an amorphous matrix are observed in the bulk of the material as indicated by the arrow. The energy dispersive EDX line profile, obtained at a comparable location within the sample, additionally shows that aside from silicon, oxygen is present at the interface to the crystalline silicon substrate, indicating that the SiO_2 is not entirely removed during the HWCVD process [14].

The objective of this chapter is to understand the UV degradation in the TPC and the mechanism behind the V_{oc} and FF decline due to UV illumination, there must be links between the electrical properties and the material properties. This decline could originate from either the interface or the bulk materials. Therefore, observing the microstructure changes of various films can provide insights into the process.

6.2 Samples for the study

The fabrication process of the TPCs solar cells were described in section 3.6.2. For the UV Exposure testing setup: UV exposure experiments were carried out in the lab of SHJ solar and module manufacturer, Anhui Huasun Energy Co.,Ltd. The UV light source simulator was with A+ ultraviolet B(UVA & UVB) irradiance set to an intensity of 200 W m^2. The UVB(280–320 nm) content was around 5.9% of the total spectral irradiance. After 300 h of exposure, the cumulative UV irradiance was equivalent to a UV dose of 60 kWh m^2. The temperature of the UV chamber was kept at 60°C [177].

Table 6.1: *Overview of the samples investigated in this study and their performance parameters.*

Sample ID	method of preparation	V_{oc} (mV)	J_{sc} (mA/cm^2)	FF (%)	η(%)
#1 Before UV	FIB	673	39.1	79.3	23.1
#2 After UV exposure	FIB	658	38.45	69.7	17.6
#3 Before UV	Conventional TEM	673	39.1	79.3	23.1
#4 After UV exposure	Conventional TEM	658	38.45	69.7	17.6

Device characterization: The PV parameters (V_{OC}, J_{SC}, FF, and η) of SHJ and TPC solar cells were measured by current density–voltage (J–V) measurements under standard test conditions (AM 1.5G, 25°C, 1000 W m^2). All of these measurements were integrated into the LOANA solar cell analysis system from PV tools.

Cross-sectional TEM specimens were prepared using two methods: the conventional technique with a final step using the PIPS II ion milling at (6-1) eV to ensure high electron transparency, and with the FIB method, as described in the section 3.5. **Figure 6.3 (a,b)** shows the SEM image of the cross-section lamella for this study. The surface of the thin film showing the pyramids of the texture for the samples, before UV exposure and after UV exposure, respectively, as shown in **Figure 6.3 (c,d)**.

Diffraction pattern templates were generated from the Crystallographic Information Framework (CIF) files for each material. The Si substrate is cubic, with a space group symmetry of Fd-3m (#227) and lattice parameters of a= 5.4305 Å and c= 5.4305 Å (JCPDS #51-688). 3C-SiC refers to nc-SiC:H layers, which are cubic, with lattice parameter a= 4.348 Å, and c= 4.348 Å. The ITO layer exhibited a cubic bixbyite structure with a space

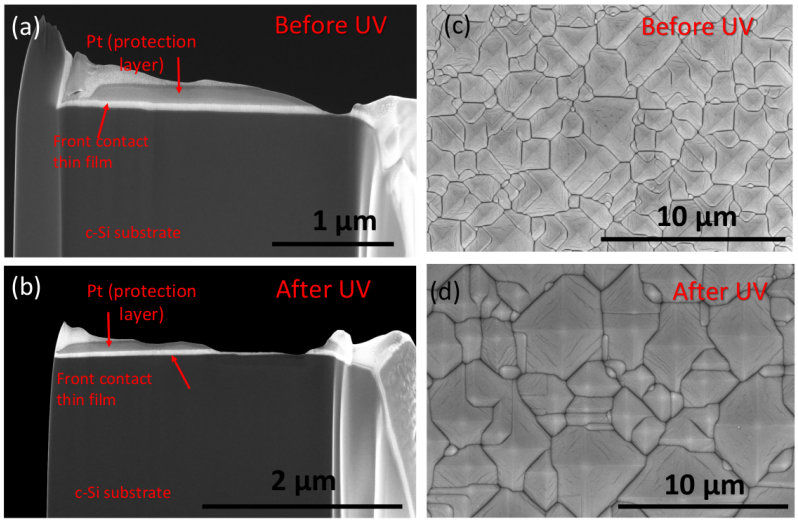

Figure 6.3: *(a)Scanning electron microscope (SEM) image of the thinned lamella for samples before UV exposure and with UV exposure, respectively (a and b), surface of the thin film showing the pyramids of the texture for the samples before UV exposure and with UV exposure, respectively (c and d).*

group symmetry of Ia3 (#206) and lattice parameters of a= 10.117 Å and c=10.118 Å (JCPDS #06-0416).

6.3 TPCs solar cell performance

In order to adequately understand the TPCs solar cells, it is necessary to see the performance of this solar cells. This section describes the results that were obtained by (J–V) measurements, and gives a theoretical explanation of the experimental data.

6.3.1 J-V characteristics

Figure 6.4 presents the changes in cell performance induced by UV irradiation. The accumulated UV dose was maintained at 60 kWh m^{-2}. Two types of samples have been examined: the SHJ and the TPC. The UVID behavior varied used front contact, as shown in **Figure 6.4 (a)**. Exposure to UV light resulted in a reduction in the efficiency of both types of samples. However, the same dose of UV irradiation reduced the efficiency of SHJ samples by 2.58% on average and in absolute terms, but this resulted in a significantly greater loss of efficiency of TPC samples, with a reduction of 9.34%. This level of UVID has not been reported for solar cells using heterojunction technology, this severe decline may indicates that the choice of front-side passivating contact plays a critical role in determining UVID susceptibility. A general decrease in efficiency-related parameters provides an explanation.

Figure 6.4 (b) shows an observable decrease in the J_{SC} of the TPC samples after UV irradiation compared with the as-deposited samples. A loss of J_{SC} of approximately 4.66 mA/cm^2 appeared in the TPC samples. The J_{SC} of the SHJ samples decreased by approximately 1.19 mA/cm^2, which is also larger than the observation by other researchers in which the change of J_{SC} was regarded as rather small [175, 176]. This can be attributed to the thinner a-Si:H front stack used in our SHJ samples, which allows a greater fraction of UV photons to reach and degrade the a-Si:H/c-Si interface. The much larger J_{SC} loss in TPC samples reflects additional degradation in the wide-bandgap nc-SiC:H layer, which strongly affects both transparency and carrier collection. To address this gap, several recent works have specifically examined UVID in rear-junction SHJ cells, providing a more appropriate basis for comparison with the present study.

Figure 6.4 (c) presents the changes in fill factor (FF). A sharp FF loss of 13.9% was observed for the TPC samples. In contrast, the FF of the SHJ samples reduces by 2.7%. Such a sharp FF reduction in the TPC devices is consistent with UV-induced increases in series resistance, grain-boundary disorder, and reduced carrier mobility within nc-SiC:H.

UV-induced reduction in V_{OC} has been widely discussed in the literature. Sinha et al. observed a decrease in V_{OC} of 3% after UV exposure for 2000 h. This work and the other two studies by Yang et al. and Thome et al. were carried out with a front-junction configuration of SHJ solar cells, which indicates direct exposure of the PN junction to UV light [179, 180]. However, the widely used SHJ cell configuration in the industry features a rear-junction design; therefore, these observations may not reflect the actual UVID present in cells that will be deployed in the future. Several studies have been conducted on rear-junction configurations. Ye et al. observed a 1% loss of V_{OC} in rear-junction SHJ solar cells after exposure to 60 kWh m^{-2} at 40°C [176].

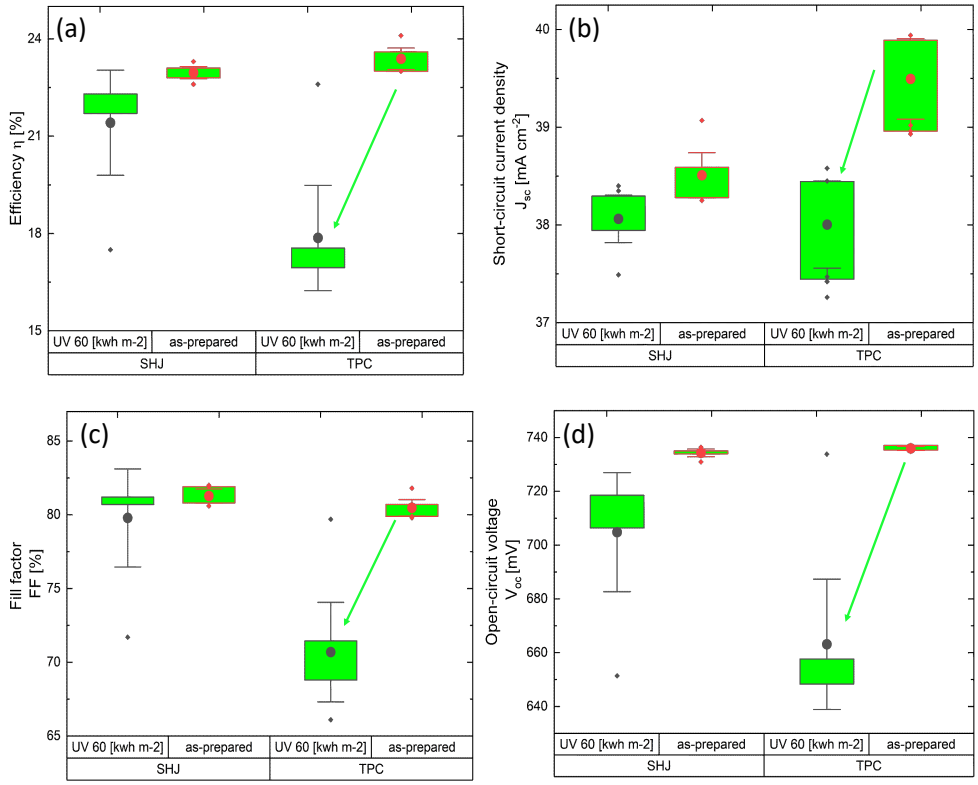

Figure 6.4: *The evolution of (a) efficiency, (b) short-circuit current density, (c) fill factor, and (d) open-circuit voltage of silicon heterojunction solar cells using (i) a-Si:H based SHJ contact or nc-SiC:H based TPC contact after a UV irradiation with the UV dose of 60 kWh* m^{-2}.

Significant V_{OC} losses were also observed in both samples, approximately 38.7 mV

for the SHJ samples and 129.8 mV for the TPC samples, as shown in **Figure 6.4 (d)**. Considering the cell configuration and UV dose, only the study by Ye et al. can be compared with our results for the SHJ samples. The relative V_{OC} loss of the SHJ samples was calculated as 5.3%, which is larger than that reported by Ye et al. This could be explained by two factors. On the one hand, our experiments were carried out at room temperature, while the one referred to was at 40°C; the temperature difference might affect the degradation of passivation quality. Yang et al. reported a relationship between the decline in V_{OC} and temperature [179]. They argued that higher temperatures may accelerate the degradation process. Nevertheless, this observation was performed on front-junction cells, and systematic work is still missing. However, a thinner a-Si:H stack was applied here on the front side of the SHJ samples; therefore, more UV photons passed through the a-Si:H layer, reaching the a-Si:H/c-Si interface. This may have resulted in greater V_{OC} losses. None of the literature has reported such a huge decline in V_{OC}, as observed in TPC samples.

6.4 Insight into ITO/nc-SiC:H front contact microstructure

In this section, the focus will be on identifying the microstructure of the ITO and TPC stack ((n)nc-SiC:H cond./(n)nc-SiC:H pass./SiO_x), using TEM, EDX as well as the phases and crystallographic orientations of the grains within the functional front contact layers using the 4D-STEM technique. By correlating grain structure and orientation with electrical performance, we aim to reveal how microstructural evolution contributes to UVID in TPC-based SHJ solar cells.

Figure 6.5 shows side-by-side high-resolution TEM images of TPC-SHJ samples prepared by conventional TEM and the inset fast fourier transform (FFT) of the structure. **Figure 6.5 (a)** image corresponds to a sample before UV exposure, showing relatively uniform layers and smooth interfaces, especially in the SiO_x/(n)nc-SiC:H pass. region.

On the other hand, the sample after UV were exposed to 15 kWh m^{-2} UV, and it shown in **Figure 6.5 (b)**, in this case, a distinct structural changes are observed, including increased contrast variations and localized crystalline domains within the (n)nc-SiC:H layer, which are indicative of phase transformations or defect formation due to UV exposure, the FFT pattern from the UV-exposed sample displays slightly broadened

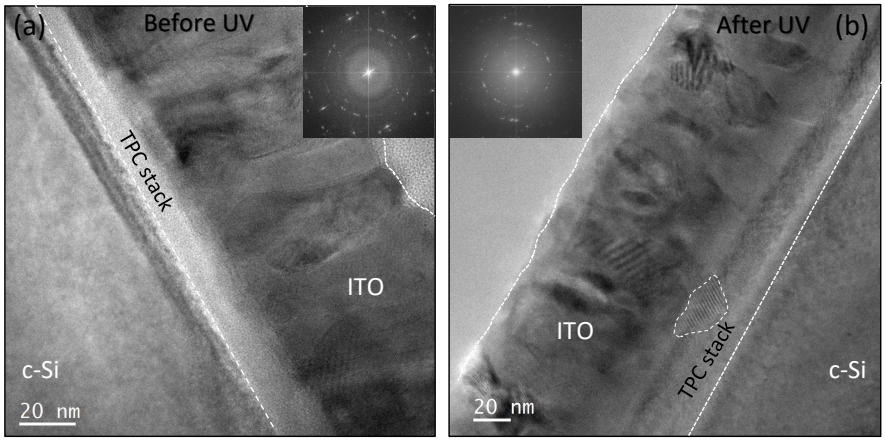

Figure 6.5: *Cross sectional TEM images of ITO/TPC stack/c-Si samples and the corresponding FFT pattern inset for the samples before UV exposure in (a) and after UV exposure in (b).*

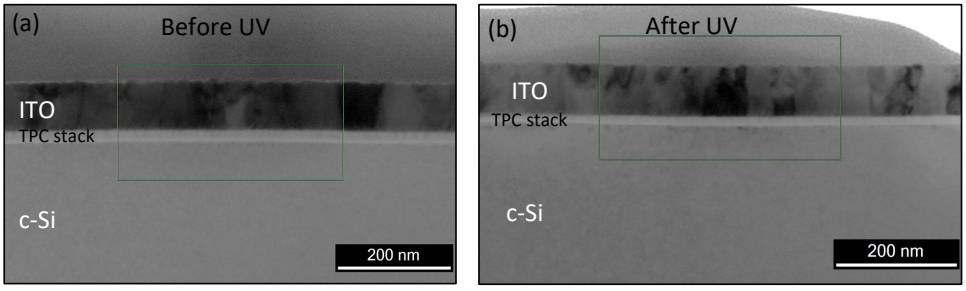

Figure 6.6: *High annular dark-field (HAADF) STEM overview images obtained before UV exposure and after UV exposure (a and b) respectively, with scale bar 200nm.*

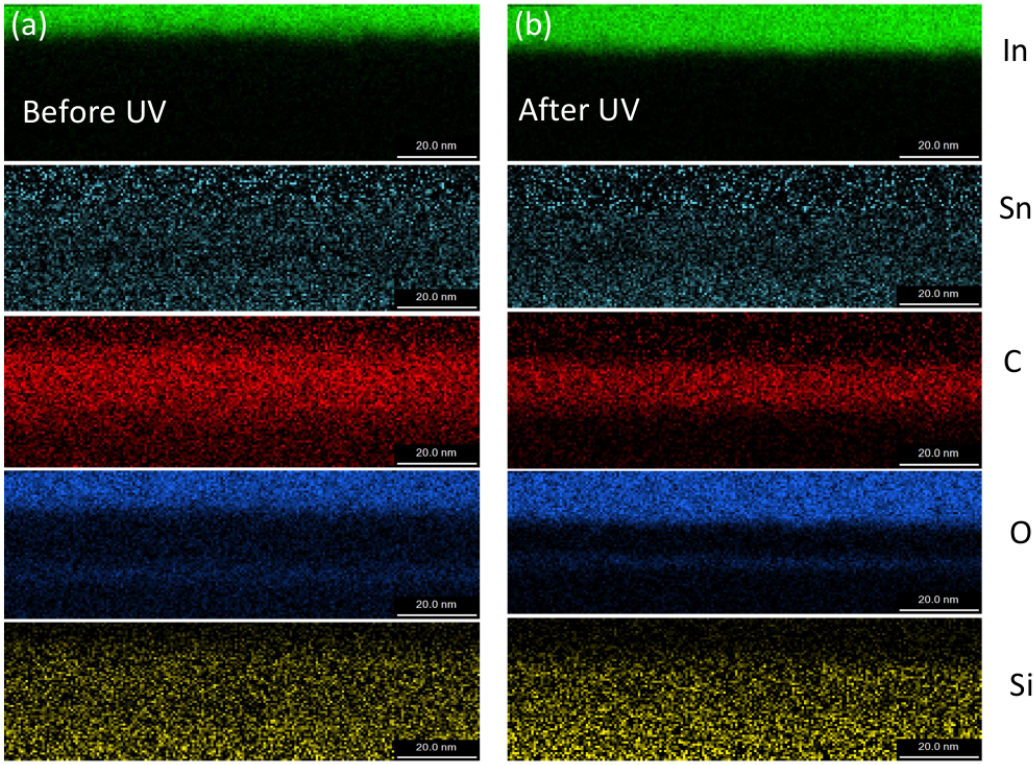

Figure 6.7: *EDX elemental maps of the ITO/TPC stack/c-Si interface before (a) and after (b) UV exposure. Elemental distributions of In, Sn, C, O, and Si are shown to evaluate potential chemical changes induced by ultraviolet illumination.*

diffraction rings compared to the sample before UV. These results suggest that UVID can affect the crystallinity, interface quality, or defect states in passivating contact layers, potentially affecting the electrical and performance of the solar cell.

Figure 6.6 (a,b) shows the HAAD-STEM overview images obtained before and after UV exposure, respectively. HAADF-STEM imaging was employed to assess the structural integrity of the ITO/TPC/c-Si stack both before and after UV exposure, from that the EDX elemental mapping were conducted.

In **Figure 6.7 (a,b)** show the EDX mapping of the area which focusing on the TPC stack. The compositional mapping reveals that the overall distribution of key elements (In, Sn from ITO; C and O and Si) remains largely unchanged after UV exposure. No significant elemental diffusion or migration is observed across the interfaces, suggesting that large-scale compositional changes do not primarily drive the UVID. It is also shown that the c-Si/SiO_2 interface, an accumulation of oxygen can be clearly found between the c-Si/nc-SiC:H(n), which indicates the existence of the silicon tunnel oxide. However, subtle intensity variations in the C and O maps after UV irradiation may indicate minor restructuring or loss of hydrogen-rich bonds within the nc-SiC:H layer, consistent with previously reported UV-induced hydrogen depletion.

6.4.1 Mapping grains in the ITO/nc-SiC:H front contact

The nanostructural changes in the nc-SiC:H cond./nc-SiC:H pass. layers after UV exposure influence device performance. The 4D-STEM technique enables detailed orientation and phase mapping, allowing for precise characterization of the TPC stack ((n)nc-SiC:H cond. and (n)nc-SiC pass./SiO_x). The STEM imaging was initiated by aligning the sample to a low-zone axis on the c-Si substrate. The diffraction patterns were then recorded with the incident beam, and an orientation map was reconstructed by indexing each diffraction pattern within the STEM scan area using a template matching algorithm.

The analysis was performed using integrated, near real-time 4D STEM data acquisition and processing with a TESCAN TENSOR operated at 100 kV acceleration voltage. The scanning frame areas were a large field of view (L-FOV) $400nm \times 200nm$ and a pixel size of 2 nm, and a small field of view (S-FOV) $120nm \times 40nm$ and a pixel size of 1 nm. The convergence half-angle of 2 mrad, generating a probe size of approximately 1.169 nm and a probe current of 266.7 pA. The following figures present the microstructure comparison of the ITO and nc-SiC:H stacks before and after UV exposure using 4D-STEM, recorded

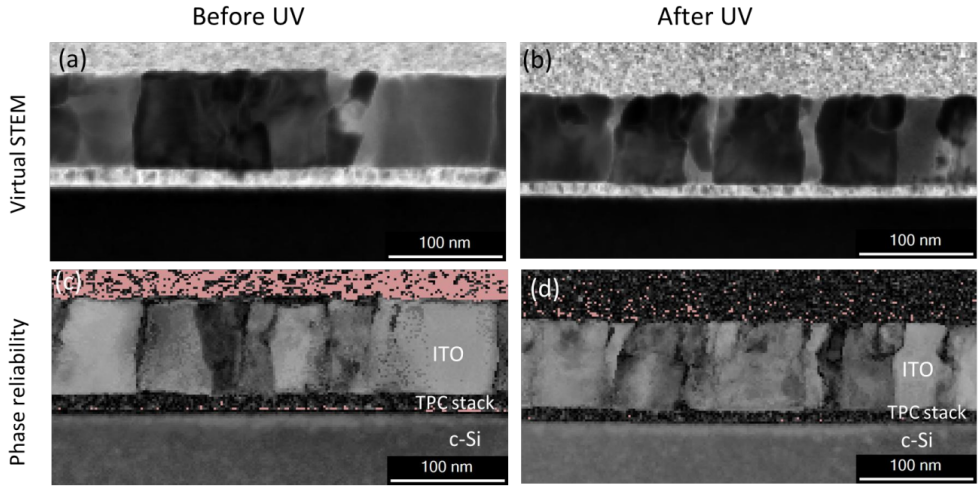

Figure 6.8: *Virtual bright-field STEM images of ITO/TPC stack/c-Si samples before UV exposure in (a) and sample after UV exposure in (b). Phase reliability for samples before and after UV exposure in (c) and (d), respectively. The scanning area is* $400nm \times 200nm$ *with a pixel size of 2 nm.*

along the [100] direction of the silicon substrate. **Figure 6.8** presents a L-FoV virtual bright-field scanning transmission electron microscopy (BF-STEM) and phase reliability images that compare the structure of ITO/nc-SiC:H cond./nc-SiC:H pass./SiO_x/c-Si solar cell stacks, before UV and after UV samples. The sample was subjected to a UV dose of 15 kWh m^{-2}.

In **Figure 6.8 (a) and (b)**, the sample before UV exposure and after UV exposure shows approximately a typical ITO layer, showing a dense columnar structure with well-defined grain boundaries. **Figure 6.8 (c,d)** presents phase reliability derived from STEM with an L-FOV for samples before and after UV exposure, respectively. In the case of ITO, columnar-grown ITO grains are uniformly distributed in both sample, and barely any change in the phase can be observed, suggesting a stable microstructure of the ITO film.

A detailed comparison of the TPC layers in the S-FOV is undertaken for the samples before and after UV exposure. **Figure 6.9 (a,b)** presents virtual BF-STEM images highlighting regions of interest within the TPC stack beneath the ITO. **Figure 6.9 (c,d)** presents a phase reliability, the nc-SiC:H passivation layer near the c-Si in the sample contains some amorphous phases before UV exposure, while it appears more crystalline after

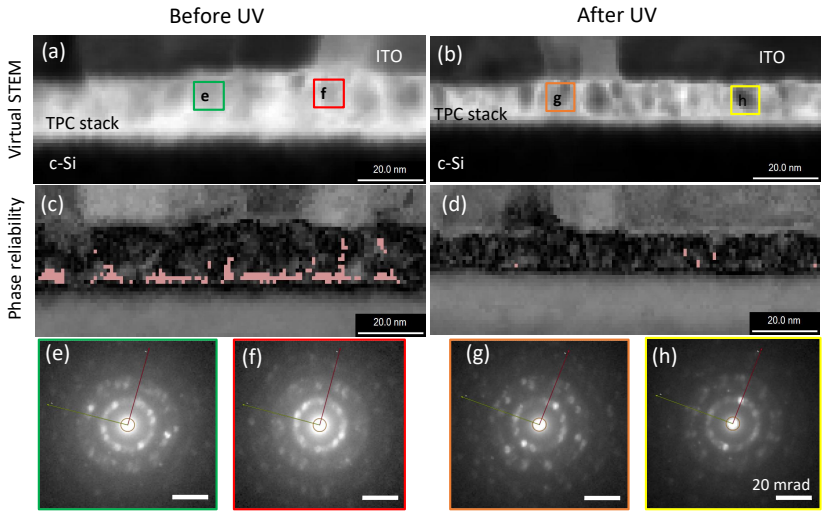

Figure 6.9: *Virtual bright-field STEM images of ITO/nc-SiC:H/SiO_x/c-Si samples before UV exposure in (a) and sample after UV exposure in (b). Phase reliability for samples before and after UV exposure in (c) and (d), respectively. The scanning area is* $120nm \times 40nm$ *with a pixel size of 1 nm.*

UV exposure. However, this is also may indicate to the lower reliability in this regions.

The diffraction patterns extracted from different regions marked in virtual BF-STEM in (a and b) confirm the crystallite of TPC layers and ITO. In the sample before UV exposure **Figure 6.9 (e,f)** diffraction rings are sharper and more continuous. In contrast, in the sample after UV exposure, **Figure 6.9 (g,h)** shows that rings appear more diffuse, wheres all the recorded diffraction patterns contain signal from multiple grains from ITO thin film and c-Si.

The orientation maps along the (x,y and z) directions were obtained, where the electron beam of the microscope is aligned with the z- **Figure 6.10 (a-c)** shows a 4DSTEM orientation map of the microstructural evolution of the sample before UV exposure for the L-FOV on the z-axis, y-axis and x-axis, respectively. However, **Figure 6.10 (d-f)** presents the orientation map of the sample after UV exposure. **Figure 6.10 (j)** considering that the color coded orientation maps from the Si substrate, which is the cubic phase, and of ITO thin films, which is cubic bixbyite.

Figure 6.11 (a-c) shows the orientation map of the microstructural evolution of the sample before UV exposure for the S-FOV on the z-axis, y-axis and x-axis, respectively.

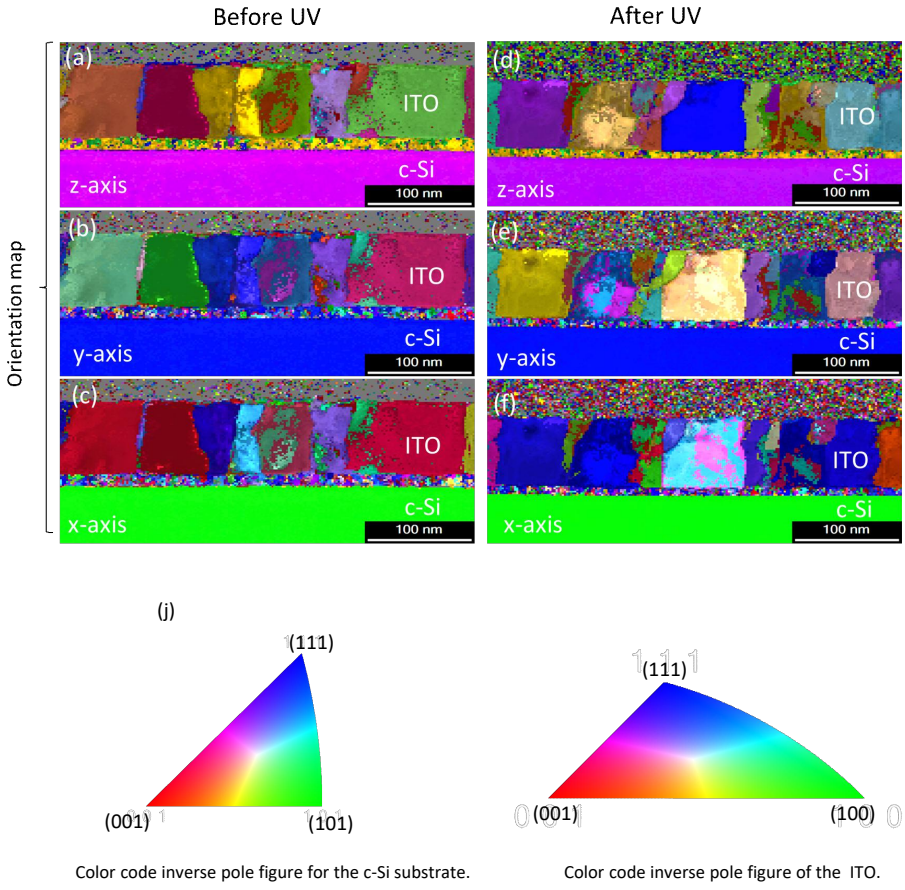

Figure 6.10: *The orientation map (a-b) for the samples before, (d-f) for the sample after UV exposure and (j) color code inverse pole figures for the Si substrate and ITO, for the large field of view (L-FOV) scanning area is* $400nm \times 200nm$ *with a pixel size of 2 nm.*

However, **Figure 6.11 (d-f)** presents the orientation map of the sample after UV exposure. There is a uniform distribution of nanocrystals of a few nanometers in the direction parallel to the interface. In the orientation map images, a more uniform single color means strong orientation alignment, while a mixture of many colors may indicates an artifactes or polycrystalline region.

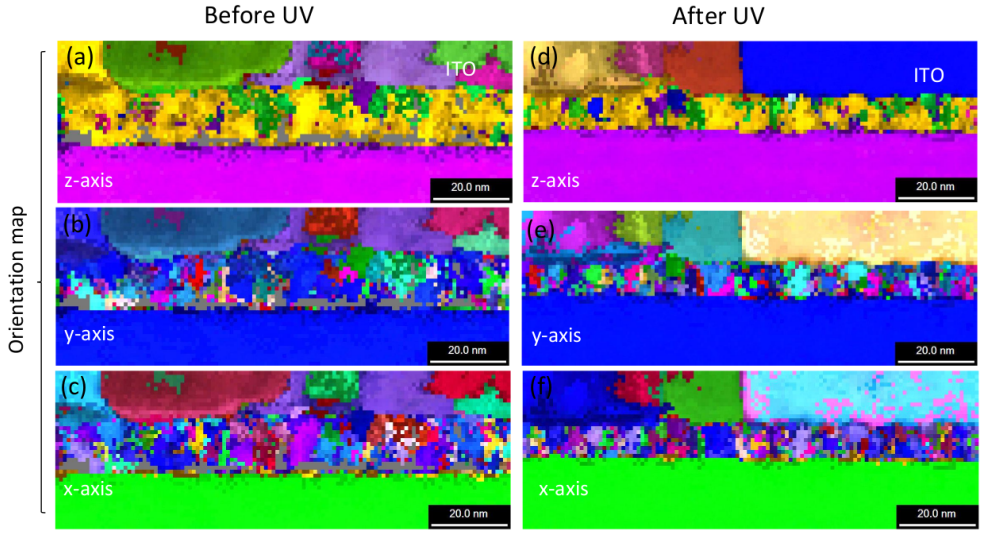

Figure 6.11: *The orientation map (a-b) for the samples before and (d-f) for the sample after UV exposure. The scanning area is* $120nm \times 40nm$ *with a pixel size of 1 nm.*

Forexample, as in the **Figure 6.11 (a-c)** the TPC stack contains many tiny colored pixels, which reflecting small nanocrystals with random orientation and a mix of crystalline and amorphous regions. However, the grains are poorly defined, consistent with nanocrystalline SiC embedded in an amorphous matrix. In the second hand, **Figure 6.11 (d-f)** shows more color fragmentation which is means increased misorientation and local orientation distortions. This suggests that UV-induced bond breaking the (Si–H, C–H), creation of new defects or perhapes internal stress causing grain rotation or misalignment.

In the reconstructed orientation maps, a notable fraction of the nanocrystals within the TPC stack display blue nanogranis contrast, corresponding to the <100> directionas in **Figure 6.10 (j)**, Since the SiC phase present in the nc-SiC:H layers is predominantly 3C-SiC (β-SiC), which has a zincblende cubic structure. The <111> orientation has the lowest surface energy and is frequently reported as the preferred growth direction in SiC thin films

formed on Si substrates. The identification of (111) oriented grains also provides insight into how UV exposure may modify the nanostructure. Any change in the distribution, continuity, or size of these grains especially if the (111) oriented domains are disrupted could impact carrier transport or passivation quality at the TPC/c-Si interface.

From the grain orientation maps in **Figure 6.10** and **Figure 6.11**, it is evident that there is a uniform distribution of nanocrystals of a few nanometers in the direction parallel to the interface. This suggests that UV-induced localized structural rearrangements are believed to contribute to the increased resistivity of nc-SiC:H, leading to the observed loss of FF.

6.5 Conclusion

This study demonstrates that UVID has a profound impact on the performance and microstructure of SHJ solar cells employing TPCs. Both conventional a-Si:H-based SHJ cells and nc-SiC:H based TPC cells suffer performance losses under UV irradiation. After UV exposure at a dose of 60 kWh m^{-2}, the TPC-based cells exhibited significant reductions in V_{OC}, J_{SC}, and FF, each relatively decreasing by more than 10%. The combination of TEM, 4D-STEM, and EDX analyses reveals that these electrical losses originate from UV-induced structural changes within the nc-SiC:H layers rather than from large-scale elemental diffusion or chemical reconfiguration at the interfaces. UVID promotes the formation of additional nanocrystalline regions, increases structural disorder, and alters diffraction signatures within the nc-SiC:H layers. These local rearrangements are consistent with hydrogen depletion and bond reconfiguration processes known to occur in wide-bandgap passivation materials. Such microstructural evolution likely raises the resistivity of the contact layers and enhances interface defect density, thereby explaining the pronounced FF and V_{OC} reductions observed in TPC devices.

Overall, the results highlight that although TPCs provide high transparency and strong passivation in their initial state, their stability under UV illumination remains a major challenge. Understanding and controlling the microstructural responses of nc-SiC:H to UV exposure will be essential for improving the long-term reliability of TPC-based SHJ technology and for ensuring its competitiveness with established high-efficiency contact schemes.

7 Conclusions and future work

This thesis advanced the understanding of SHJ solar cells by investigating three key aspects that critically influence their performance and stability: the microstructure of TCOs, the role of TPCs, and the mechanisms of UVID.

7.1 Conclusions

Solar cells play a vital role in supporting a global shift from fossil fuels to renewable energy sources. However, a significant contribution from PV can only be achieved if the costs of PV systems are reduced to a minimum. A key driver for reducing the levelized costs of electricity for PV systems is the solar energy conversion efficiency (η) of individual solar cells. Here, Si solar cells based on SHJ technology are advancing to become the highest η technology due to their superior V_{oc}.

Recent record efficiencies in the field of c-Si solar cells are exclusively shown by full area passivated contact approaches. When c-Si solar cells using passivated contacts in the full area are compared to local direct metal contacts, fully passivated contact solar cells give rise to higher V_{oc}, and consequently higher cell efficiencies are possible. The SHJ using a-Si is one of the passivated contact concepts to improve the transport of photogenerated charge carriers in the lateral direction and reduce resistive losses. Highly doped TCO layers are integral components of SHJ solar cells.

Here, the main question is how to improve the materials and thus the performance of the solar cells. In order to answer this question, we need to improve AZO film performance by adopting a seed layer of ITO. We employ the TEM characterization to determine the microstructure link with the electrical and performance of the conventional SHJ structure with AZO only, and with the structure after adding the ITO seed layer. The second topic is about TPC for the front side of SHJ solar cells, which consists of an n-type doped hydrogenated nanocrystalline silicon carbide (nc-SiC:H(n)) layer on an ultra-thin SiO_2.

The advantage of the TPC is that nc-SiC:H(n) has a wide optical band gap of 2.0 – 3.3 eV, which is larger as the band gaps of a-Si (1.7 eV) and poly-Si (1.1 eV), thus reducing the parasitic absorption. This thesis also shows that the extent of UVID in SHJ solar cells depends on the specific front (illumination side) passivating contacts used in the cell structure. Despite the obvious enhancement of J_{SC} when the nc-SiC:H based TPC contact is adopted, this investigation has found that this kind of contact is much less stable compared to its conventional a-Si:H based contact. After UV exposure at a dose of 60 kWh m^{-2}, the TPC-based cells exhibited significant reductions in V_{OC}, J_{SC}, and FF, each relatively decreasing by more than 10%. Furthermore, the electrical characterizations indicate that the J_{SC} loss is mainly due to the front surface recombination, and the FF drop results from the substantial increase in the resistivity of the nc-SiC:H layer.

For all topics, TEM was employed to investigate the microstructural features of the solar cells, with complementary compositional analysis performed using energy-dispersive EDX. Furthermore, 4D-STEM was utilized to extract crystallographic information, including grain orientation, phase reliability, and growth direction. By combining these microstructural and crystallographic insights with J–V measurements and electrical property analysis, a comprehensive correlation between structural changes and device performance was established.

The main findings can be summarized as follows:

- Correlation between structure and performance: A TEM-based approach was developed to study the microstructure of AZO thin films. Using high-resolution TEM, analytical TEM, and 4D-STEM, grain orientation and size were mapped with high precision. It was found that AZO deposited on amorphous silicon (a-Si:H) formed columnar grains that enhanced carrier transport, while AZO on nanocrystalline silicon (nc-Si:H) exhibited smaller and irregular grains, limiting mobility. An ITO seed layer promoted larger grain growth and improved crystallinity, leading to enhanced conductivity and higher device efficiencies. These results demonstrated the critical influence of microstructure and interfacial quality on the electronic performance of SHJ devices.
- TPC principle: While nc-SiC:H-based TPCs increased J_{SC} compared to conventional a-Si:H contacts, they were found to be less stable under operation. Structural and electrical characterization revealed that performance gains came at the expense of reduced long-term reliability, highlighting the delicate balance between electrical en-

hancement and stability.

- Degradation behavior: It was shown that the extent of UVID strongly depends on the front passivating contact design. Under UV exposure, nc-SiC:H-based contacts exhibited significant reductions in V_{OC}, J_{SC}, and FF. To identify the structural origins of these losses, TEM, 4D-STEM and EDX analyses were performed before and after degradation. High-resolution TEM imaging revealed increased lattice disorder, interface roughening, and local amorphization within the nc-SiC:H layers after UV exposure. 4D-STEM orientation mapping showed a broader spread of local grain orientations and the formation of small, disordered regions, indicating UV-induced structural rearrangements that hinder carrier transport. Complementary EDX mapping detected subtle variations in oxygen, silicon, and carbon signals near the nc-SiC:H layers and SiO_x/c-Si interfaces, consistent with Si–H bond rupture, hydrogen migration, and defect formation. These microstructural and chemical changes explain the increased recombination and resistive losses observed electrically. In contrast, conventional a-Si:H contacts showed significantly fewer structural modifications, correlating with their superior stability under UVID.

Together, these results provide a comprehensive picture of how microstructure, contact design and electrical properties interact to determine SHJ solar cell performance. TEM, and in particular 4D-STEM, proved to be indispensable in correlating nanoscale structural features with macroscopic photovoltaic behavior.

7.2 Future work

While this work has demonstrated the value of TEM-based analysis for advancing high-efficiency SHJ solar cells, several directions remain open for future investigation. Further progress could be achieved by expanding the use of advanced TEM techniques such as STEM, high-resolution TEM, and EELS to gain deeper insight into interfacial chemistry, bonding, and defect states. Improving TEM sample preparation especially for full device cross-sections—through refined FIB and other low-damage approaches will be essential for reliable nanoscale characterization. Integrating these nanoscale insights with scalable deposition process optimization and device-level modeling could support the rational design of improved passivation and TCO layers. Finally, the characterization framework established in this thesis can be extended beyond SHJ devices to emerging tandem and

next-generation photovoltaic architectures, where interfacial quality remains a critical determinant of performance. Together, these research directions highlight the continued importance of nanoscale structural analysis in pushing photovoltaic devices toward higher efficiency, improved stability, and long-term technological viability.

List of Abbreviations

This chapter lists all acronyms used in this thesis.

PV	Photovoltaic
c-Si	Crystalline Silicon
SHJ	Silicon Heterojunction
η	conversion efficiency
a-Si	amorphous silicon
a-Si:H	Hydrogenated Amorphous Silicon
TCO	Transparent Conductive Oxides
AZO	Aluminum-doped Zinc Oxide
ITO	Indium Tin Oxide
TPC	Transparent Passivating Contacts
nc-SiC:H	NanoCrystalline Silicon Carbide
TEM	Transmission Electron Microscopy
4D-STEM	4D Scanning Transmission Electron Microscopy
EDX	Energy Dispersive X-ray
HRSTEM	High resolution scanning TEM
UVID	UltraViolet-Induced Degradation
E_g	bandgap energy
E_v	valence band
E_c	conduction band
λ	wavelengths
SQ	Shockley-Queisser
SHR	Shockley-Read-Hall
J_{SC}	Short-circuit current density
V_{OC}	Open-circuit voltage
FF	Fill factor
MPP	maximum power point

a-Si:H/poly-Si	silicon heterojunction
i-a-Si:H	intrinsic hydrogenated amorphous silicon
KOH	alkaline potassium hydroxide
SEM	Scanning electron microscope
DB	dangling bonds
TPCs	transparent passivating contacts
ZnO:Al_2O_3	aluminium-doped zinc oxide
In_2O_3:SnO_2	Indium tin oxide
ZnO	zinc oxide
Al	aluminum
B	boron
Ga	gallium
XRD	x-ray diffraction
In	indium
O	oxygen
Sn	substitute tin
SnO_2	tin oxide
CVD	chemical vapour deposition
HWCVD	Hot wire chemical vapour deposition
MMS	monomethylsilane
STEM	scanning transmission electron microscopy
EELS	electron energy loss spectroscopy
APT	Atom probe tomography
SIMS	Secondary Ion Mass Spectrometry
ToF-SIMS	time-of-flight SIMS
EM	electron microscope
$\delta f = C_1$	Defocus
C_s	spherical aberration
C_c	chromatic aberration
W	tungsten
LaB6	lanthanum hexaboride
FEG	field emission gun
SE	secondary electrons
BSE	backscattered electrons

BF	bright field
DF	dark field
HRTEM	High resolution TEM
β	scatter collection angle
LAADF or ADF	Low-angle annular dark-field
ABF or BF	Annular bright field
CBED	convergent beam electron diffraction
NBED	nanobeam electron diffraction
SEND	scanning electron nano-diffraction
ROI	region of interest
EBSD	electron backscatter diffraction
FEG	field emission gun
PED	precession electron diffraction
AEM	Analytical Electron Microscopy
SDD	silicon-drift detector
EELS	Electron energy loss spectroscopy
ZLP	zero-loss peak
ELNES	energy-loss near-edge structure
FIB	focused ion beam
PIPS	precision ion polishing system
EQE	external quantum efficiency
IQE	internal quantum efficiency
SHJ	silicon heterojunction
IWO	Tungsten doped indium oxide
ITiO	titanium-doped indium oxide
IZrO	indium zirconium oxide
ICO:H	hydrogenated indium cerium oxide
FFT	Fast Fourier transform
HAADF	high annular dark-field
UV	Ultraviolet
TOPCon	tunnel oxide passivated contact
POLO	poly-Si on oxide
SiC	Silicon carbide
SiO_2	silicon oxide

HWCVD	hot-wire chemical vapor deposition
L-FOV	large field of view
S-FOV	small field of view
BF-STEM	bright-field scanning transmission electron microscopy

Appendix

Table 1: *Table A1*

Samples No.	Name	Materials	Type of sample
#200	222vxe-4	AZO/ aSi:H/c-Si	FIB
#201	22tmg9-4	AZO-ncSi:H/c-Si	FIB
#202	22tmg9-1	ITO/ncSi:H/c-Si	FIB
#203	21u436	AZO/aSi:H/c-Si	FIB
#204	21gwf9	AZO/ITO/aSi:H/c-Si	Conventional
#217	23g1uh-2	AZO-ncSi (no H2)	FIB
#218	234vvf-1	AZO-ncSi (no H2)	FIB
#230	21753f-1	AZO/ITO/c-Si	
#236	232rbf-2	ITO/SiC/c-Si	Conventional
#237	23c3sw-2	ITO/SiC/c-Si	Conventional
#253	TPC-UV	ITO/SiC/c-Si	Conventional
#254	SHJ TPC	ITO/SiC/c-Si	Conventional
#271	SHJ AZO/ITO	AZO/ITO/c-Si	FIB
#273	231tuc-1 TPC-UV	ITO/SiC/c-Si	
#274	23x5xd-3 TPC reference	ITO/SiC/c-Si	
#275	23qvx5 RF AZO/a-Si	AZO/c-Si	FIB
#276	23qwm7 DC AZO/a-Si	AZO/c-Si	FIB

List of Figures

1.1 Schematic representation illustrating the correlation between nanostructural properties, electrical/optical characteristics, and overall device performance in a solar cell. 14

2.1 Functional diagram of a photovoltaic solar cell with an external circuit component. 18

2.2 The energy band diagram of the p-n junction. 19

2.3 Theoretical efficiency limits of single-junction solar cells as a function of the semiconductor bandgap. Adapted from [22]. 20

2.4 Recombination mechanisms in semiconductors. The black arrows indicate the direction of the electron (brown circuit with minus sign) transitions. The holes (blue circle with plus sign) travel against the arrow direction. (a) depicts the schematic of spontaneous radiative recombination, (b) depicts the Auger recombination processes, (c) shows the four basic transitions that may occur during SRH recombination. 22

2.5 Current density-voltage ($J-V$) curve of a solar cell and the parameters that can be evaluated: short-circuit current density J_{sc}, open-circuit voltage V_{oc}, current density and voltage at the maximum power point (MPP). . . 24

2.6 Structure of silicon heterojunction solar cells built on pyramidal-textured n-type c-Si wafers and an intrinsic thin layer. 25

2.7 Etched of silicon oriented along the (100) plane and textured along the (111) plane (a). SEM images of the top view of the textured SHJ solar cell(b). . 27

2.8 The hexagonal wurtzitel lattice is characterized by two lattice constants: a and c in (a), crystal structure hexagonal wurtzite model of AZO (b) and cubic bixbyite ITO (c), the crystal models of AZO and ITO can be visualised using the VESTA software tools. 33

3.1 The development of microscopy resolution during the years, adapted from H. Rose [75]. 39

3.2 (a) Spherical aberration(b) Chromatic aberration (c) Astigmatism. 41

3.3 Schematic diagram of the beam formation optics in TEM vs STEM. 43

3.4 Signals were generated by the interaction of a beam of high energy electrons with a thin specimen; modified from [61]. 45

3.5 Illustrates the ray diagrams for the diffraction (left) and imaging (right) operation modes in a TEM, adapted from [61] 47

3.6 Schematic configuration of STEM detection set-up. Annular DF (ADF), Annular BF and HAAD detectors conditions (a) and (b) the relative positions of the ADF and ABF detectors. The LAADF detector (top) forms an annular region capturing scattered electrons at low angles, while the ABF detector (bottom) is more centrally positioned, capturing Bragg-scattered electrons. The corresponding images formed ADF and BF images as in (c). 49

3.7 Schematic representation of the constructive interference condition, governed by Bragg's law, where the path difference between reflected waves equals an integer multiple of the wavelength. The Ewald sphere is shown in a reciprocal space with a radius of $|k_0| = |k_g| = 1/\lambda$. The formation of a diffraction pattern is shown geometrically in real space. The vectors k_0 and k_g are the wave vectors of the incident and diffracted beam, and g is the reciprocal lattice vector; the dashed black line represents the Ewald sphere. 51

3.8 A SAED pattern obtained from a crystalline silicon substrate in [100] direction (a) and the SAED pattern displays diffraction rings characteristic of a nanocrystalline AZO/ITO thin film (b). 53

3.9 A Schematic of four-dimentional STEM (4D-STEM), Adapted with permission from Ophus (2019) [93]. 54

3.10 Schematic representation of x-ray emission. Adapted with permission from Williams and Carter(2009) [61] 56

3.11 Schematic illustration of the TEM sample mechanical preparation process for a solar cell device. (a) Preparation of the sandwich structure using Si dummy substrates with the solar cell sample placed in the center. (b) Cutting the sandwich into thin slices ($\sim$300 μm) using a wire saw. (c) Punching the slices into 3 mm diameter standard disks. (d) Initial polishing and grinding of the disks down to $\sim$100 μm thickness using silicon carbide abrasive paper. (e) Dimple grinding and polishing to achieve $< 50 \mu m$ thickness at the center. (f) Final thinning by argon ion milling to obtain an electron-transparent region (< 50 nm) suitable for TEM analysis. 59

3.12 Equipment used in the conventional TEM samples. 61

3.13 SEM images illustrating the focused ion beam (FIB) technique steps. For detailed explanation of individual steps see text. 62

3.14 Schematic illustration of a dual beam FIB/SEM (left). The angle (α) between the electron beam and ion beam is normally in the range of 52 and 54° the FEI nanolab 460F1 scanning electron microscope (right). 63

3.15 Silicon heterojunction solar cells built on pyramidal-textured c-Si wafers (a), The main steps of the manufacturing process of the SHJ(b). 66

3.16 Sketch of a silicon solar cell using an n-type wafer with a TPC on the front side (a), The main steps of the manufacturing process of the TPC (b). . . 68

4.1 Schematic overview of the key considerations prior to TEM specimen preparation, growth mechanisms, motivation for the structure and materials, and crystallographic orientation of the structure. 74

4.2 Optical microscope images of the TEM sample at grinding stages. During initial polishing, surface roughness and scratches are visible, along with debris (indicated by yellow arrows) (a). After grinding, the surface appears smoother and more uniform, with a significant reduction in polishing defects, resulting in a sample better suited for subsequent thinning and TEM analysis (b). 75

4.3 Optical image of the glued sandwich structure, where the solar cell layers are embedded between dummy Si substrates for mechanical support (a). Formation of an excellent thin region during ion milling, suitable for electron transparency (b). Final stage showing hole formation at the center of the sample, indicating complete perforation (c). (d) Low-magnification TEM image showing the glue line and layer interfaces (d), intermediate thinning region exhibiting pronounced bending contours caused by strain and thickness variations (e), uniformly thinned area demonstrating suitable electron transparency but also revealing edge roughness from ion milling (f). 77
4.4 TEM image of a FIB-prepared lamella from a SHJ solar cell, showing localized amorphous damage (dark halo) caused by ion implantation and beam-induced amorphization with scale bar 20 nm. 78
4.5 TEM images showing preparation artifacts, redeposition near the ITO layer (a), residual needle material within the poly-Si layer. (b). 80

5.1 The schematic illustration of a standard n-type c-Si substrate SHJ solar cell, the window layers of three groups of SHJ cells fabricated for this study, and the zoomed-in view of the front side of Cell 1: AZO/(n/i) a-Si:H, cell 2: AZO/(n)nc-Si: H/(i)a-Si:H and cell 3: AZO/ITO/(n/i)a-Si:H. 85
5.2 The open-circuit voltage (V_{oc}) (a), short-circuit current density (J_{sc}) (b), fill factor (FF) (c), power conversion efficiency (η) of the solar cells with AZO front contacts (d). 88
5.3 (a) Resistivity and carrier concentration for the three cells in this study, and (b) Charge carrier mobility and average grain diameter. 90
5.4 Cross-section TEM images obtained from the sample cell 1 with AZO/(n/i)a-Si:H in (a), cell 2 with AZO/(n)nc-Si:H in (b) and cell 3 with AZO/ITO. All with scale bar 50nm 92
5.5 Bright field (BF) image of the side of sample cell2 AZO/(n)nc-Si:H in (a). DF image of the same sample in (b). 92
5.6 HRTEM image of sample with AZO deposited on (i/n)a-Si:H/c-Si a scale bar of 10 nm has an average grain size of 53.8 nm (b), and the corresponding FFT pattern (b). 93
5.7 HRTEM image of sample with AZO deposited on (i/n)a-Si:H/c-Si with a scale bar of 5 nm and its average grain size of 26.2 nm (a), and the corresponding FFT pattern (b). 93

5.8 HRTEM images of the structure with AZO deposited on (n)nc-Si:H/(i)a-Si:H/c-Si, with scale bars of 25 nm average grain size of 14.8 nm (a), and the corresponding FFT pattern(b). 94
5.9 EDX analysis was performed at the same position (a). HAADF-STEM image obtained at a comparable position within cell 1 (b). 95
5.10 EDX analysis was performed at the same position (a). HAADF-STEM image obtained at a comparable position within cell 2 (b). 96
5.11 HAADF STEM overview image obtained within cell 3 with scale bar 2 μm (a) HAAD-STEM image at the different scale bar 200 nm (b). 96
5.12 HAADF-STEM image obtained at a comparable position within cell 3 (a), The composite image of elemental mapping (indicated with the arrow the same as growth direction) (b), EDX analysis was performed at the same position (c), XRD pattern of the TCO film, where red indicates cell 3 and black indicates cell 1 (d), adapted from [127]. 97
5.13 (a) Virtual BF-STEM and diffraction patterns of the silicon substrate in the inlets for sample cell 1, AZO only, and the phase map image in (b). 99
5.14 (a) Virtual BF-STEM and diffraction patterns of the silicon substrate in the inlets for sample cell 2, and the phase map image in (b). 99
5.15 (a) Virtual BF-STEM and diffraction patterns of the silicon substrate in the inlets for sample cell 3, and the phase map image in (b). 100
5.16 The orientation map along the (x,y and z) direction of cells 1 from left to right. color code inverse pole figures for the Si substrate and AZO. 102
5.17 The orientation map along the (x,y and z) direction of cell 2 from left to right. color code inverse pole figures for the Si substrate and AZO. 102
5.18 The orientation map along the (x,y and z) direction of cell 3 from left to right. color code inverse pole figures for the Si substrate and AZO. 103
5.19 (a, b, and c) Grain boundary annotation layer for cell 1 with AZO/a-Si: H, cell2 with AZO/nc-Si:H, and cell3 with AZO/ITO, respectively; (d, e, and f) Statistical analysis of grain size distribution. 104
5.20 (a) Diagram sputtering process, explaining the difference between the types of power [158]. (b) Schematic illustration of the SHJ solar cell layers, the inset shows an atomic-scale view of the a-Si:H/c-Si interface, highlighting the structural disorder and hydrogen passivation with red atom within the a-Si:H layer [158–160]. 106

5.21 The evolution of (a)open-circuit voltage (V_{oc}),(b) short-circuit current density (J_{sc}), (c) fill factor (FF), and (d) efficiency (η) of silicon heterojunction solar cells. 109
5.22 TEM images showing sputter damage caused by (a) PDC and (b) RF sputtering methods, along with (c) a reference a-Si sample without any ITO coating (free from sputter damage), adapted by [167]. 110

6.1 Bright-field (BF) (a), dark-field TEM image (DF) (b), and electron diffraction pattern (c) of a μc-SiC:H film with a relative doping level of 0.001. The film exhibits a columnar arrangement of crystalline grains. The diffraction pattern confirms the predominance of the cubic phase, while the arc-shaped intensity along the (111) ring indicates a preferred orientation of the (111) planes perpendicular to the film growth direction [172]. 114
6.2 (a) The schematic illustration of a standard n-type c-Si substrate SHJ solar cell used TPC on the front side, using stack layers ITO, nc-SiC:H pass. represents the passivation layer, whereas nc-SiC:H cond represents the conductive layer and SiO_2. (b) HRSTEM bright-field image and EDX measurement of the c-Si(n)/SiO_2/nc-SiC:H(n) interface. The arrow is to show the SiC crystallites embedded in an amorphous matrix. The EDX line profile is obtained at a similar location, which clearly shows the oxygen presence at the interface to the silicon substrate, scale bar, 5 nm [14]. 115
6.3 (a)Scanning electron microscope (SEM) image of the thinned lamella for samples before UV exposure and with UV exposure, respectively (a and b), surface of the thin film showing the pyramids of the texture for the samples before UV exposure and with UV exposure, respectively (c and d). 118
6.4 The evolution of (a) efficiency, (b) short-circuit current density, (c) fill factor, and (d) open-circuit voltage of silicon heterojunction solar cells using (i) a-Si:H based SHJ contact or nc-SiC:H based TPC contact after a UV irradiation with the UV dose of 60 kWh m^{-2}. 120
6.5 Cross sectional TEM images of ITO/TPC stack/c-Si samples and the corresponding FFT pattern inset for the samples before UV exposure in (a) and after UV exposure in (b). 122
6.6 High annular dark-field (HAADF) STEM overview images obtained before UV exposure and after UV exposure (a and b) respectively, with scale bar $200nm$. 122

6.7 EDX elemental maps of the ITO/TPC stack/c-Si interface before (a) and after (b) UV exposure. Elemental distributions of In, Sn, C, O, and Si are shown to evaluate potential chemical changes induced by ultraviolet illumination. 123
6.8 Virtual bright-field STEM images of ITO/TPC stack/c-Si samples before UV exposure in (a) and sample after UV exposure in (b). Phase reliability for samples before and after UV exposure in (c) and (d), respectively. The scanning area is $400nm \times 200nm$ with a pixel size of 2 nm. 125
6.9 Virtual bright-field STEM images of ITO/nc-SiC:H/SiO_x/c-Si samples before UV exposure in (a) and sample after UV exposure in (b). Phase reliability for samples before and after UV exposure in (c) and (d), respectively. The scanning area is $120nm \times 40nm$ with a pixel size of 1 nm. 126
6.10 The orientation map (a-b) for the samples before, (d-f) for the sample after UV exposure and (j) color code inverse pole figures for the Si substrate and ITO, for the large field of view (L-FOV) scanning area is $400nm \times 200nm$ with a pixel size of 2 nm. 127
6.11 The orientation map (a-b) for the samples before and (d-f) for the sample after UV exposure. The scanning area is $120nm \times 40nm$ with a pixel size of 1 nm. 128

List of Tables

2.1 Values of the band gap and crystal lattice parameters of Si, AZO, ITO and nc-SiC. 33
2.1 Values of the band gap and crystal lattice parameters of Si, AZO, ITO and nc-SiC. 34

3.1 Electron wavelengths at 5, 10, 200, and 300 KV, and light wavelength. . . 40
3.2 highlighting key differences and similarities between EBSD, NBED, and 4D-STEM when used for orientation mapping. 55
3.3 Summary of layer, thickness, and deposition techniques for the solar cell structure. 65

5.1 Summary of the performance of AZO-related SHJ solar cells, adapted by [127]. 91

6.1 Overview of the samples investigated in this study and their performance parameters. 117

1 Table A1 139

Acknowledgments

I would like to express my sincere gratitude to all those who made this work possible. I am deeply indebted to my supervisor Prof. Joachim Mayer for his supervision, for examining this thesis, and for providing me with the opportunity to conduct my research at his institute. I am equally grateful to my second supervisor Prof. Uwe Rau for his supervision, examination, and for his continuous confidence and encouragement throughout my doctoral studies. I am also indebted to many colleagues at the Ernst Ruska Centre for Microscopy and Spectroscopy with Electrons (ERC) who contributed by preparing samples, assisting me in preparing my own samples, performing measurements, or providing support in analysis. My sincere thanks to Dr. Hongchu Du and Dr. Martina Luysberg for providing me training on the microscope.

My special thanks go also to the Photovoltaic group in the Institute of Energy Materials and Devices (IMD), to Dr. Kaining Ding, whose excellent guidance and support were invaluable at every stage of this work. I am thankful also to Alexander Eberst and all colleagues in the group for discussions time and fascinating work.

I gratefully acknowledge the organisers of the Palestinian-German Science Bridge (PGSB) for offering me the unique opportunity to complete my PhD in Germany.

On a personal note, I wish to thank my beloved husband, Soboh, for his endless support, patience, and understanding throughout this journey. Finally, I am profoundly grateful to my family, whose unwavering encouragement and strong foundation in education have brought me to where I am today.

Publications related to this thesis

- Alkhereibi, S., Yaqin, M. A., Eberst, A., Xu, B., Jo, J., Alsamamra, H., Lambertz, A., Rau, U., Ding, K., Mayer, J. (2025). Resolving the microstructure of aluminum-doped zinc oxide thin films grown on different silicon heterojunction solar cell structures by advanced transmission electron microscopy. Thin Solid Films, 825, 140744. https://doi.org/10.1016/j.tsf.2025.140744
- Binbin Xu, Sara Alkhereibi, Alexander Eberst, Kai Zhang, Rongda Zhang, Astrid Besmehn, Felix Gunkel, Tae-Eun Hong, Joon-ho Oh, Karsten Bittkau, Andreas Lambertz, Joachim Mayer, Uwe Rau, Kaining Ding. Passivating Contacts-related Ultraviolet-induced Degradation in Silicon Heterojunction Solar Cells "Shared first author". Small Structures. https://doi.org/10.1002/sstr.202600024

Curriculum Vitae

About

PhD Research Fellow (2021–2025) at RWTH Aachen University and Forschungszentrum Jülich, specializing in the fundamental properties and microstructural characterization of high-efficiency solar cells through advanced microscopy techniques. Possesses extensive experience in theoretical and applied physics, with a Master's in Theoretical Physics focusing on quantum-classical analogies for ballistic electrons and electromagnetic waves. Previously served as a teaching assistant and educator, delivering courses in physics and general science, developing educational materials, and supervising research. Actively contributed to astronomical research initiatives, including the establishment of observatories and exhibitions. Author of multiple peer-reviewed publications on topics ranging from quantum electron propagation to advanced transmission electron microscopy of photovoltaic materials.

Education

- **2021–2025:** Ph.D. in Photovoltaics Physics, RWTH Aachen University & Forschungszentrum Jülich, Germany. Thesis: *The fundamental properties and microstructural characterization of high-efficiency solar cells.*
- **2017–2019:** M.Sc. in Theoretical Physics and Applied Mathematics, Islamic University, Gaza, Palestine. Thesis: *Analogies between Quantum and Classical for the Propagation of Ballistic Electrons and Electromagnetic Waves.*
- **2010–2014:** B.Sc. in Physics Teaching Education, Al Aqsa University, Gaza, Palestine.
- **2009–2010:** High School (Scientific Stream), Khanyounis School for Girls, Gaza, Palestine.

Career Summary

- **PhD Research Fellow (2021–2025)** — RWTH Aachen University & Forschungszentrum Jülich, Jülich, Germany. Research at the Ernst Ruska-Centre for Microscopy and Spectroscopy with Electrons, focusing on the microstructural characterization of high-efficiency solar cells. Expertise in advanced microscopy and photovoltaics physics.
- **Teaching Assistant (2015–2016)** — Al Aqsa University, Physics Department, Gaza, Palestine. Developed and evaluated exams; taught General Physics A; supervised research and supported laboratory work.
- **Science Teacher (2014–2015)** — UNRWA, Gaza, Palestine. Taught science to grades IV–VIII; developed teaching methods; organized scientific trips and competitions.
- **Physics Teacher (2016–2017)** — Islamic Awqaf Secondary School, Gaza, Palestine. Taught high school physics and mentored students.
- **Research Assistant (Volunteer, 2018–2019)** — CASSR – Center of Astronomy and Space Sciences Research, Al Aqsa University, Gaza, Palestine. Coordinated astronomy-related projects including observatory establishment, study days, and exhibitions.

Publications

- Binbin Xu and Sara Alkhereibi et al. (2026). *Passivating Contacts-related Ultraviolet-induced Degradation in Silicon Heterojunction Solar Cells "Shared first author".* Small Structures. https://doi.org/10.1002/sstr.202600024
- Sara Alkhereibi et al. (2025). *Resolving the Microstructure of Azo Thin Films Grown on Different Silicon Heterojunction Solar Cell Structures by Advanced Transmission Electron Microscopy.* `https://doi.org/10.1016/j.tsf.2025.140744`
- Sara Alkhereibi et al. (2020). *Theoretical Study of Propagation of Ballistic Electrons through Multilayered Structure.* `10.1109/ICPET51420.2020.00031`
- Sara Alkhereibi et al. (2019). *Analogies between Quantum and Classical for the Propagation of Ballistic Electrons and Electromagnetic Waves.*
- Sara Alkhereibi et al. (2019). *Transmission and Reflection of Negative Mass Ballistic*

Electron through a Single Finite Quantum Barrier.

Communications

- 3–5 February 2025: Resolving the Microstructure of Azo Thin Films. Workshop on New Perspectives in Solid-State and Material Research, Max-Planck Institute, Stuttgart.
- 11 December 2024: Microstructural and Functionality of Heterojunction Contact on Crystalline Silicon Solar Cell, PGSB Workshop, Forschungszentrum Jülich.
- 14–18 July 2019: Palestinian Advanced Physics School, Scientists for Palestine, Birzeit University.
- 5 March–30 April 2019: Training Course for Summer Camp Leaders and Activists (15 hours).
- March 2017: Member, First Astronomical Exhibition in Palestine, Islamic University, Gaza.
- 11 March 2017: Academic Day – Developing the Performance of Graduate Students.
- 22–26 April 2017: Second Scientific Research Week, Islamic University, Gaza.
- 2017: Physicist Conference – *Physics For All 3: Computational Celestial Mechanics.*

Courses

- Condensed Matter Physics I (2023)

Skills

- Scientific writing, data analysis, statistical modeling, microscopy, photovoltaics, and research methodologies.
- Programming: Python, MATLAB, LaTeX, Microsoft Office, Google Workspace.
- Data visualization, analytics, and processing tools.
- Strong communication, planning, and teamwork skills.

Languages

- **Arabic:** Native
- **English:** B2 – Advanced

- **German:** A2-B1 – Basic proficiency

References

- Prof. Dr. rer. Nat. Joachim Mayer — RWTH Aachen University, Gemeinschaftslabor für Elektronenmikroskopie, Ahornstraße 55, 52074 Aachen. mayer@gfe.rwth-aachen.de
- Prof. Dr. rer. Nat. Uwe Rau — Forschungszentrum Jülich GmbH, JARA-Energy, RWTH Aachen University, Schinkelstr. 2, 52062 Aachen. u.rau@fz-juelich.de
- Dr. rer. Nat. Kaining Ding — Forschungszentrum Jülich GmbH, Institute for Energy Materials and Devices, 52425 Jülich, Germany. k.ding@fz-juelich.de

References

[1] A. Hooke, The Global Demand for Energy – 2020-2100, Accessed: 2025-10-03, **2023**.

[2] B. Dudley, BP Statistical Review of World Energy 2019, Report, BP p.l.c., London, **2019**.

[3] Fraunhofer Institute for Solar Energy Systems ISE, Photovoltaics Report, tech. rep., Updated: 30 July 2024, Fraunhofer ISE, **2024**.

[4] United Nations, Paris Agreement, Report, United Nations, New York, **2016**.

[5] I. E. Agency, Global Energy Review 2020, Accessed: 2025-10-03, **2020**.

[6] I. E. Agency, Global Energy Review 2025, Accessed: 2025-10-03, **2020**.

[7] I. E. Agency, Global Energy Review 2024, Accessed: 2025-10-03, **2020**.

[8] V. Shah, J. Booream-Phelps, S. Min, 2014 Outlook: Let the Second Gold Rush Begin, Report, Deutsche Bank Markets Research, **2014**.

[9] International Technology Roadmap for Photovoltaics, 2023 Results, Report, ITRPV, **2024**.

[10] S. De Wolf, A. Descoeudres, Z. C. Holman, C. Ballif, *Green* **2012**, *2*, 7–24.

[11] H. Lin, M. Yang, X. Ru, G. Wang, S. Yin, F. Peng, C. Hong, M. Qu, J. Lu, L. Fang, C. Han, P. Procel, O. Isabella, P. Gao, Z. Li, X. Xu, *Nature Energy* **2023**, *8*, 789–799.

[12] K. Ellmer, *Nature Photonics* **2012**, *6*, 809–817.

[13] S. Li, M. Pomaska, A. Lambertz, W. Duan, K. Bittkau, D. Qiu, Z. Yao, M. Luysberg, P. Steuter, M. Köhler, K. Qiu, R. Hong, H. Shen, F. Finger, T. Kirchartz, U. Rau, K. Ding, *Joule* **2021**, *5*, 1535–1547.

[14] M. Kohler, M. Pomaska, P. Procel, R. Santbergen, A. Zamchiy, B. Macco, A. Lambertz, W. Duan, P. Cao, B. Klingebiel, S. Li, A. Eberst, M. Luysberg, K. Qiu, O. Isabella, F. Finger, T. Kirchartz, U. Rau, K. Ding, *Nature Energy* **2021**, *6*, DOI: 10.1038/s41560-021-00806-9, 529–537.

[15] S. Kim, V. Q. Hoang, C. W. Bark, *Nanomaterials* **2021**, *11*, 2944.

[16] S. Arya, P. Mahajan in *Solar Cells: Types and Applications*, Springer Nature Singapore, Singapore, **2023**, pp. 37–76.

[17] T. Markvart, *Solar cells: materials, manufacture and operation*, Academic Press, **2012**.

[18] Y. Abou Jieb, E. Hossain, *Photovoltaic Systems: Fundamentals and Applications*, Springer International Publishing, Cham, **2022**.

[19] N. Guerra, M. Guevara, C. Palacios, F. Crupi, *I+D Tecnológico* **2018**, *14*, 84–95.

[20] M. A. Green, K. Emery, Y. Hishikawa, W. Warta, E. D. Dunlop, *Progress in Photovoltaics: Research and Applications* **2015**, *23*, 1–9.

[21] K. Yoshikawa, H. Kawasaki, W. Yoshida, T. Irie, K. Konishi, K. Nakano, T. Uto, D. Adachi, M. Kanematsu, H. Uzu, K. Yamamoto, *Nature Energy* **2017**, *2*, 17032.

[22] T. Markvart, *WIREs Energy and Environment* **2016**, *5*, 543–569.

[23] W. Shockley, H. J. Queisser, *Journal of Applied Physics* **1961**, *32*, 510–519.

[24] M. Yamaguchi, F. Dimroth, J. F. Geisz, N. J. Ekins-Daukes, *Journal of Applied Physics* **2021**, *129*, 240901.

[25] T. Kirchartz, G. Yan, Y. Yuan, B. Patel, D. Cahen, P. Nayak, *Nature Reviews Materials* **2025**, Publisher Copyright: © Springer Nature Limited 2025., DOI 10.1038/s41578-025-00784-4.

[26] M. Plakhotnyuk, Nanostructured Heterojunction Crystalline Silicon Solar Cells with Transition Metal Oxide Carrier Selective Contacts, https://doi.org/10.13140/RG.2.2.15200.17929, **2018**.

[27] A. Richter, M. Hermle, S. W. Glunz, *IEEE Journal of Photovoltaics* **2013**, *3*, 1184–1191.

[28] Y. Hamakawa, K. Fujimoto, K. Okuda, Y. Kashima, S. Nonomura, H. Okamoto, *Applied Physics Letters* **1983**, *43*, 644–646.

[29] W. G. J. H. M. Van Sark, F. Roca, L. Korte, *Physics and Technology of Amorphous-Crystalline Heterostructure Silicon Solar Cells*, Springer, **2012**.

[30] M. Taguchi, A. Yano, S. Tohoda, K. Matsuyama, Y. Nakamura, T. Nishiwaki, K. Fujita, E. Maruyama, *IEEE Journal of Photovoltaics* **2014**, *4*, 96–99.

[31] R. A. D. Arancon, C. S. K. Lin, K. M. Chan, T. H. Kwan, R. Luque, *Energy Science & Engineering* **2013**, *1*, 53–71.

[32] J. Du, F. Meng, H. Fu, L. Sun, L. Zhang, A. Han, J. Shi, Y. Xie, Z. Liu, *Energy Science & Engineering* **2021**, *9*, 1306–1312.

[33] J. Puigdollers, C. Voz, E. Ros in *Energy Harvesting and Storage: Fundamentals and Materials*, Springer Nature Singapore, Singapore, **2022**, pp. 61–95.

[34] Y. Liu, Y. Li, Y. Wu, G. Yang, L. Mazzarella, P. Procel-Moya, A. C. Tamboli, K. Weber, M. Boccard, O. Isabella, X. Yang, B. Sun, *Materials Science and Engineering: R: Reports* **2020**, *142*, 100579.

[35] S. de Wolf, C. Ballif, M. Kondo, *Physical Review B* **2012**, *85*, 113302–113306.

[36] Q. Yang, K. Bittkau, A. Eberst, U. Rau, K. Ding, *Solar Energy Materials and Solar Cells* **2024**, *273*, 112953.

[37] C. Messmer, M. Bivour, C. Luderer, L. Tutsch, J. Schön, M. Hermle, *IEEE Journal of Photovoltaics* **2020**, *10*, 343–350.

[38] H. T. Gebrewold, K. Bittkau, K. Qiu, U. Rau, K. Ding, *Solar RRL* **2023**, *7*, 2201051.

[39] E. Fortunato, D. Ginley, H. Hosono, D. C. Paine, *MRS Bulletin* **2007**, *32*, 242–247.

[40] K. Ellmer, *Journal of Physics D: Applied Physics* **2001**, *34*, 3097–3108.

[41] K. Ellmer, R. Mientus, *Thin Solid Films* **2008**, 6th International Conference on Coatings on Glass and Plastics (ICCG6), Advanced Coatings for Large, Area or High, Volume Products, 4620–4627.

[42] K. Wilken, Druckausgabe: 2017. - Onlineausgabe: 2017. - Auch veröffentlicht auf dem Publikationsserver der RWTH Aachen University; Dissertation, RWTH Aachen University, 2017, Dissertation, RWTH Aachen University, Jülich, **2017**, 1 Online–Ressource (194 Seiten).

[43] V. Coleman, C. Jagadish in *Zinc Oxide Bulk, Thin Films and Nanostructures*, (Eds.: C. Jagadish, S. Pearton), Elsevier Science Ltd, Oxford, **2006**, pp. 1–20.

[44] L. Jianguo, S. Fujita, T. Kawaharamura, H. Nishinaka, Y. Kamada, T. Ohshima, Z. Ye, Y. Zeng, Y. Zhang, L. Zhu, H. He, B. Zhao, *Journal of Applied Physics* **2007**, *101*, DOI 10.1063/1.2721374.

[45] *Handbook of Transparent Conductors*, (Ed.: D. S. Ginley), Springer US, Boston, MA, **2011**.

[46] D. Erfurt, *New TCO for use as transparent front contact in chalcopyrite thin film solar cells*, Technische Universitaet Berlin (Germany), **2019**.

[47] D. K. Sharma, S. Shukla, K. K. Sharma, V. Kumar, *Materials Today: Proceedings* **2022**, *49*, National Conference on Functional Materials: Emerging Technologies and Applications in Materials Science, 3028–3035.

[48] V. Coleman, C. Jagadish in *Zinc Oxide Bulk, Thin Films and Nanostructures*, (Eds.: C. Jagadish, S. Pearton), Elsevier Science Ltd, Oxford, **2006**, pp. 1–20.

[49] J. Hüpkes, J. Müller, B. Rech, Texture Etched ZnO:Al for Silicon Thin Film Solar Cells, (Eds.: K. Ellmer, A. Klein, B. Rech), Berlin, Heidelberg, **2008**.

[50] R. Aboorvakani, S. J. K. Vethanathan, K. U. Madhu, *Journal of Alloys and Compounds* **2020**, *834*, 155078.

[51] I. Hamberg, C. G. Granqvist, K. .-. Berggren, B. E. Sernelius, L. Engström, *Phys. Rev. B* **1984**, *30*, 3240–3249.

[52] T. Nagata in *Single Crystals of Electronic Materials*, (Ed.: R. Fornari), Woodhead Publishing Series in Electronic and Optical Materials, Woodhead Publishing, **2019**, pp. 523–546.

[53] M. Thirumoorthi, J. T. J. Prakash, *Journal of Asian Ceramic Societies* **2016**, *4*, 124–132.

[54] M. F. Al-Kuhaili, *Journal of Materials Science: Materials in Electronics* **2020**, *31*, 2729–2740.

[55] Y.-S. Kim, Y.-C. Park, S. Ansari, B.-S. Lee, H.-S. Shin, *Thin Solid Films* **2003**, *426*, 124–131.

[56] K. Zhang, F. Zhu, C. Huan, A. Wee, *Thin Solid Films* **2000**, *376*, 255–263.

[57] T. Ayalew, PhD thesis, Technische Universität Wien, **2004**.

[58] T. Chen, Y. Huang, H. Wang, D. Yang, A. Dasgupta, R. Carius, F. Finger, *Thin Solid Films* **2009**, *517*, Proceedings of the Fifth International Conference on Hot-Wire CVD (Cat-CVD) Process, 3513–3515.

[59] J. M. Zuo, J. C. Spence, *Advanced Transmission Electron Microscopy: Imaging and Diffraction in Nanoscience*, Springer, New York, NY, **2017**.

[60] R. F. Egerton, *Reports on Progress in Physics* **2009**, *72*, 016502.

[61] D. B. Williams, C. B. Carter, *Transmission Electron Microscopy: A Textbook for Materials Science*, 2nd ed., In four volumes, not available separately, Springer, New York, NY, **2009**, pp. LXII + 775.

[62] T. F. Kelly, D. J. Larson, *Annual Review of Materials Research* **2012**, *42*, 1–31.

[63] A. Benninghoven, F. G. Rudenauer, H. W. Werner, *Secondary ion mass spectrometry: basic concepts, instrumental aspects, applications and trends*, John Wiley and Sons,New York, NY, **1987**.

[64] B. Fultz, J. Howe, *Transmission Electron Microscopy and Diffractometry of Materials*, 4th ed., Springer, Berlin, Heidelberg, **2013**.

[65] L. Gu, N. Wang, X. Tang, H. G. Changela, *Scanning* **2020**, *2020*, 8406917.

[66] P. A. Midgley, R. E. Dunin-Borkowski, *Nature Materials* **2009**, *8*, 271–280.

[67] J. Mayer, L. A. Giannuzzi, T. Kamino, J. Michael, *MRS Bulletin* **2007**, *32*, 400–407.

[68] N. Tanaka in *Electron Nano-Imaging: Basics of Imaging and Diffraction for TEM and STEM*, Springer Japan, Tokyo, **2017**, pp. 17–28.

[69] J. Thomas, T. Gemming, *Analytical transmission electron microscopy: an introduction for operators*, Springer Science & Business, **2014**.

[70] R. F. Egerton in *Physical Principles of Electron Microscopy: An Introduction to TEM, SEM, and AEM*, Springer International Publishing, Cham, **2016**, pp. 1–26.

[71] H. H. Radamson, A. Hallén, I. Sychugov, A. Azarov, *Analytical Methods and Instruments for Micro- and Nanomaterials*, 1st ed., Springer, Cham, **2023**, pp. XVI + 282.

[72] L. de Broglie, J. Trillat, *Comptes Rendus Hebdomadaires Des Seances De L Academie Des Sciences* **1925**, *180*, 1485–1487.

[73] K. Thompson-Russell, J. Edington, Practical Electron Microscopy in Materials Science, Monograph Five-Electron Microscope Specimen Preparation, **1975**.

[74] M. De Graef, *Introduction to Conventional Transmission Electron Microscopy*, Cambridge University Press, **2003**.

[75] H. Rose, *Ultramicroscopy* **1994**, *56*, 11–25.

[76] R. Erni, M. D. Rossell, C. Kisielowski, U. Dahmen, *Phys. Rev. Lett.* **2009**, *102*, 096101.

[77] O. Scherzer, *Zeitschrift fur Physik* **1936**, *101*, 593–603.

[78] O. Scherzer, *Journal of Applied Physics* **1949**, *20*, 20–29.

[79] M. Haider, H. Rose, S. Uhlemann, E. Schwan, B. Kabius, K. Urban, *Ultramicroscopy* **1998**, *75*, 53–60.

[80] H. Hely, *Optik* **1982**, *60*, 353–370.

[81] D. F. Hardy, PhD thesis, University of Cambridge, Cambridge, UK, **1967**.

[82] H. Koops, G. Kuck, O. Scherzer, *Optik* **1977**, *48*, 225–236.

[83] M. Matijevic, S. Lengweiler, D. Preikszas, H. Müller, R. R. Schröder, G. Benner in EMC 2008 14th European Microscopy Congress 1–5 September 2008, Aachen, Germany, (Eds.: M. Luysberg, K. Tillmann, T. Weirich), Springer Berlin Heidelberg, Berlin, Heidelberg, **2008**, pp. 83–84.

[84] L. Reimer, H. Kohl, *Transmission Electron Microscopy*, Springer New York, NY, **2008**.

[85] D. B. Williams, C. B. Carter, *Transmission electron microscopy: a textbook for materials science*, *Vol. 28*, Elsevier Science, **1997**, pp. 75–75.

[86] *Scanning Transmission Electron Microscopy: Imaging and Analysis*, 1st ed., (Eds.: S. J. Pennycook, P. D. Nellist), Springer, New York, NY, **2011**.

[87] H. Vahidi, K. Syed, H. Guo, X. Wang, J. L. Wardini, J. Martinez, W. J. Bowman, *Crystals* **2021**, *11*, DOI 10.3390/cryst11080878.

[88] K. Kimoto in *Compendium of Surface and Interface Analysis*, (Ed.: T. S. S. S. of Japan), Springer, Singapore, **2018**, pp. 767–773.

[89] C. Ophus, S. E. Zeltmann, A. Bruefach, A. Rakowski, B. H. Savitzky, A. M. Minor, M. C. Scott, *Microscopy and Microanalysis* **2022**, *28*, 390–403.

[90] S. I. Wright, M. M. Nowell, D. P. Field, *Microscopy and Microanalysis* **2011**, *17*, 316–329.

[91] D. VILADOT, M. VÉRON, M. GEMMI, F. PEIRÓ, J. PORTILLO, S. ESTRADÉ, J. MENDOZA, N. LLORCA-ISERN, S. NICOLOPOULOS, *Journal of Microscopy* **2013**, *252*, 23–34.

[92] P. W. Trimby, *Ultramicroscopy* **2012**, *120*, 16–24.

[93] C. Ophus, *Microscopy and Microanalysis* **2019**, *25*, 563–582.

[94] J. Donohue, S. E. Zeltmann, K. C. Bustillo, B. Savitzky, M. A. Jones, G. F. Meyers, C. Ophus, A. M. Minor, *iScience* **2022**, *25*, 103882.

[95] D. Van Der Wal, *Microscopy Today* **2023**, *31*, 15–17.

[96] A. D. Darbal, M. Gemmi, J. Portillo, E. Rauch, S. Nicolopoulos, *Microscopy Today* **2012**, *20*, 38–42.

[97] O. Krivanek, N. Dellby, J. Hachtel, J.-C. Idrobo, M. Hotz, B. Plotkin-Swing, N. Bacon, A. Bleloch, G. Corbin, M. Hoffman, C. Meyer, T. Lovejoy, *Ultramicroscopy* **2019**, *203*, 75th Birthday of Christian Colliex, 85th Birthday of Archie Howie, and 75th Birthday of Hannes Lichte / PICO 2019 - Fifth Conference on Frontiers of Aberration Corrected Electron Microscopy, 60–67.

[98] Y. J. Kim, L. D. Palmer, W. Lee, N. J. Heller, S. K. Cushing, *The Journal of Chemical Physics* **2023**, *159*, 050901.

[99] R. Singh in *Transmission Electron Microscopy Sample Preparation: From Specimen to Micrograph*, Springer Nature Switzerland, Cham, **2024**, pp. 43–59.

[100] J. Ayache, L. Beaunier, J. Boumendil, G. Ehret, D. Laub, *Sample Preparation Handbook for Transmission Electron Microscopy*, Springer New York, NY, **2010**.

[101] L. Giannuzzi, F. Stevie, *Micron* **1999**, *30*, 197–204.

[102] L. Jian, T. Malis, S. Dionne, *Materials Characterization* **2006**, *57*.

[103] M. Schaffer, B. Schaffer, Q. Ramasse, *Ultramicroscopy* **2012**, *114*, 62–71.

[104] E. Montoya, S. Bals, M. D. Rossell, D. Schryvers, G. V. Tendeloo, *Microscopy Research and Technique* **2007**, *70*, Research Support, Non-U.S. Gov't, 1060–1071.

[105] T. C. Isabell, P. E. Fischione, C. O'Keefe, M. U. Guruz, V. P. Dravid, *Microscopy and Microanalysis* **2002**, *5*, 126–135.

[106] I. M. Watt in *The Principles and Practice of Electron Microscopy*, Cambridge University Press, **1997**, pp. i–iv.

[107] D.-S. Ko, Y. M. Park, S.-D. Kim, Y.-W. Kim, *Ultramicroscopy* **2007**, *107*, 368–373.

[108] D. V. S. Rao, K. Muraleedharan, C. Humphreys, *Microscopy: Science Technology Applications and Education* **2010**.

[109] D. Cooper, R. Truche, J.-L. Rouviere, *Ultramicroscopy* **2008**, *108*, 488–493.

[110] Y. Liao, *An Online Book* **2006**, *3*, 1412.

[111] F. Ji, Y. Yao, T. Xin, J. Seidel, *Nanomanufacturing and Metrology* **2022**, *5*, 67–79.

[112] S. RUBANOV, P. R. MUNROE, *Journal of Microscopy* **2004**, *214*, 213–221.

[113] D. Drobne, M. Milani, V. Lešer, F. Tatti, *Microscopy Research and Technique* **2007**, *70*, 895–903.

[114] J. Wang, F. Zhong, H. Liu, L. Zhao, W. Wang, X. Xu, Y. Zhang, H. Yan, *Solar Energy* **2021**, *221*, 114–119.

[115] H. Sharma, S. Bhattacharya, S. Alam, S. Manna, A. Pandey, S. P. Singh, V. K. Komarala, *Applied Physics A* **2025**, *131*, 458.

[116] *Introduction to Focused Ion Beams, Instrumentation, Theory, Techniques and Practice*, 1st ed., (Eds.: L. A. Giannuzzi, F. A. Stevie), Springer, New York, NY, **2005**, pp. XVII, 357.

[117] K. Larsen, The effects of Ga FIB milling on analysis, Accessed: 2025-09-24, **2021**.

[118] M. Corazza, S. B. Simonsen, H. Gnaegi, K. T. Thydén, F. C. Krebs, S. A. Gevorgyan, *Applied Surface Science* **2016**, *389*, 462–468.

[119] S. Alkhereibi, M. A. Yaqin, A. Eberst, B. Xu, J. Jo, H. Alsamamra, A. Lambertz, U. Rau, K. Ding, J. Mayer, *Thin Solid Films* **2025**, *825*, 140744.

[120] H. Sai, T. Matsui, *Solar RRL* **2023**, *7*, 2300290.

[121] W. Huang, J. Shi, Y. Liu, F. Meng, Z. Liu, *Journal of Alloys and Compounds* **2020**, *843*, 155151.

[122] Z. Yao, W. Duan, P. Steuter, J. Hüpkes, A. Lambertz, K. Bittkau, M. Pomaska, D. Qiu, K. Qiu, Z. Wu, H. Shen, U. Rau, K. Ding, *Solar RRL* **2021**, *5*, 2000501.

[123] H. Li, S. Yin, G. Dong, G. Cui, C. Lei, Y. Li, X. Xu, L. Feng, J. Zhang, C. Yu, *Solar Energy* **2020**, *196*, 125–131.

[124] E. Kobayashi, Y. Watabe, T. Yamamoto, Y. Yamada, *Solar Energy Materials and Solar Cells* **2016**, *149*, 75–80.

[125] O. Madani Ghahfarokhi, K. Chakanga, S. Geissendoerfer, O. Sergeev, K. von Maydell, C. Agert, *Progress in Photovoltaics: Research and Applications* **2015**, *23*, 1340–1352.

[126] G. Dong, J. Li, Y. Zhao, X. Ran, C.-W. Peng, D. He, C. Jin, Q. Wang, H. Jiang, Y. Zhang, X. Cao, C. Yu, *Progress in Photovoltaics: Research and Applications* **2023**, *31*, 931–938.

[127] Q. Tang, W. Duan, A. Lambertz, K. Bittkau, M. A. Yaqin, Y. Zhao, K. Zhang, Q. Yang, D. Qiu, F. Gunkel, M. Weber, U. Rau, K. Ding, *Solar Energy Materials and Solar Cells* **2023**, *251*, 112120.

[128] C. Agashe, O. Kluth, J. Hüpkes, U. Zastrow, B. Rech, M. Wuttig, *Journal of Applied Physics* **2004**, *95*, 1911–1917.

[129] H. Scherg-Kurmes, S. Seeger, S. Körner, B. Rech, R. Schlatmann, B. Szyszka, *Thin Solid Films* **2016**, *599*, 78–83.

[130] A. Valla, P. Carroy, F. Ozanne, D. Muñoz, *Solar Energy Materials and Solar Cells* **2016**, *157*, 874–880.

[131] K. Ellmer, R. Mientus, *Thin Solid Films* **2008**, *516*, 5th International Symposium on Transparent Oxide Thin Films for Electronics and Optics, 5829–5835.

[132] P. Šotová, P. Novák, T. Kozák, *AIP Conference Proceedings* **2021**, *2411*, 030007.

[133] Z. Zhang, Y. Tang, J. Chen, J. Chen, *Physica B: Condensed Matter* **2016**, *495*, 76–81.

[134] A. Cruz, F. Ruske, A. Eljarrat, P. P. Michalowski, A. B. Morales-Vilches, S. Neubert, E.-C. Wang, C. T. Koch, B. Szyszka, R. Schlatmann, B. Stannowski, *IEEE Journal of Photovoltaics* **2020**, *10*, 703–709.

[135] N. P. Patel, K. V. Chauhan, *Materials Today: Proceedings* **2022**, *62*, International Conference on Materials, Processing & Characterization (13th ICMPC), 3386–3396.

[136] G. Kiriakidis, M. Suchea, S. Christoulakis, P. Horvath, T. Kitsopoulos, J. Stoemenos, *Thin Solid Films* **2007**, *515*, First International Symposium on Transparent Conducting Oxides, 8577–8581.

[137] B. Mendis, K. Durose, *Ultramicroscopy* **2012**, *119*, Special Issue: Gertrude F. Rempfer 100th Birthday Memorial, 82–96.

[138] D. Abou-Ras, M. Nichterwitz, M. J. Romero, S. S. Schmidt in *Advanced Characterization Techniques for Thin Film Solar Cells*, John Wiley & Sons, Ltd, **2016**, Chapter 14, pp. 371–420.

[139] K. Durose, S. E. Asher, W. Jaegermann, D. Levi, B. E. McCandless, W. Metzger, H. Moutinho, P. Paulson, C. L. Perkins, J. R. Sites, G. Teeter, M. Terheggen, *Progress in Photovoltaics: Research and Applications* **2004**, *12*, 177–217.

[140] K. Wang, P. Jiao, Y. Cheng, H. Xu, G. Zhu, Y. Zhao, K. Jiang, X. Zhang, Y. Su, *Optical Materials* **2022**, *134*, 113040.

[141] H. Park, S. Qamar Hussain, S. Velumani, A. H. Tuan Le, S. Ahn, S. Kim, J. Yi, *Materials Science in Semiconductor Processing* **2015**, *37*, Advances in functional semiconducting materials (Int. Mat. Res. Cong. - 2014), 29–36.

[142] P. Misra, V. Ganeshan, N. Agrawal, *Journal of Alloys and Compounds* **2017**, *725*, 60–68.

[143] D. Qiu, W. Duan, A. Lambertz, A. Eberst, K. Bittkau, U. Rau, K. Ding, *Solar RRL* **2022**, *6*, 2200651.

[144] H. Li, W. Duan, A. Lambertz, J. Hüpkes, K. Ding, U. Rau, O. Astakhov, *IEEE Journal of Photovoltaics* **2019**, *9*, 1485–1491.

[145] K. C. Park, D. Y. Ma, K. H. Kim, *Thin Solid Films* **1997**, *305*, 201–209.

[146] A. B. Morales Vilches, A. Cruz, S. Pingel, S. Neubert, L. Mazzarella, D. Meza, L. Korte, R. Schlatmann, B. Stannowski, *IEEE Journal of Photovoltaics* **2019**, *9*, 34–39.

[147] D. Meza, A. Cruz, A. B. Morales-Vilches, L. Korte, B. Stannowski, *Applied Sciences* **2019**, *9*, DOI 10.3390/app9050862.

[148] L.-L. Senaud, G. Christmann, A. Descoeudres, J. Geissbühler, L. Barraud, N. Badel, C. Allebé, S. Nicolay, M. Despeisse, B. Paviet-Salomon, C. Ballif, *IEEE Journal of Photovoltaics* **2019**, *9*, 1217–1224.

[149] Z. Wu, W. Duan, A. Lambertz, D. Qiu, M. Pomaska, Z. Yao, U. Rau, L. Zhang, Z. Liu, K. Ding, *Applied Surface Science* **2021**, *542*, 148749.

[150] D. A. Muller, *Nature Materials* **2009**, *8*, 270.

[151] F. G. R. Sagalowicz Laurent, *Journal of Materials Research* **1999**, *14*, DOI `https://doi.org/10.1557/JMR.1999.0252`.

[152] J. Lee, D. Lee, D. Lim, K. Yang, *Thin Solid Films* **2007**, *515*, Proceedings of Sympodium O on Thin Film Chalcogenide Photovoltaic Materials, EMRS 2006 Conference, 6094–6098.

[153] K. Omri, I. Najeh, S. Mnefgui, N. Alonizan, S. Gouadria, *Materials Science and Engineering: B* **2023**, *297*, 116738.

[154] A. Eberst, B. Xu, K. Bittkau, W. Duan, A. Lambertz, A. Meise, M. Heggen, R. E. Dunin-Borkowski, U. Rau, K. Ding, *Advanced Physics Research* **2024**, *3*, 2400036.

[155] S. D. Wolf, A. Descoeudres, Z. C. Holman, C. Ballif, *Green* **2012**, *2*, 7–24.

[156] T. G. Allen, J. Bullock, X. Yang, A. Javey, S. D. Wolf, *Nature Energy* **2019**, *4*, 914–928.

[157] V. Linss, M. Bivour, H. Iwata, K. Ortner, *AIP Conference Proceedings* **2019**, *2147*, 040009.

[158] M. H. .-. P. .-. S. E. Inc., *Semicore Equipment Inc.* **2016**.

[159] A. Diggs, Z. Zhao, R. V. Meidanshahi, D. Unruh, S. Manzoor, M. Bertoni, S. M. Goodnick, G. T. Zimányi, *Communications Materials* **2023**, *4*, 24.

[160] C. Gatzen, I. Smokovych, M. Scheffler, M. Krüger, *Advanced Engineering Materials* **2021**, *23*, 2001016.

[161] A. Illiberi, P. Kudlacek, A. H. M. Smets, M. Creatore, M. C. M. van de Sanden, *Applied Physics Letters* **2011**, *98*, 242115.

[162] S. De Wolf, B. Demaurex, A. Descoeudres, C. Ballif, *Phys. Rev. B* **2011**, *83*, 233301.

[163] V. Kanneboina, *Microelectronic Engineering* **2022**, *265*, 111884.

[164] H. Fujiwara, M. Kondo, *Applied Physics Letters* **2007**, *90*, 013503.

[165] B. Shin, T. Lee, J. Prakash Kar, M. Lee, K. Park, K. Ahn, K. Yeom, J. Cho, J. Myoung, *Materials Science in Semiconductor Processing* **2011**, *14*, Funding Information: This research was supported by the Converging Research Center Program through the Ministry of Education, Science and Technology (Grant no. 2010K001082)., 23–27.

[166] R. Cebulla, R. Wendt, K. Ellmer, *Journal of Applied Physics* **1998**, *83*, 1087–1095.

[167] M. Huang, Z. Hameiri, A. G. Aberle, T. Mueller, *Vacuum* **2015**, *119*, 68–76.

[168] A. Machín, F. Márquez, *Materials* **2024**, *17*, DOI 10.3390/ma17051165.

[169] J. Melskens, B. {van de Loo}, B. Macco, L. Black, S. Smit, W. Kessels, *IEEE Journal of Photovoltaics* **2018**, *8*, 373–388.

[170] M. Köhler, A. Zamchiy, M. Pomaska, A. Lambertz, F. Lentz, W. Duan, V. Smirnov, F. Finger, U. Rau, K. Ding in 2018 IEEE 7th World Conference on Photovoltaic Energy Conversion (WCPEC) (A Joint Conference of 45th IEEE PVSC, 28th PVSEC & 34th EU PVSEC), **2018**, pp. 3468–3472.

[171] A. Heidt, T. Chen, R. Carius, F. Finger, U. Rau, J. Mayer, M. Luysberg, *Journal of Physics: Conference Series* **2011**, *326*, 012019.

[172] S. Klein, R. Carius, F. Finger, L. Houben, *Thin Solid Films* **2006**, *501*, Proceedings of the Third International Conference on Hot-Wire CVD (Cat-CVD) Process, 169–172.

[173] A. Eberst, A. Lambertz, W. Duan, V. Smirnov, U. Rau, K. Ding, *Solar RRL* **2023**, *7*, 2300013.

[174] H. Zhang, L. Zhang, W. Liu, Y. Zhou, S. Lan, K. Jiang, J. Du, A. Han, H. Zhao, H. Zhang, J. Shi, F. Meng, Z. Liu, *Applied Physics Letters* **2023**, *122*, 182101.

[175] A. Sinha, J. Qian, S. L. Moffitt, K. Hurst, K. Terwilliger, D. C. Miller, L. T. Schelhas, P. Hacke, *Progress in Photovoltaics: Research and Applications* **2023**, *31*, 36–51.

[176] H. Ye, S. Huang, C. Qian, Z. Sun, Y. Chen, X. Song, Y. Zhang, N. Wang, Y. Hu, Y. Yang, L. Li, Z. Ma, T. Chen, W. Liu, J. Yu, *Solar RRL* **2023**, *7*, 2300334.

[177] B. Xu, K. Bittkau, A. Eberst, K. Zhang, Y. Liu, J. Yang, W. Duan, M. A. Yaqin, V. Smirnov, C. Zhou, W. Wang, X. Xu, A. Lambertz, U. Rau, K. Ding, *Advanced Energy and Sustainability Research* **2025**, *6*, 2400227.

[178] S. W. Glunz, F. Feldmann, *Solar Energy Materials and Solar Cells* **2018**, *185*, 260–269.

[179] L. Yang, Z. Hu, Q. He, Z. Liu, Y. Zeng, L. Yang, X. Yu, D. Yang, *Solar Energy Materials and Solar Cells* **2024**, *275*, 113022.

[180] F. T. Thome, P. Meßmer, S. Mack, E. Schnabel, F. Schindler, W. Kwapil, M. C. Schubert, *Solar RRL* **2024**, *8*, 2400628.

Band / Volume 730
Land-Atmosphere Coupling in a Changing Climate: Understanding Variability, Extremes, and Human Influence through Regional Climate Modeling
Y. Zhang (2026), 135 pp
ISBN: 978-3-95806-980-0 (Print)
ISBN: 978-3-95806-981-7 (E-Book)

Band / Volume 731
Abbildung gekoppelter Infrastrukturen in Energiesystemmodellen
P. Freitag (2026), XIX, 322 pp
ISBN: 978-3-95806-984-8 (Print)
ISBN: 978-3-95806-985-5 (E-Book)

Band / Volume 732
Cost-reduced and Sustainable Interconnects and their Coatings for Solid Oxide Cells
M. Hilger (2026), viii, 185 pp
ISBN: 978-3-95806-988-6 (Print)
ISBN: 978-3-95806-989-3 (E-Book)

Band / Volume 733
Liquid-Phase Synthesis of Silicon and Silicon Carbide Thin-Films via Atmospheric Pressure Chemical Vapor Deposition
B. Fischer (2026), xxii, 211, A15 pp
ISBN: 978-3-95806-990-9 (Print)
ISBN: 978-3-95806-991-6 (E-Book)

Band / Volume 734
Modellgestützte Transformationspfade des deutschen Energiesystems
R. Maier (2026), xxvii, 331 pp
ISBN 978-3-95806-994-7 (Print)
ISBN 978-3-95806-995-4 (E-Book)

Band / Volume 735
Dynamical drivers of deep and shallow branches in the stratospheric circulation and transport
R.- A. Baikhadzhaev (2026), 120 pp
ISBN 978-3-95806-996-1 (Print)
ISBN 978-3-95806-997-8 (E-Book)

Band / Volume 736
Silicon heterojunction solar cells on thin wafers – prospects in different utilization scenarios
U. K. Chime (2026), 151 pp
ISBN 978-3-95806-998-5 (Print)
ISBN 978-3-95806-999-2 (E-Book)

Band / Volume 737
Advancing the understanding of actual evapotranspiration and critical soil moisture thresholds using lysimeter networks
X. Lu (2026), XXX, 159 pp
ISBN 978-3-69367-000-2 (Print)
ISBN 978-3-69367-001-9 (E-Book)

Band / Volume 738
Einfluss des automatisierten Fahrens auf die technoökonomische Performance von Verkehrssystemen
E. Jungblut (2026), VIII, 304 pp
ISBN 978-3-69367-006-4 (Print)
ISBN 978-3-69367-007-1 (E-Book)

Band / Volume 739
Photon-assisted Degradation and Recovery of Transparent Passivating Contact Silicon Solar Cells
B. Xu (2026), xii, 189 pp
ISBN 978-3-69367-008-8 (Print)
ISBN 978-3-69367-009-5 (E-Book)

Band / Volume 740
Effects of Microplastics on Carbon and Nitrogen Turnover Processes in the Rhizosphere of Crops
K. J. Neubert (2026), xxii, 193 pp
ISBN 978-3-69367-010-1 (Print)
ISBN 978-3-69367-011-8 (E-Book)

Band / Volume 741
Comprehensive Understanding and Optimization of the Tape Casting Process for the Fabrication of LLZO-Based Solid-State Battery Components
K. N. El K. Touidjine (2026), XV, 170 pp
ISBN 978-3-69367-016-3 (Print)
ISBN 978-3-69367-017-0 (E-Book)

Band / Volume 742
Microstructure and Functionality of Heterojunction contacts on crystalline Silicon solar cells
S. Alkhereibi (2026); 170 pp
ISBN 978-3-69367-018-7 (Print)
ISBN 978-3-69367-019-4 (E-Book)

Weitere ***Schriften des Verlags im Forschungszentrum Jülich*** unter
http://wwwzb1.fz-juelich.de/verlagextern1/index.asp

Energie & Umwelt / Energy & Environment
Band / Volume 742
ISBN 978-3-69367-019-4

Mitglied der Helmholtz-Gemeinschaft

JÜLICH
Forschungszentrum